

Thesis Proposal

CONTINUAL LEARNING ENABLED AGENTIC ADDITIVE MANUFACTURING PROCESS OPTIMIZATION

by

Peter Myung-Won Pak

Department of Mechanical Engineering
College of Engineering
Carnegie Mellon University
Pittsburgh, Pennsylvania, USA

February 2026

Submitted in partial fulfillment of the requirements
for the degree of Doctor of Philosophy
in Mechanical Engineering

Thesis Proposal Committee: Dr. Amir Barati Farimani, Thesis Supervisor
Dr. Anthony Rollett
Dr. Jon Malen
Dr. Sneha Prabha Narra

Copyright © 2026
Peter Myung-Won Pak
All Rights Reserved

ABSTRACT

The additive manufacturing process is a complex and multi-faceted fabrication challenge which expands in complexity at higher levels of precision. Specifically, powder based processes such as Laser Powder Bed Fusion and Selective Laser Sintering present challenges from overall build feasibility to defect mitigation within the final part. Approaches to combat potential issues have explored feedforward and feedback control of the build process utilizing *in-situ* process monitoring data, multi-physics simulation, and machine learning models to detect and address potential defects before they arise in the build. These approaches have shown success in limited and controlled experimental trials and exploration of implementing these systems in a dynamic environment is yet to be done. In this work an agentic system will be developed for the optimization of the selective laser sintering process and integrated into a continual learning environment to further account for changing environmental variables.

This proposal will first explore the works achieved to develop the individual components of this system starting from the process monitoring with *in-situ* two-color pyrometry data, to fine-tuning large language models for domain knowledge integration, and agentic system implementation of the intelligent automation of research tasks. These works set the foundation for the proposed work for an agentic process optimization system within selective laser sintering where through experimental trials and prints, the capabilities

of the system will be evaluated. The results obtained from these experiments will further expand the dataset used to fine-tune this system into a continual learning environment where system will better understand the dynamics of its environment.

CONTENTS

List of Figures	viii
List of Tables	xiv
1 Overview	1
1.1 Introduction	1
1.1.1 Foundation of Powder Bed Additive Manufacturing	1
1.1.2 Tokenization in Large Language Models	3
Subword Neural Machine Translation	3
Byte Pair Encoding	4
1.1.3 Reasoning and Prompting	4
Chain-of-Thought	4
Zero-Shot Chain of Thought	6
ReAct	6
1.1.4 Agentic Tool Calling	7
WebGPT	7
ReAct	7
1.2 Structure of the Thesis Proposal	8
2 ThermoPore: Predicting Part Porosity Based on Thermal Images Using Deep Learning	10
2.1 Introduction	10
2.2 Methodology	14
2.2.1 <i>Spacing and Velocity Samples</i>	14
Sample Fabrication and Data Acquisition	14
In-situ Pyrometry	15
Ex-situ Micro-computed Tomography (CT)	16
2.2.2 Pyrometry and Micro-computed Tomography Datasets	17
Pyrometry and Micro-computed Tomography Alignment	17
Data Alignment	17
Pore Thresholding	18
2.3 Porosity Reconstruction	20
2.3.1 Porosity Count	21

2.3.2	Porosity Localization	23
2.4	Results and Discussion	25
2.4.1	Porosity Count	25
2.4.2	Porosity Localization	28
2.4.3	Model Limitations	30
2.5	Conclusion and Future Work	31
2.6	Appendix	32
2.6.1	Input Cropping and Label Downsampling	32
2.6.2	Calculating absolute temperature estimations with data obtained through Stratonics pyrometer	33
2.6.3	Sample alignment of thermal images to CT data along the X and Y axes	34
2.6.3	Trends of IoU scores of ViViT Dense models trained varying pore datasets	34
3	AdditiveLLM: Large Language Models Predict Defects in Metals Additive Manufacturing	37
3.1	Methodology	40
3.1.1	Task	40
3.1.2	Dataset	41
Data Generation and Split	43	
<i>Baseline</i> Dataset	44	
<i>Prompt</i> Dataset	44	
3.1.3	Large Language Models	45
DistilBERT	45	
SciBERT	45	
Llama 3	46	
T5	46	
3.1.4	Fine-Tuning	47
3.2	Results and Discussion	47
3.2.1	Model Results	47
<i>Baseline</i> Fine-Tuned LLMs	48	
<i>Prompt</i> Fine-Tuned LLMs	50	
Impact of Dataset Composition	50	
3.2.2	<i>Baseline</i> vs. <i>Prompt</i> Fine-Tuned LLMs	51
3.2.3	Principle Component Analysis	53
3.3	Conclusion and Future Work	53
3.3.1	Conclusion	53
3.3.2	Future Work	55
3.3.3	Data Availability	56

3.4 Appendix	57
3.4.1 Model Training Resources and Runtimes	57
3.4.2 Model Evaluation Runtimes	58
3.4.3 Prediction Distribution of LLM fine-tuned on <i>Baseline</i> Dataset	59
3.4.4 Prediction Distribution of LLM fine-tuned on <i>Prompt</i> Dataset	60
4 Agentic Additive Manufacturing Alloy Evaluation	61
4.1 Introduction	61
4.2 Methodology	63
4.2.1 Calculation of Thermophysical Properties	63
Absorptivity Calculation and Limitation	66
4.2.2 Lack of Fusion Defect Prediction	67
Dimensional Approximation of the Melt Pool	67
Model Assumptions and Limitations	68
Defect Domain Scope and Applicability	69
4.2.3 Model Context Protocol	70
Tools	70
Resources	71
4.2.4 Agentic Tools	72
Workspace	72
Thermo-Calc	73
Additive Manufacturing	76
4.2.5 Experiments	78
Known Alloy Compositions	78
Material Property Search	79
Novel Alloy Compositions	79
4.3 Results	79
4.3.1 Lack of Fusion Validation of Known Alloy Compositions	82
Inconel 718	83
Stainless Steel 316L	83
4.4 Discussion	84
4.4.1 Comparison to Existing Tool Integration Frameworks	86
4.5 Conclusion	86
4.6 Future Work	87
4.6.1 Technical Roadmap	87
Objective	87
Methodology	87
Evaluation Metrics	88

Timeline	88
4.7 Data Availability	88
4.8 Appendix	90
4.8.1 Model Context Protocol Example Tool	90
4.8.2 Melt Pool Length	90
4.8.3 Database Selection	92
4.8.4 Validation of Predicted Absorptivity	93
4.8.5 Lack of Fusion and Keyhole Boundaries of Known Alloys	93
4.8.6 LLM Prompt and Response for Corrosion Resistant Material Property Search	93
5 Proposed Work and Timeline	96
5.1 Proposed Work: Agentic Process Optimization for Selective Laser Sintering	96
5.1.1 Experimental Platform	96
SLS4All Inova Mk1	96
Platform Limitations	99
5.1.2 Agentic System	99
Material Selection Tool	99
Simulation Tool	100
Parameter Testing Tool	100
Print Profile Tool	100
Build Monitoring Tool	101
5.1.3 Evaluation	101
5.2 Proposed Work: Continual Learning enabled Additive Manufacturing Large Language Model	102
5.3 Timeline	102
Bibliography	104

LIST OF FIGURES

1.1	Hypothetical comparison of outputs between standard prompting process to that of the chain-of-thought reasoning process.	5
2.1	A sequence of 200 thermal pyrometry images (4.1c) providing absolute temperature values of the build plate taken <i>in-situ</i> (4.1a) are provided as input data for models for pore quantification (4.1d) and pore localization (4.1e). These two separate models utilize a CNN and ViViT with dense output heads to produce a scalar number of pores and 2D mapping of expected porosity regions respectively. Metrics derived from <i>ex-situ</i> CT data for the corresponding build layer are used as ground truth values for each model (4.1b).	14
2.2	Each sample (2.2a) contains 10 different process parameter combinations with the <i>Spacing</i> sample (2.2b) exhibiting varying hatch spacing and the <i>Velocity</i> sample (2.2c) exhibiting varying scan velocity.	15
2.3	Visualization of segmented CT porosity within overall sample for <i>Spacing</i> and <i>Velocity</i> samples (2.3a). Figure 2.3b superimposes the pyrometry image directly over the corresponding CT data with alignment offsets applied along the X and Y axes, using the top left corner of both as the origin. Alignment for a build layer is visually validated (2.3c) as only a subset of the built sample is visible through the lens of the pyrometer (2.3d).	18
2.4	The <i>Spacing</i> sample on average consist of larger pores with a standard deviation of 20.5 μm compared to the <i>Velocity</i> sample's standard deviation of 16.0 μm (2.4a). The tighter distribution of <i>Velocity</i> pores are visible in the thresholded distribution of equivalent pore sizes (2.4b) within the slices of the CT data. The segmentation of pores within the sample (2.4c) relied on a minimum of 100 voxels (11.4 μm equivalent spherical diameter)[153] in order to register the contiguous cluster of voids as porosity (2.4d) and an increase in the minimum size further removed smaller pores (2.4e).	19

2.5	A standard convolutional neural network with a kernel size of 3 pixels and a stride of 2 filters the features within an image down over 4 layers to a singular scalar value indicating the expected number of pores from the sequence of thermal images.	22
2.6	The input sequence of thermal images are sliced into a set of patches (2.6a) where 4 and 5 sublayers of the respective spatial and temporal self attention are applied (2.6b). Each self attention block consisted of 8 attention heads (2.6c) of a dimension of 256. A feature fusion block (2.6d) applies residual convolution and a dense prediction head produces a 2 dimensional output indicating regions of expected porosity.	24
2.7	CNN pore count predictions plotted alongside target pore values for <i>Spacing</i> , <i>Velocity</i> , and <i>All</i> (combination of both datasets) for a depth of 1 build layer. In all plots the pore counts for build layers 100 - 160 are clustered near the origin as the upper half of the sample is composed of nominal process conditions. Of all the various implementations, the CNN model trained on the <i>Spacing</i> (Top Left) dataset without transforms shows the greatest level of alignment between the prediction and ground truth.	27
2.8	Comparison of prediction and label values for the model trained on the <i>All</i> samples dataset alongside the application of a minimum ESD pore threshold (Fig. 2.8b). The examples correspond to build layer number 16 of the <i>Velocity</i> sample and the areas colored in yellow represent the intersection that is considered for IoU calculations (ignoring the background). The ViViT model trained on pores without thresholding (Fig. 2.8a) achieved an IoU score of 0.672 whereas the model trained with $\mu + \sigma$ thresholded pores (Fig. 2.8b) produced a lower IoU score of 0.323.	29
2.9	Relative porosity locations are derived from the raw CT data which are cropped to capture a consistent area to match the input thermal data (Fig. 2.9a). The CT data is further downsampled factor of 24 and cropped to provide a 16 x 16 label shape (Fig. 2.9b).	33
2.10	ViViT Dense model IoU trends by build layer for various datasets with and without rotational transforms without the application of a minimum pore threshold.	35
2.11	ViViT Dense model IoU trends by build layer for various datasets with and without rotational transforms with the application of minimum equivalent diameter pore threshold where equivalent sphere diameter of pores are 1 standard deviation above the mean ($\mu + \sigma$ Pores).	36

3.1	A series of LLM models are fine-tuned with a process parameter defect dataset generated from experimental results obtained from literature and simulations performed with FLOW-3D. The corresponding melt pool dimensions are used in the computation of defect criterions used as classifications labels for a specific process parameter combination. A prompt which incorporates the process parameters is provided as input to the model which in turn predicts the potential defect classification.	39
3.2	The highlighted attributes are replaced with the appropriate values and corresponding units, unknown values are replaced with an empty string.	41
3.3	The text of each input label pair is formatted to a set of prompt templates, taking in consideration the multiple ways an input query can be structured.	41
3.4	Melt pool dimensions dependent on the corresponding process parameters are obtained through either experimental cross-sectional measurements or computational fluid dynamic simulations. The obtained depth, length, and width, dimensions, pass through a set of criterions that determine the potential defects that would arise from the combination of process parameters.	42
3.5	Distribution of materials and defect classifications within the dataset comprised of samples from original sources and augmented samples where additional <i>Lack of Fusion</i> classifications were obtained. . . .	43
3.6	Distribution of materials and defect classifications within the train, test, and validation splits are derived from the <i>Augmented Dataset</i>	44
3.7	F1 Scores for each of the defect types with their corresponding total samples below each class label within either <i>Baseline</i> (left) or <i>Prompt</i> (right) dataset fine-tuned models. Within evaluation set the 44.76% are classified as <i>None</i> , 13.84% as <i>Keyhole</i> , 35.48% as <i>Lack of Fusion</i> , and 5.90% as <i>Balling</i> . Notably F1 scores for the highest performing <i>Baseline</i> Llama and <i>Prompt</i> DistilBERT fine-tuned models display relatively consistently values throughout all classifications.	49
3.8	Distribution of F1 scores within each corresponding class for DistilBERT <i>Prompt</i> and Llama <i>Baseline</i> fine-tuned models on SS316L (common) and IN615 (uncommon) samples.	52
3.9	Principle Component Analysis (PCA) of LLMs fine-tuned and evaluated with the <i>Baseline</i> dataset. For all models, the labels of <i>Keyhole</i> and <i>Lack of Fusion</i> share a high degree of overlap to the extent that <i>Lack of Fusion</i> covers much of the <i>Keyhole</i> labels.	54

3.10 Principle Component analysis of LLM models fine-tuned on the <i>Baseline</i> dataset and inference using the <i>Prompt</i> dataset show high degrees of overlap between all labels indicating the models struggle to extract relevant information when formatted in natural language.	55
3.11 LLMs fine-tuned on <i>Baseline</i> dataset have prediction distributions similar to that of the <i>Augmented</i> dataset with the exception on the T5 model.	59
3.12 LLMs fine-tuned on <i>Prompt</i> dataset exhibit a wider range of classification distribution labels with DistilBERT and SciBERT most closely resembling that of the <i>Augmented</i> dataset.	60
4.1 (Top Left) An input query for alloy compositions regarding the printability of an additively manufactured part suitable for its intended use case is provided to Claude Sonnet. This Large Language Model (LLM) calls the tools necessary to generate and analyze each potential alloy compositions, providing a response of candidates ranked by their content of their lack of fusion fusion regimes. (Top Right) Thermo-Calc allows for the retrieval of material properties for an hypothetical alloy composition, for instance thermal conductivity, to be used in down stream lack of fusion calculations. (Bottom Left) Workspaces provide a way for each of the tools to effectively communicate with one another and handles state management and file organization. (Bottom Right) Tools managed by the Additive Manufacturing subagents then utilize the calculated material properties from the Thermo-Calc subagent to generate a lack of fusion process map to send back to the LLM for analysis and final recommendation.	64
4.2 (Left) Claude Code provides an interface for integrating agentic tools with Claude Sonnet LLM, allowing for natural language input to execute tasks and response analysis. (Right) Streamlined summary of tool executions and analysis from the prompt given to Claude Code utilizing subagents for Additive Manufacturing, Thermo-Calc, and Workspace.	71
4.3 A simple tool calling procedure within the Workspace subagent for the task of finding or initializing a workspace. Here an initial tool call is made to list available workspaces and if none are found, a new workspace is created. This newly initialized workspace or the most relevant selected by Claude Sonnet is included in the successful response object.	73

4.4	Flow diagram outlines the expected tool calling procedure for the Thermo-Calc subagent. In this example the material properties for Stainless Steel are extracted from the calculated property diagram of the alloy's elemental composition. Composition is obtained from a look-up table of known alloys or provided directly to the agentic system and parsed into mass fractions using Claude Sonnet. This process generates a schema file with alloy's material properties recorded for downstream use with other tools.	75
4.5	Diagram outlines expected tool calling procedure for additive manufacturing subagent for the task for generating and analyzing a lack of fusion process map. Build and material configurations are required to initialize a process map, the latter of which can be obtained from the Thermo-Calc subagent or manually configured by the additive manufacturing subagent. Initializing the process map provides override ranges for power and velocity build parameters for melt pool depth calculations. The tool generates the process map and a response consisting of power and velocity configurations that potentially exhibit lack of fusion defects. Claude Sonnet analyzes this response and provides suggestion for optimal build parameters.	77
4.6	Lack of fusion process maps for a selection of known alloys with default hatch spacings of 50 μm and various layer heights indicated by their respective colors within the legend.	80
4.7	Comparison of lack of fusion process maps of between Inconel 625 and Stainless Steel 316L for corrosion resistant applications. Between these two candidates, the LLM ultimately recommended the use of Inconel 625 for its smaller lack of fusion regime.	81
4.8	Various lack of fusion process maps for novel alloy compositions. (Top Row) Hypothetical element compositions for proposed Iron and Aluminum based alloys. (Bottom Row) slightly modified known alloy compositions of Inconel and Stainless Steel 316L with the removal of Molybdenum. (Bottom Right) An LLM proposed composition when prompted to suggest an novel alloy.	82
4.9	High hardness alloy candidates with their respective lack of fusion process maps. LLM makes an error by recommending Enhanced Maraging Steel over High Strength Stainless Steel for its smaller lack of fusion region.	85
4.10	Example tool implementation shown via Solver tool defined in additive-manufacturing package.	91
4.11	Database selection decision tree	92

4.12	Literature values for SS316L and IN718 melt pool classifications expected defect regions for each respective alloy. Logistic regression is applied to establish a boundary between the two regions to reference as threshold to the extent in which Rosenthal's equation can be used to predict lack of fusion defects.	94
4.13	Prompt response and reasoning provided by agentic system for evaluating lack of fusion process map for known alloys.	95
5.1	Flow diagram depicts simplified user interaction with agentic system for parameter selection and process monitoring for the Inova Mk1. (1) The user prompt is provided as model input (2) and (4) query for the vector database. Results from the vector database is appended to the model input and provided to a LLM. The LLM executes relevant (3) tool calls via MCP with their results added to the vector database. (4) Generated responses from the LLM are added to the vector database for use with future prompts.	97
5.2	Inova Mk1 (a) assembled from kit prints complex geometries, such as the β_2 protein molecule (b), only capable through the SLS process.	98
5.3	5 x 5 grid of patches (a) printed for testing PA12 GF powder, each with their own parameter configuration (b).	101

LIST OF TABLES

2.1	R ² and RMSE prediction performance metrics of pore counts for the pore quantification task utilizing CNN models trained on various datasets and build layer depths for 500 epochs.	28
2.2	Pore localization prediction performance metrics for ViViT Dense model trained on <i>Spacing</i> , <i>Velocity</i> , and <i>All</i> sample datasets for 1000 epochs on both all segmented pores and pores with equivalent diameters greater than 1 standard deviation above the mean. The adjusted threshold to consider only pores with larger equivalent diameters improved prediction results in build layers with nominal process parameter and low resulting porosity.	31
3.1	Accuracy and F1 metrics obtained from validation set inference on models fine-tuned with <i>Baseline</i> dataset for 25 epochs and <i>Prompt</i> dataset 2 epochs.	47
3.2	Accuracy for models trained on <i>Baseline</i> dataset over a series of 25 epochs with 5 epoch increments.	48
3.3	Hardware configurations used for fine-tuning the various large language models along with their corresponding epochs and runtimes.	57
3.4	Sample inference times obtained from querying fine-tuned LLMs hosted on CPU.	58
4.1	Comparison between reported (literature) absorptivity and Drude-model calculated absorptivity at 1070 nm.	93
5.1	Milestones and proposed timeline for completing the thesis	103

CHAPTER 1

OVERVIEW

1.1 Introduction

1.1.1 Foundation of Powder Bed Additive Manufacturing

Many of the modern powder based additive manufacturing techniques such as Laser Powder Bed Fusion (LPBF), Selective Laser Sintering (SLS), and Electron Beam Melting (EBM) [72, 81] inherit foundational concepts from an early process developed known as Stereolithography (SLA) [109, 243]. Invented by Charles W. Hull, the SLA process was patented in 1984 and further developed into the company that known as 3D Systems Inc [109]. The general process outlined in the patent utilizes geometries defined in a computer-aided design (CAD) to iteratively fabricate a desired part layer by layer through precise forward control, relying on the phase change of the material after exposure to an energy source [109].

Specific to Stereolithography, also referred to by other names such as *vat polymerization* or *resin printing*, this process utilizes photopolymerizable monomers as its base material which is cured into a solid phase with the selective exposure of laser irradiation [109, 243]. The liquid material is held in a vat and precise translational control (along the z direction) of the build plate prepares the next layer for selective exposure [109, 243]. Selective exposure is controlled along the x and y directions using a scanning system, often times a mirror based galvometer setup, to project the sliced geometry into the given layer [109, 243]. After exposure, the build plate moves down a prescribed distance defined by the layer height and a recoater blade passes over the layer to ensure even distribution of the material [109, 243]. This process is repeated until the part is fully fabricated and subject to further post processing such as heat and UV curing before it can be used in its final assembly. Since the inception of this technique, the process of SLA has been further refined to

improve efficiency by means of Directed Light Processing (DLP) [54] for selective light exposure and reversing build direction for reduced initial material requirements [243].

Selective Laser Sintering (or Solid Freeform Fabrication [132]) is an additive manufacturing process which utilizes many of the techniques introduced in SLA with modifications to operate in a powder based environment [35, 36, 101, 196]. Developed at the University of Texas at Austin by Joseph J. Beaman and Carl R. Deckard, the 1990 patent describes a method and apparatus to produce a part by applying successive powder layers and selectively sintering powder within the cross-sectional regions until a part is fully formed [36]. This approach expands the range of materials that can be utilized for additive manufacturing outside those of photopolymerizable monomers to that of polycarbonate [39, 102], silicon carbide [229], and various metal alloys [159, 168].

During the sintering process the powder particles agglomerate through partial melting of the material [101, 129, 132]. For polymer based powders, a metastable temperature window between the onset of crystalline and melting phases known as the “sintering window” producing a stable viscosity regime[196]. For metals, binding can be achieved through three mechanisms: solid state sintering, liquid phase sintering, and true melting [131]. Solid state sintering relies on the solid state diffusion of atoms and is often too slow for much of the prescribed laser velocities [131]. Liquid phase sintering utilizes two different materials (matrix and structure) with varying melting temperatures for the production of a “green part” [131]. The rapid scans of the laser melt the material with the lower melting temperature (matrix) allowing the capillary forces to infiltrate the higher melting temperature (structure) material where the two are then fused together in postprocessing heat treatment [131]. Lastly, true melting occurs with a single material at higher energy levels as to completely fuse metal powder grains without the formation of a green part and aligns more to process of Laser Powder Bed Fusion. [131].

Laser Powder Bed Fusion, also referred to by other names such as Selective Laser Melting (SLM) [143, 199, 205, 217, 231] or Direct Metal Laser Sintering (DMLS) [40, 124, 168]), is the process in which metal powder is fully melted

through the application of localized heat with a laser creating a melt pool [44, 108, 171, 172, 241, 249]. This process of precise powder melting within each layer is repeated until a fully part is produced. However, this liquid phase of the material gives rise to melt pool dynamics such as keyholing [108, 125, 166, 220] and balling [37, 94, 137] which can result in downstream effects in the final part such as porosity.

1.1.2 Tokenization in Large Language Models

Tokenization is an essential component of the Natural Language Processing (NLP) pipeline as it converts strings of human-readable characters into token representations which are then embedded into vectors for the large language model [22, 82, 201]. Raw text does not provide a suitable representation medium for models to train upon as it commands a large vocabulary and treats words as distinct units [201]. Thus, tokenization presents a more efficient representation of the data to the model as an embedding vector [230]. Tokenization methods include dividing character strings into word and subword units along with indexing frequently occurring sequences detected using Byte Pair Encoding (BPE) [201]. In order to retain positional data, methods such as sinusoidal positional encoding [230] or Rotary Position Embeddings (RoPE) [213] are added to the token embedding vectors. By converting the tokens to vector embeddings with positional data, the model is able to use the semantic and sequential patterns of the input to perform next token prediction from the representations learned during training [201, 213, 230].

Subword Neural Machine Translation

Subword Neural Machine Translation is a preprocessing method which text is segmented into subword units, specifically useful in encoding out-of-vocabulary (OOV) words. The approach proposed by Senrich et al. [201] implements an adapted version of Byte Pair Encoding [79] (BPE) (Section 1.1.2) to first generate the pair table for frequently occurring character sequences within the train text. This is similar to the pair table seen in the compressed output that original BPE produces, however with slight adjustment of merging char-

acters rather than bytes in order to suit the application of word segmentation [201]. Along with this, the compression routine is set to conclude after a given number of operations rather than the original BPE process of repeating until there are no more remaining bytes in the text [79]. This provides a tunable `num_operations` parameter which balances the frequency for complete words and subwords within the dictionary, improving the coverage of tokens during training. This allows for out-of-vocabulary words to be segmented into combinations of word and subword tokens

Byte Pair Encoding

Byte Pair Encoding was first introduced by Philip Gage [79] as a method of data compression useful in memory constrained environments due to its fast expansion routine. The compression routine of the algorithm looks for most adjacent byte pairs that occur most frequently within a given pass and replaces the pair with a byte that doesn't already exist within the data. This repeats until there is either no more frequent byte pairs or there are no more remaining unused bytes [79]. The expansion routine is performed over a single pass over the input file, where byte literals are passed directly to the output buffer and byte pairs are pushed onto a stack. Within each iteration, if the stack contains data the byte there is used as the next input byte, otherwise the next input byte is obtained from the input file.

1.1.3 Reasoning and Prompting

Chain-of-Thought

Chain-of-Thought (CoT) is multi-step prompting technique to elicit further developed answers from the large language model than simple standard prompting [127, 234]. In this method, the prompt is formatted in a manner such that a step-by-step answer is provided to an example question before a similar question is posed in the input [127, 234]. This facilitates reasoning within the model as it decomposes the prompt into a multi-step problem which allows for additional computations be allocated to these individual steps [234].

Standard Prompting

Model Input
<p>Question: Alice goes out to lunch and splits the bill with Bob and Charlie. The total cost for lunch is \$65 with everyone ordering the same entree with the exception of Bob ordering a \$5 soda. What should Alice, Bob, and Charlie each pay?</p> <p>Answer: Alice pays \$20, Bob pays \$25, and Charlie pays \$20.</p> <p>Question: Bob and Charlie go out to dinner and the bill comes out to \$50. Both order the same entree but Bob orders himself a \$10 appetizer and Charlie orders a \$5 drink. How much should each pay?</p>
Model Output
<p>Answer: Bob pays \$25, and Charlie pays \$25.</p>

Chain-of-Thought Prompting

Model Input
<p>Question: Alice goes out to lunch and splits the bill with Bob and Charlie. The total cost for lunch is \$65 with everyone ordering the same entree with the exception of Bob ordering a \$5 soda. What should Alice, Bob, and Charlie each pay?</p> <p>Answer: Because Bob ordered an extra \$5 soda, he is responsible for that additional cost. The shared cost is now \$60 because $\\$65 - \\$5 = \\$60$. Since all three ordered the same entree, the shared cost can be divided into 3 resulting in $\\$60 / 3 = \\20 per person. Alice pays \$20, Bob pays \$25, and Charlie pays \$20.</p> <p>Question: Bob and Charlie go out to dinner and the bill comes out to \$50. Both order the same entree but Bob orders himself a \$10 appetizer and Charlie orders a \$5 drink. How much should each pay?</p>
Model Output
<p>Answer: Because Bob ordered himself a \$10 appetizer and Charlie ordered himself a \$5 drink, we would remove this from the shared total. The shared total now becomes $\\$50 - \\$10 - \\$5 = \\35. Since Bob and Charlie ordered the same entree, the cost should be the same for each $\\$35 / 2 = \\17.5 per person. Bob pays \$27.5 and Charlie pays \$22.5.</p>

Figure 1.1: Hypothetical comparison of outputs between standard prompting process to that of the chain-of-thought reasoning process.

For example, while constructing the prompt rather than simply stating the direct answer to a given problem, the answer is formatted in a way to provide the granular steps taken to arrive at an answer [234] (Fig. 1.1). This method is particularly useful in facilitating fidelity in multi-step arithmetic problems along with providing interpretable insight into reasoning within the LLM [234].

In addition to formatted user prompts, CoT reasoning provides a useful avenue to monitor large language model outputs for potential exploits that may produce misaligned behavior output [28]. This has been shown with the monitoring of verbose CoT outputs from larger models (i.e. o3-mini) using weaker models (i.e. GPT-4o) to prevent reward hacking schemes [28]. For example, *Baker et al.* [28] highlights an example where by monitoring the CoT of a model’s trajectory using a separate agent, a reward hacking scheme of modifying unit tests to always pass is thwarted. This proves useful in directing the model to complete tasks using the correct approach rather than choosing the simpler, often incorrect, approach. However, the authors have

found that given too much optimization the model can learn hide its intent within the CoT producing avenues where in which hallucination can occur [28, 169].

Zero-Shot Chain of Thought

With the increasing size of Large Language Models, Zero-Shot Chain-of-Thought has been shown to be sufficient in eliciting deeper thought responses without the need for step-by-step examples [127]. Rather, a simple addition to the prompt such as “Let’s think step by step” would be sufficient in encouraging the model to produce a more well formed answer [127]. This enables a minimalist approach to probe for complex reasoning with the large language model leveraging the large corpus of data that the model has been trained on [46, 127].

ReAct

ReAct (Reason + Act) is a general paradigm that combines reasoning and actions within the large language model to utilize feedback to make informed choices for the next set of actions [240]. By utilizing prompt based approach to navigating through an action space, ReAct is able to update its current policy by reasoning over it’s current context and observations [240]. This is achieved by decomposing a given task into a smaller set of steps similar to the Chain-of-Thought process [234, 240]. At a given timestep (t), each step consists of a language space action (\hat{a}_t) which Yao et al. [240] refer to as *thought* or *reasoning trace*, an environmental action (a_t) such as a tool call, and an observation (o_t) which is the result of action (a_t). The LLM generates a policy ($\pi(a_t|c_t)$) for the next action (a_t) given the current context (c_t) which consist of all actions and observations from previous timesteps. A language space action or aformentioned *thought* is performed to update the context ($c_{t+1} = (c_t, \hat{a}_t)$) allowing for dynamic policies which can be adjusted with feedback [240]. Further implementation details for the ReAct paradigm is discussed in Section 1.1.4.

1.1.4 Agentic Tool Calling

WebGPT

WebGPT is regarded as one of the earliest examples of LLM enabled tool calling [157]. In this work a fine-tuned GPT3 model [46] utilizes a written summary of the browser based environment along with navigation commands to answer prompted questions [157]. The model is capable of issuing a command such as `Search`, `Scrolled down <1, 2, 3>`, `Scrolled up <1, 2, 3>`, `End: Answer`, etc. to obtain information from the environment before composing a final answer [157]. Reinforcement Learning from Human Feedback (RLHF) and behavior cloning is used to fine-tune of the GPT3 model provide more accurate answer and execute the correct commands. During evaluation, 56% of these web enabled response produced answers that are preferred by human participants and provides benefits in reasoning transparency as the entire thought process for constructing answers is visible [157].

ReAct

As mentioned in Section 1.1.3, the ReAct paradigm is a multi-step process that operates by dynamically adjusting its policy given the updated context within each step [240]. Each step is composed of a “Thought”, “Action” and “Observation” which the LLM is prompted to complete [240]. The “Thought” is the language space action that the LLM produces to create the updated context from the existing context space after both an Action and Observation are performed [240]. “Actions” are then performed by parsing the subsequent output from the LLM to search for tools that match a specific syntax (i.e. `search[entity]`, `lookup[string]`, or `finish[answer]`). The respective function is then executed with the provided argument producing an “Observation” which is then appended to the context before moving onto the next step. This “Thought”, “Action” and “Observation” process is repeated until either the LLM produces an “Action” consisting of `finish[answer]` or an iteration limit is reached [240]. During this process, the CoT reasoning is visible throughout each step providing transparency into the mechanisms used

to construct the final answer [240].

1.2 Structure of the Thesis Proposal

This proposal is structured to summarize prior research conducted to support the proposed work regarding agentic process monitoring. Specific to prior research, this proposal covers the use of a video transformer based model for *in-situ* process monitoring, fine-tuning large language models for enhanced domain knowledge, and the development of an agentic system for intelligent automation.

Chapter 2 describes the work done in process monitoring utilizing a video transformer based model for correlating *in-situ* thermal images to *ex-situ* porosity. The data is obtained experimentally with the thermal images taken using a two color pyrometer and the porosity data collected through computed tomography. The transformer based approach was able to achieve an R^2 score of 0.57 for porosity quantification and an Intersection over Union score of 0.32 which indicates that porosity in the final part can be detected from anomalies in thermal images [172].

Chapter 3 explores the application of fine-tuning on a range of large language models such as DistilBERT [194], SciBERT [38], T5 [11], and Llama 3 [93] for the prediction of potential defect regimes. These models were trained on a dataset of melt pool dimensions and their defect classification provided by MeltpoolNet [20] along dimensions and classification obtained through computational fluid dynamic simulations. The fine-tuned models displayed robust predictive capability with a *Baseline* accuracy of 94% and a *Prompt* accuracy of 82% showing that relatively small models can be fine-tuned to perform well on domain specific tasks in additive manufacturing [171].

Chapter 4 investigates the use of an agentic system for the task of alloy evaluation in additive manufacturing. Here, the model context protocol is leveraged to enable a multi-agent system to analyze potential lack of fusion defect regimes of proposed element compositions. This is achieved through a set of tool calls to ThermoCalc [222] in order to obtain material properties and subsequent tool calls to a Rosenthal based melt pool equation for

the approximation of melt pool dimensions. This work showcases the intelligent automation of alloy evaluation through the use of tool call enabled large language models.

Chapter 5 outlines the proposed works of developing an agentic system for process monitoring and parameter tuning for selective laser sintering (SLS) and further work to enable the large language model to continuously learn from previous iterations. For this the experimental process will utilize an open source SLS machine and utilize its available sensors for process monitoring and control. These interactions will be stored in a vector database in order to deploy the large language model into a continuous learning environment where it is able to make informed decisions on past actions.

CHAPTER 2

THERMOPORE: PREDICTING PART POROSITY BASED ON THERMAL IMAGES USING DEEP LEARNING

2.1 Introduction

Additive manufacturing (AM) presents a competitive alternative to the conventional approaches in manufacturing with the advantages of efficient material utilization, design consolidation, and fast iteration [20, 35, 100, 183]. However, a significant area of improvement lies within defect prevention as printed parts present their own set of challenges in porosity, distortion, and cracking[183]. These issues are often uncovered through *ex-situ* non-destructive testing methods and can sometimes be addressed through lengthy post-processing means such as hot isostatic pressing (HIPing) before they are certified [66, 170]. With *in-situ* process monitoring, a digital twin of the fabrication process can be created and segments of the certification process can be conducted in parallel[33, 80, 126].

Laser powder bed fusion (LPBF), relies primarily on established process maps [18, 56, 92] to determine the optimal machine settings that minimize defects within the finished part. Most commonly, these process maps explore the power and velocity space to determine a combination of two that would result in a sufficiently dense part. Informed control over these process parameters and others such as hatch spacing [237], layer height [209], and raster pattern [149], can greatly affect the part's porosity, microstructure [87], and surface finish [209]. However, even within build conditions with nominal process parameters, defects such as porosity remain an issue [207].

In-situ process monitoring offers a means to resolve this issue as information obtained from the build process can assist in resolving many of the technical challenges encountered during part fabrication [207, 223]. Many of these defects and their precursors such as part distortions [41], surface roughness [103], or keyhole formation [186, 220] exhibit signals which with the appropri-

ate sensors can be detected before *ex-situ* sample analysis. These indicators can be applied alongside the build process to analytical and machine learning models in order to obtain the necessary feedback to adjust process parameters for the build. This feedback loop would be optimized to reduce the number of part defects through both preemptive and responsive measures. [77, 146]. In addition, reconstructing the porosity map can significantly accelerate the part certification process as the knowledge of the porosity map can expedite qualification through observations of statistics alone[55, 68, 126, 200, 210].

Thermal imaging demonstrates effectiveness as an *in-situ* process monitoring technique as evidenced by previous studies which have explored comparing melt pool images to computational fluid dynamics simulations [156], mathematical equations [122], and 3D surface maps[96]. Further exploration of this technique has shown effectiveness in applications such as defect detection and correction within the build process either indicating likely porosity given a thermal image of a melt pool [153] or material extrusion correction in large scale additive manufacturing[42, 43].

Analytical solutions such as Rosenthal's equation [192] provide a foundational method to determine nominal process parameter regions within laser power and scanning velocity space. This equation can be adapted to provide depth and width estimates of the melt pool given specific process parameters such as preheat temperature, power, and velocity which can be applied to the selection of nominal parameters for hatch spacing and layer height. However, this method poses limitations as solutions provided by Rosenthal's equation are only suitable for melt pools within the conduction regime [99, 112, 192]. This leaves areas out that are not captured through analytical models such as melt pool behavior in the keyhole mode and process conditions such as scan strategies.

Much attention has been directed towards machine learning to fill this gap between the projection of these analytical models and their applied results some of which include process parameter optimizing [34, 166] and fatigue life prediction [244]. In this paper we explore the application of machine learning towards the quantification and spatial localization of pores within a sample given the *in-situ* monitoring data of thermal images. These predictions can

then be utilized to create a digital twin of the built sample and perform qualification and certification tasks in parallel to the sample fabrication[33, 80, 126].

For the task of pore quantification a three dimensional Convolutional Neural Network (CNN) was utilized to extract features within a provided sequence of thermal images and provide a singular scalar prediction of the expected number of pores. Models such as *ImageNet*[130] have shown the effectiveness of 2D CNNs with image classification tasks and other models such as *C3D*[226] have applied this technique to extended over a sequence of images. Training a 3D CNN model with the objective of pore quantification enables the identification of pore counts within a build layer prior to any *ex-situ* sample analysis.

The task of pore localization utilizes a Video Vision Transformer (ViViT)[25] which is suited to capture the spatial and temporal features within the sequence of thermal images through subdividing the input into patches. The original implementation of the ViViT model is structured to provide a classification output[25], however for the purposes of pore localization the classification head is replaced with a dense prediction head which retains the spatial information of the input sequence. Our network implementation utilizes a dense output which directly correlates the spatial and temporal information into a 2D pore localization prediction. This network builds off the work by Ranftl et al.[184] where fusion blocks and convolutional layers are added to a vision transformer to provide depth predictions of a given image.

Application of these aforementioned machine learning techniques alongside the build process opens up the possibility to acquire expedited *ex-situ* sample insights and fabricate parts within a closed feedback loop. This has the possibility to reduce labor and materials costs as parts fabricated through laser powder bed fusion rely on *ex-situ* post-build inspection and testing to qualify parts and identify potential defects [55, 63, 67, 76]. This is often a tedious process as cross-sectional imaging or x-ray computed micro-tomography (CT) is required to analyze these parts for defects such as keyholing or lack of fusion porosity. [156, 166]. However, if analogous information is obtained earlier during the build process through the creation of a digital twin, problematic

builds can be terminated earlier or dynamic adjustments can be applied once the presence of defects is detected to reduce material waste and costs.

Previous work towards establishing a correlation between the *in-situ* and *ex-situ* dataset has been conducted with sensors such as thermal monitoring, acoustic recording, or photodiode readings[57, 76, 135, 188]. With the recent work by Li *et al.*, the usage of acoustic *in-situ* monitoring was applied to recognize five laser powder bed fusion defects to an accuracy of 99.12%[135], highlighting the effectiveness of *in-situ* process monitoring. Work by Coeck *et al.*[57] explores the effectiveness utilizing photodiode sensors to determine lack of fusion porosity establishing a correlation directly between *in-situ* process monitoring to *ex-situ* porosity obtained with computed tomography. Our work explores an emerging approach to correlate *in-situ* pyrometry data to *ex-situ* porosity through the usage of deep learning approaches such as convolutional neural networks or transformers.

For this purpose, we have constructed a digital twin framework called *ThermoPore* for extrapolating defect critical porosity information from a sequence of *in-situ* thermal images. This framework extends existing additive manufacturing digital twin work, a data-based approach to develop *product twins* utilizing melt pool dynamic simulations and *in-situ* process monitoring techniques[126, 178, 247]. This work focuses on the utilization *in-situ* pyrometry data to construct characteristics for a *product twin* such as pore count and pore localization. As outlined in Fig. 4.1, the general architecture of this framework consists of two separate deep learning models (Fig. 4.1d and 4.1e) which extract embeddings from a sequence of *in-situ* thermal images (Fig. 4.1c). These embeddings correspond to the quantitative and localized information of pores obtained from the segmented computed tomography data (Fig. 4.1b). The predictions from these models indicate the degree of porosity that can be anticipated from a given sequence of thermal images. By leveraging the capabilities of Convolutional Neural Networks and Video Vision Transformers, *ThermoPore* enables efficient evaluation of laser powder bed fusion printed parts.

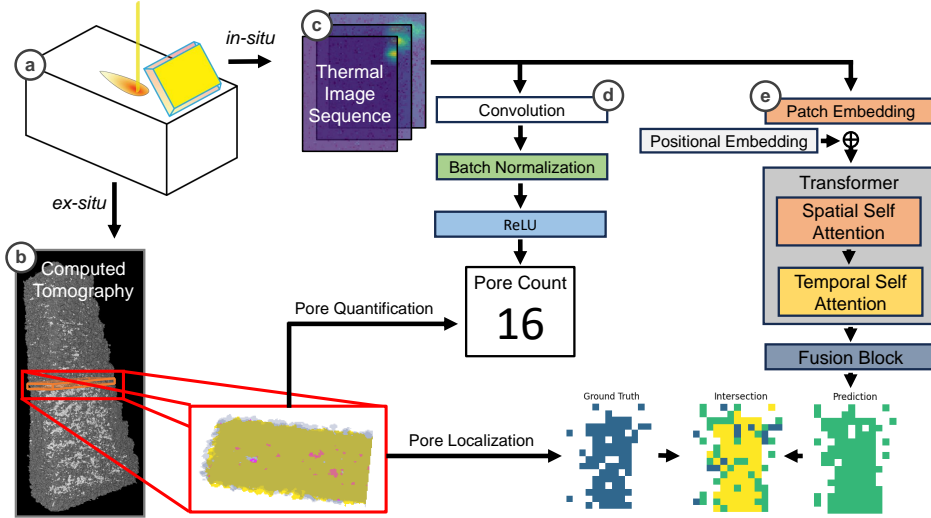


Figure 2.1: A sequence of 200 thermal pyrometry images (4.1c) providing absolute temperature values of the build plate taken *in-situ* (4.1a) are provided as input data for models for pore quantification (4.1d) and pore localization (4.1e). These two separate models utilize a CNN and ViViT with dense output heads to produce a scalar number of pores and 2D mapping of expected porosity regions respectively. Metrics derived from *ex-situ* CT data for the corresponding build layer are used as ground truth values for each model (4.1b).

2.2 Methodology

2.2.1 Spacing and Velocity Samples

Sample Fabrication and Data Acquisition

This paper analyzes two samples, one with variable hatch spacing (*Spacing*) and the other with variable scan velocity (*Velocity*). Both of these samples were manufactured using LPBF equipment (ProX DMP 200 from 3D Systems) with AISI 316L stainless steel powder and a constant laser power of 103 W[26, 153]. These samples were designed with a staircase structure (Fig. 2.2a) with each sample comprised of 10 separate steps and each step consisting of a 16 build layers with a 30 μm layer height. Within each of these steps a different

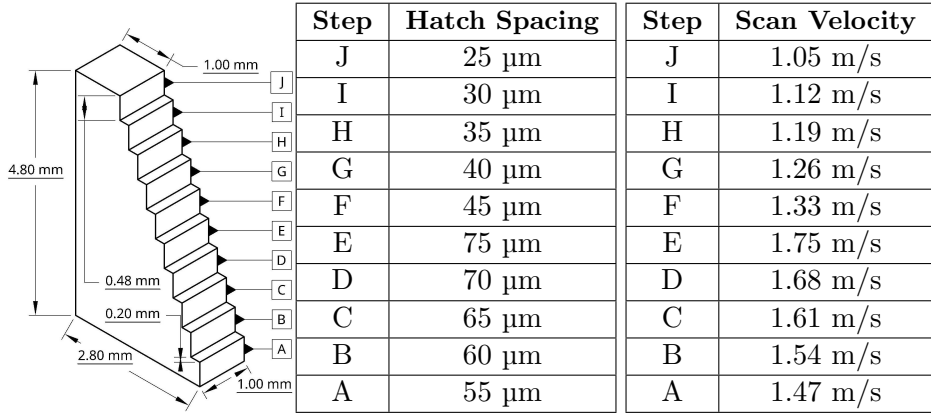


Figure 2.2: Each sample (2.2a) contains 10 different process parameter combinations with the *Spacing* sample (2.2b) exhibiting varying hatch spacing and the *Velocity* sample (2.2c) exhibiting varying scan velocity.

combination of process parameters were implemented with changes to either hatch spacing (Fig. 2.2b) or scanning velocity (Fig. 2.2c). The expected dimensions of each sample are 4.80 mm × 2.80 mm × 1.00 mm in height, length, and width respectively[26]. Each step consisted of dimensions 0.48 mm in height and ranged from 1.00 mm to 2.80 mm in length, increasing in length by 0.20 mm from the top of the sample to the bottom. The *Spacing* sample with varying hatch spacing was built with a constant 1.4 m/s scan velocity and the *Velocity* sample with varying scan velocity was built with a constant 50 µm hatch spacing [26]. A *normal* rastering pattern consisting of line scans parallel to the build axes, orthogonal to the previous layer was utilized as the scan strategy for both samples.

In-situ Pyrometry

Absolute temperature estimations were calculated from thermal radiation captured by a Stratonics two-color pyrometer receptive to light emitted at 750 nm and 900 nm, calibrated with NIST-traceable tungsten lamp[153]. Images were captured with a frame rate within 6 - 7 kHz and a 90 µs exposure.[153] Temperature estimations without in depth knowledge of emissivity parameters

were performed with a grey-body assumption.[153]. Synchronization between the LPBF equipment and pyrometer were achieved via Transistor-Transistor Logic (TTL) triggering producing 1000 frames of $65\text{ px} \times 80\text{ px}$ images within each build layer[153]. This translated to a $1365\text{ }\mu\text{m} \times 1680\text{ }\mu\text{m}$ resolution with approximately $21\text{ }\mu\text{m}$ per px. This presented a total of 159,000 images taken for each sample and with initial screening applied to filter out "empty" images, reducing the total number of frames down to 20,469 and 20,187 for *Spacing* and *Velocity* samples respectively. Within the *Spacing* sample, the melt pool temperatures observed a consistent spread between $1400\text{ }^{\circ}\text{C}$ to $1650\text{ }^{\circ}\text{C}$ through all build layers, which aligns with the expected behavior of parts fabricated with constant power and velocity.

Within the range of potential melt pool temperatures, lack of fusion porosity is expected toward the lower temperature bound due to insufficient melting and keyhole porosity at the upper temperature bound. Keyhole porosity results from the collapse of the rear keyhole, driven by recoil pressure, which peaks at the vaporization temperature of the material but is also influenced by ambient pressure [233]. Studies have shown that lower ambient pressures reduce porosity by lowering the vaporization temperature, thus affecting recoil pressures [118, 245, 252]. At the lower bound, lack of fusion porosity occurs when melt pool temperatures are below the material's melting point, influenced by factors like melt pool dimensions, layer height, and hatch spacing[218]. For 316L Stainless Steel, with a liquidus temperature of $1437.11\text{ }^{\circ}\text{C}$ (1710.26 K), solidus temperature of $1410.53\text{ }^{\circ}\text{C}$ (1683.68 K), and vaporization temperature of $2860.85\text{ }^{\circ}\text{C}$ (3134 K)[154], these values establish the temperature boundaries for avoiding porosity. However, due to various factors like ambient pressure affecting the vaporization temperature, machine learning models are used to analyze temperature sequences and predict porosity in computed tomography data.

Ex-situ Micro-computed Tomography (CT)

Micro-computed tomography analysis was performed using a Zeiss Xradia 520 Versa at the maximum output power of 10 W and tube voltage of 140

kV with the sample positioned 11.1 mm from the source [26]. Scans were taken at a cubic voxel size of 3.63 μm and with a build layer height of 30 μm , this equated to approximately 8.26 voxels per build layer. The obtained scans for the *Spacing* and *Velocity* samples were bounded in the Z \times Y \times X directions by 5.05 mm \times 3.00 mm \times 1.35 mm and 5.05 mm \times 3.17 mm \times 1.44 mm respectively (Fig. 2.3a) [26]. The extracted 3D representation for both *Spacing* and *Velocity* samples extended 1410 voxels \times 900 voxels \times 430 voxels along the Z, Y, and X axes.

With the voxelized dataset obtained from both the *Spacing* and *Velocity* samples, further actions were performed to extract porosity attributes. This included each pore's unique identifier, equivalent diameter, centroid, number of voxels, and minor and major axes. Of these traits, the pore's unique identifier was primarily used to determine the boundaries of each individual pore which was further processed to labels used for the Pore Quantification and Pore Localization tasks.

2.2.2 Pyrometry and Micro-computed Tomography Datasets

Pyrometry and Micro-computed Tomography Alignment

Data Alignment

To ensure accurate correlation between pyrometry input and corresponding micro-computed tomography pore labels, effective alignment of the two datasets is essential. In the pyrometry dataset, the capture area (Fig. 2.3c) needs to be considered as it is limited to 80 px \times 65 px (1680 μm \times 1365 μm) area of the sample, leading to raster patterns of lower build layers (steps A - F) to extend further than the camera's viewport [153]. As mentioned, initial screening filtered out many of these empty frames by applying a minimum threshold on each frame's peak value from long wavelength data[153]. This method removed the frames where the melt pool was out of view, however still included some frames where spatter likely occurred.

In-situ thermal images and slices of *ex-situ* CT data shared the same origin at the top left (Fig 2.3 b). Small offsets were then applied to align the X and

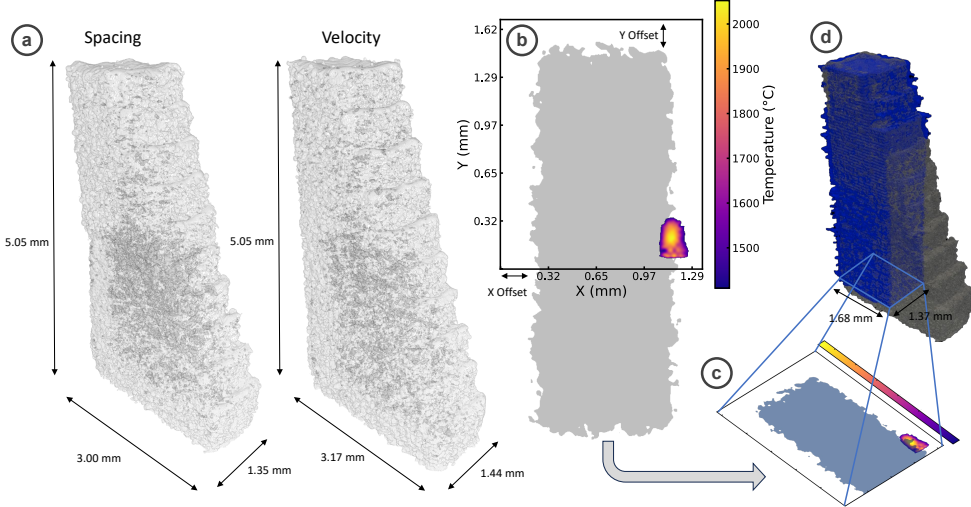


Figure 2.3: Visualization of segmented CT porosity within overall sample for *Spacing* and *Velocity* samples (2.3a). Figure 2.3b superimposes the pyrometry image directly over the corresponding CT data with alignment offsets applied along the X and Y axes, using the top left corner of both as the origin. Alignment for a build layer is visually validated (2.3c) as only a subset of the built sample is visible through the lens of the pyrometer (2.3d).

Y directions of CT to the thermal image. The provided Z direction offsets were used as starting points to align the CT data to the corresponding build layer. The Z alignment for both samples were visually verified through manual alignment of the scan path of thermal images and the a top down view of the corresponding CT layer. Step G (Fig. 2.2a) within both samples was the first section of the sample where the entire scan path is in complete view of the thermal camera and was used as a reference point to align the CT data. Both samples (*Spacing* and *Velocity*) were offset by a total 5 build layers (~9 voxels per build layer) in total.

Pore Thresholding

A CT resolution of 3.63 μm per voxel allowed for the capture of distinct shapes and contours associated with porosity, however this fine resolution

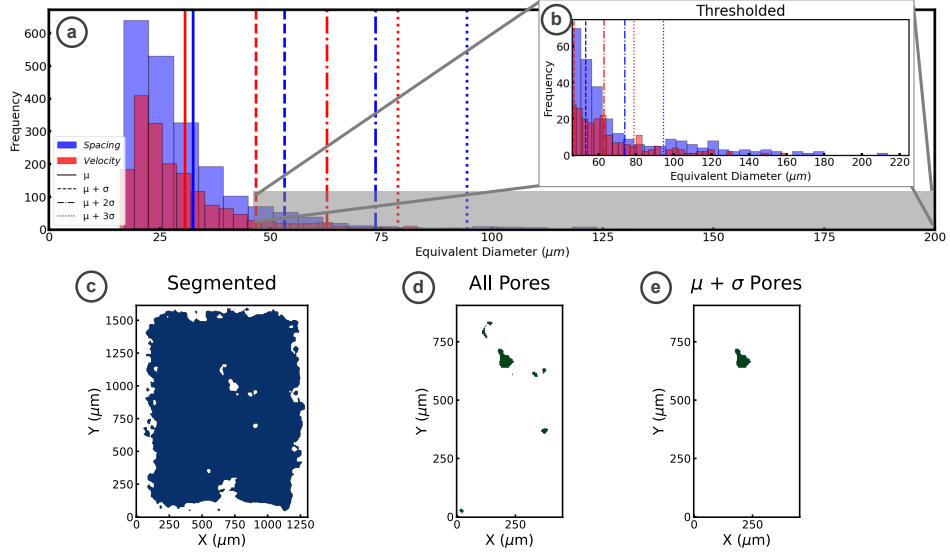


Figure 2.4: The *Spacing* sample on average consist of larger pores with a standard deviation of 20.5 μm compared to the *Velocity* sample’s standard deviation of 16.0 μm (2.4a). The tighter distribution of *Velocity* pores are visible in the thresholded distribution of equivalent pore sizes (2.4b) within the slices of the CT data. The segmentation of pores within the sample (2.4c) relied on a minimum of 100 voxels (11.4 μm equivalent spherical diameter)[153] in order to register the contiguous cluster of voids as porosity (2.4d) and an increase in the minimum size further removed smaller pores (2.4e).

also resulted in recording scattered distributions of small voids. Accurately predicting these small voids is a difficult task for a model as these defects could be the result of gas porosity [110] or rogue flaws [187] and may have precursors not visible to thermal imaging. To achieve greater correlation between the pyrometry data and CT data, our attention focused on larger diameter pores that can be attributed to factors such keyhole porosity or lack of fusion porosity. In keyholing, pores generated by the vapor column during builds resulted in an average diameter of 47 μm [205] and lack of fusion pores with diameters dependent on the height and width of melt pool and corresponding build layer [48].

The mean Equivalent Spherical Diameter (ESD) for each sample was compiled in order to obtain minimum threshold values 1 standard deviation above

the mean. In the *Spacing* sample, pores exhibited an average diameter of 32.59 μm and a standard deviation of 20.60 μm , resulting in a minimum ($\mu + \sigma$) ESD threshold of 53.19 μm . In the *Velocity* sample, pores had an average diameter of 30.78 μm and a smaller standard deviation of 16.01 μm resulting in a minimum ($\mu + \sigma$) ESD thresholds of 46.79 (Fig. 2.4b).

2.3 Porosity Reconstruction

The quantity of pores and their position within the build layer was reconstructed with machine learning inferencing upon a sequence of thermal images. With the set of *in-situ* and *ex-situ* data, the tasks of predicting the number of pores and the approximate location of these pores within the various build layers were achieved using a CNN model and a ViViT model with dense prediction heads respectively.

The number of pores corresponding to a sequence of thermal images were predicted using a CNN model. In this task both the application of rotational transforms on the input sequence and the volumetric depth utilized for pore count were treated as variables. In some cases pores, such as those resulting from keyhole porosity [233], can form below the build layer. Also within the CT data, there exist pores which extend beyond one build layer into multiple build layers. In order to account for this, labels were derived from counting the set of unique pores within a specified volumetric depth corresponding to 1, 2 or 3 build layers below the thermal image by referencing each voxel’s pore id. The quality of these predictions is measured using Root Mean Square Error (RMSE) and R^2 score.

The localization of pores was predicted using the same sequence of thermal images and utilized a ViViT model with a dense prediction head to indicate sections expected to be porous. The labels for this task were obtained by downsampling the CT data for the build layer equally along all axes in order to provide a coarse porosity estimates for the model to train and predict. In addition, the effect of applying rotational transforms on the input sequence and minimum pore ESD thresholds for label compilation were investigated. The quality of the predictions was measured using an Intersection over Union

(IoU) score, considering the overlap of the area of predicted porosity over that of the label.

2.3.1 Porosity Count

This task investigates the extent in which sequences of thermal images can quantify the number of pores that exist within the sample build layers. Without the application of a $\mu + \sigma$ equivalent diameter threshold, the *Spacing* sample consists of 2069 pores and the *Velocity* sample consists of 1811 pores. The input for this model consists of a sequence of 200 64×64 pixel thermal images of the build layer. The labels were obtained from corresponding build layer region of the CT sample data, where the number of unique pore identifiers were counted. Each build layer consisted of 9 voxels in depth and this volume was extended to a depth of 18 and 27 voxels to obtain pore counts extending down 2 and 3 build layers.

In this task a CNN model composed of 4 convolutional layers and 2 fully connected layers reduce the input set of 200 64×64 pixel images into a scalar value of the number of unique pores within the build layer (Fig. 2.5). A 3×3 pixel kernel is convolved on top each image with a stride of 2 and a padding of 1. Within each layer the number of channels is reduced by a factor of 2 and batch normalization and ReLU non-linearity activation function are applied. The output of the CNN layers are reshaped into a 2 dimensional tensor before they are passed to the two fully connected layers which output a single scalar value which quantifies the number of pores within the build layer.

A CNN operates by leveraging convolutional layers to extract features from input images hierarchically. In the initial layers, low level features such as edges and gradients are detected through convolutional operations where the kernel moves across the input image, computing dot products and producing feature maps [114, 130, 139, 226]. Activation functions such as ReLU apply non-linear transforms and allow for the capture of complex patterns. The following layers then build upon these low level feature maps and repeat this task of transforming the raw pixel values into the outputs for a specific task [130]. These tasks are determined by the final layers of the network which

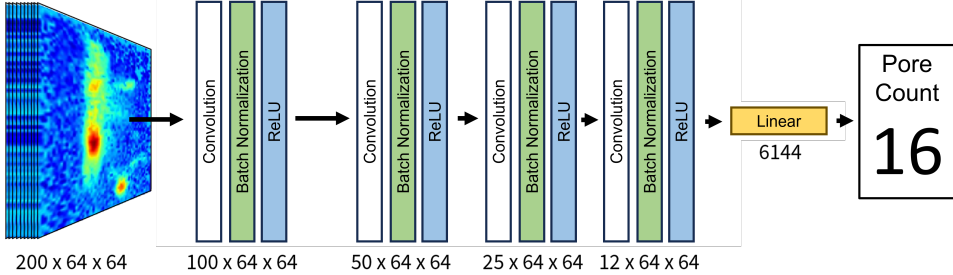


Figure 2.5: A standard convolutional neural network with a kernel size of 3 pixels and a stride of 2 filters the features within an image down over 4 layers to a singular scalar value indicating the expected number of pores from the sequence of thermal images.

utilize fully connected layers to shape the output to perform classification, regression, or reconstruction.

Due to dataset size constraints, a 75 / 25 train test split of the data was used for model training. The train test split occurred within the 16 build layers of each of the 10 sample steps of either the *Spacing* or *Velocity* sample. This split within sample steps was implemented to provide an equal distribution of processing parameters between the train and test sets for the model. This provided an input label set of 120 training pairs and 39 testing pairs for the either of the samples. Our dataset implementation allowed for the model to train on either the *Spacing*, *Velocity*, or on a combination of both datasets with the *All* dataset. For this regression task, a mean squared error was utilized as the loss function and the predicted value from the model is rounded to the nearest integer. Each of the models were trained from 500 epochs with a learning rate of 0.0001 using the ADAM optimizer.

In addition, data augmentations of the input sequence in the form of rotational transforms for the entire video sequence were applied. Data augmentation provides a means to artificially expand an existing set of data in order to improve the generalization ability and robustness of the model[130]. Typical transformations change the input image applying one or a combination of rotations, translations, flips, scaling, and cropping. In this application we focus only on applying rotational transforms ranging between 0° to 180° and avoid

alterations to the contrast or brightness that would affect the raw temperature value.

2.3.2 Porosity Localization

The localization task identifies areas within the build layer where pores are likely to form through analyzing the build layer’s sequence of 200 64×64 pixel thermal images. A video vision transformer (ViViT) provides an applicable architecture to thoroughly analyze the series of input frames to extract positional features through use of spatial and temporal attention.[25] In our model implementation a sequence of thermal images for a specified build layer is provided to the model to map to localized porosity labels obtained through alignment and extraction of the CT data. Within the CT data a build layer is a size of $9 \times 423 \times 520$ voxels. The areas that indicate porosity area then extracted and downsampled by a factor of 24 to a coarser 2 dimensional $1 \times 16 \times 16$ voxel shape to provide a general area in which porosity is expected (Fig. 2.9).

For this task a video vision transformer model with a dense prediction output is utilized to localize pores within the sample space. This model is composed of a spatial transformer layer with 4 sub-layers and a temporal transformer layer with 5 sub-layers both with 8 heads and a dimension of 256 (Fig. 2.6). Afterwards the class tokens resulting from each of the transformer layers are removed and the output is passed into a feature fusion block which performs residual convolution and provide a fine grain prediction. A series of 4 convolutional layers and ReLU non-linearity layers are applied before ultimately passing through a sigmoid activation function. The sigmoid activation function constrains the output between 0 and 1, providing a probability distribution of the existence of porosity at this location of the sample. To compare the outputs of this model to the ground truth, the outputs are converted to binary representations to the existence of porosity, which allows for the calculation of IoU performance metrics.

Attention within a transformer is comprised of three learnable components: The query vector $\{\mathbf{q}_i\}_{i=1}^{N_q}$, key vector $\{\mathbf{k}_i\}_{i=1}^{N_k}$, and the value vector $\{\mathbf{v}_i\}_{i=1}^{N_v}$

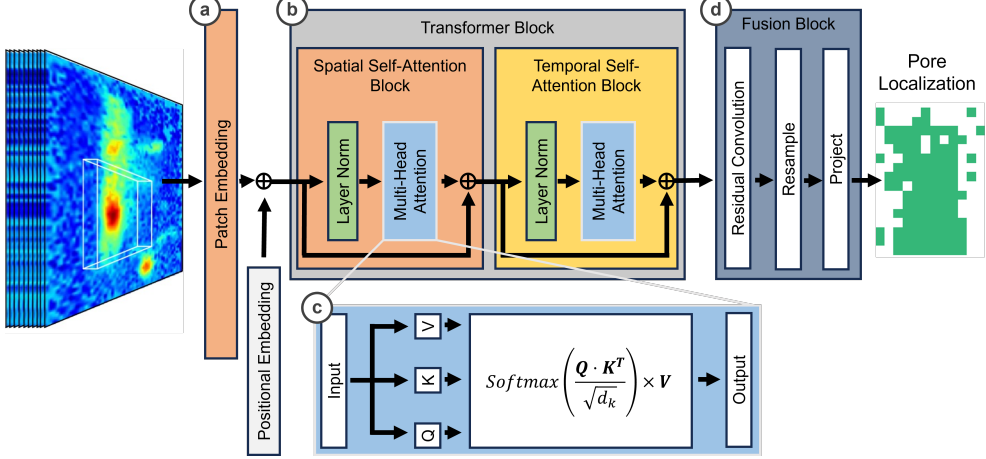


Figure 2.6: The input sequence of thermal images are sliced into a set of patches (2.6a) where 4 and 5 sublayers of the respective spatial and temporal self attention are applied (2.6b). Each self attention block consisted of 8 attention heads (2.6c) of a dimension of 256. A feature fusion block (2.6d) applies residual convolution and a dense prediction head produces a 2 dimensional output indicating regions of expected porosity.

given that $N_k = N_v$ [27, 136, 230]. In the attention mechanism, the query vector retrieves contextual information from the key vector and generates an output based on the weighted sum of corresponding value vectors. Contextual information is retrieved in the form of an attention score which is the scaled dot product between the query vector and the key vector: $\frac{\mathbf{q}_i \cdot \mathbf{k}_j^T}{\sqrt{d_k}}$ [230]. The attention score is then used in the calculation of weights (α_{ij}) which apply a Softmax over the individual contribution of each attention score (Eq. 2.1) [27, 136, 230]. Each token's numerical encoding along with its relevance to other tokens is calculated from the cross product between the value vector and weights resulting in the attention mechanism: $\text{Softmax}\left(\frac{\mathbf{Q} \cdot \mathbf{K}^T}{\sqrt{d_k}}\right) \times \mathbf{V}$ [27, 136, 230].

$$\alpha_{ij} = \text{Softmax}\left(\frac{\mathbf{Q} \cdot \mathbf{K}^T}{\sqrt{d_k}}\right) = \frac{e^{\frac{\mathbf{q}_i \cdot \mathbf{k}_j^T}{\sqrt{d_k}}}}{\sum_{k=1}^N e^{\frac{\mathbf{q}_i \cdot \mathbf{k}_k^T}{\sqrt{d_k}}}} \quad (2.1)$$

In the case of a Vision Transformer (ViT), an image is divided up into self

attention patches via patch embedding, passed through the transformer encoder, and utilized through a classification head[25, 69]. Within patch embedding, each patch has a fixed pixel size in height and width and its embedding is derived through flattening and linear projection[25, 69]. Class and position are applied to the embedding before passed through the transformer encoder composed blocks of layer norm, multi-head attention, and MLP layers after which a classification head is attached.[69]

The dataset utilizes the same 75 / 25 train test split within the sample steps for all the *Spacing*, *Velocity*, and *All* variants. The model was trained for 1000 epochs utilizing a binary cross entropy loss function for the binary prediction of a voxel’s porosity classification. An ADAM optimizer along with a cosine decay learning rate scheduler with an initial 10 epoch warm up period from learning rates 0.00001 to 0.0001 is applied to help with regularization and stabilization [91].

2.4 Results and Discussion

2.4.1 Porosity Count

The number of pores within a volume of the sample was predicted from a sequence of thermal images using a CNN model trained on either the *Spacing*, *Velocity*, or *All* dataset. Hyperparameters such as the utilization of rotational transforms and the number of build layers involved in the compilation of the pore count were investigated.

Table 2.1 outlines the model’s performance according to its training dataset and indicates the data augmentation procedures that were applied and the various depths used to calculate pore count. Models with datasets spanning 1 build layer exhibited the lowest error and highest R^2 with a minimum RMSE score of 7.84 from the *Velocity* sample and a maximum R^2 score of 0.57 from the *Spacing* sample. The RMSE aims to measure the average magnitude of errors such as the degree in which the prediction deviates from the target. The R^2 score captures the proportion of variance that can be attributed to explanatory variables. The alignment of the prediction and the corresponding target for each model (Fig.2.7) shows a general trend where there is a larger

degree of porosity within the build layers ranging from 60 to 100 and to a lesser degree elsewhere. Notably, build layers greater than 100 display lower amounts of porosity for all models regardless of dataset or data augmentation.

This is expected as both samples transition from non-nominal process parameters to nominal process parameters towards the middle of the sample (Table 2.2b, 2.2c) with the upper portion of each sample fabricated with ideal process parameters. For all models, areas where the sample was fabricated with nominal process parameters show a greater degree of clustering as pores are sparse and few. In earlier build layers, specifically those closer towards the middle of the sample a greater spread of predictions is seen (Fig. 2.7).

The model trained with the *Spacing* dataset without rotational transforms (Fig. 2.7 Bottom) achieved the highest R^2 score of all models with a score of 0.57. This indicates that the more than half of the variance within this model is able to be explained by the input data. However, the model trained with the *Velocity* sample and rotational transforms achieved the lowest RMSE score of 7.84 of all models on input data with significantly less variability as indicated with their lower R^2 scores. The model trained on the *All* dataset produced RMSE and R^2 scores inbetween that of models trained on either *Spacing* or *Velocity* datasets except in the situation for the case where rotational transforms were applied where it yielded a R^2 score of 0.07. The additional hyperparameter of various build layer depths displayed mostly worse RMSE and R^2 scores indicating that there exists a greater correlation between the thermal images and the build layer directly underneath it (Table 2.1). The exception to trend occurs within the *Velocity* dataset where R^2 score (0.36) observes a visible increase for label pairs extending to 2 build layers. This is seen to a lesser extent for porosity expanding to 3 build layers and aligns with the findings by Wang *et al.*[233] that keyhole porosity can travel well below the immediate build layer.

The RMSE and R^2 values align with what is expected of the two *Spacing* and *Velocity* datasets as the hatch spacing and scan velocity are the two variables that change between sample steps respectively. In the case of *Spacing* sample, the hatch spacing produces a visible signal in the form total rasters that is visible over the sequence of input frames. However, the *Velocity* sample

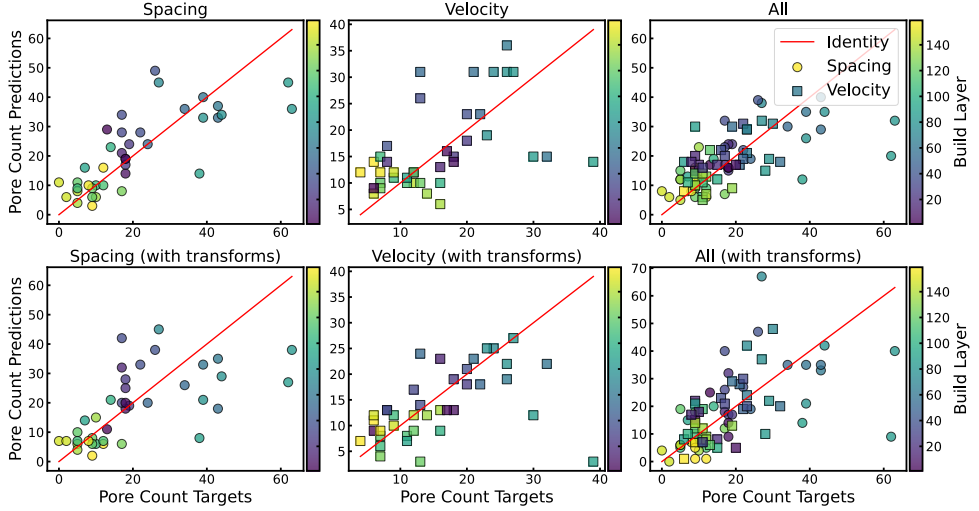


Figure 2.7: CNN pore count predictions plotted alongside target pore values for *Spacing*, *Velocity*, and *All* (combination of both datasets) for a depth of 1 build layer. In all plots the pore counts for build layers 100 - 160 are clustered near the origin as the upper half of the sample is composed of nominal process conditions. Of all the various implementations, the CNN model trained on the *Spacing* (Top Left) dataset without transforms shows the greatest level of alignment between the prediction and ground truth.

uses a consistent number of rasters traveling both vertically and horizontally across the build plate. The most significant visual signal in the *Velocity* sample is the distance the melt pool travels inbetween frames.

Within existing literature, our pore count model performs comparably to a similar study conducted by Coeck *et al.*[57] which detected the presence of porosity within 54 of the total 93 porosity samples before the removal of false positive results. Given the limited size and resolution of the training and testing dataset, the range of observed melt pools is restricted. Although an experiment for creating a dataset varying in power process parameters was conducted, challenges encountered during the data collection process prevented its use within our datasets. A larger dataset along with a higher resolution image would offer more examples and features for the model to train with and improve RMSE and R^2 performance metrics.

Dataset	Data Augmentation	1 Build Layer		2 Build Layers		3 Build Layers	
		RMSE	R ²	RMSE	R ²	RMSE	R ²
<i>Spacing</i>	Rotational	12.60	0.33	19.04	0.18	22.94	0.17
	None	10.14	0.57	18.46	0.23	19.75	0.39
<i>Velocity</i>	Rotational	7.84	0.09	11.41	-0.04	14.74	0.03
	None	8.08	0.03	8.95	0.36	13.25	0.22
<i>All</i>	Rotational	11.90	0.07	13.89	0.34	17.81	0.26
	None	9.73	0.38	14.57	0.27	16.88	0.34

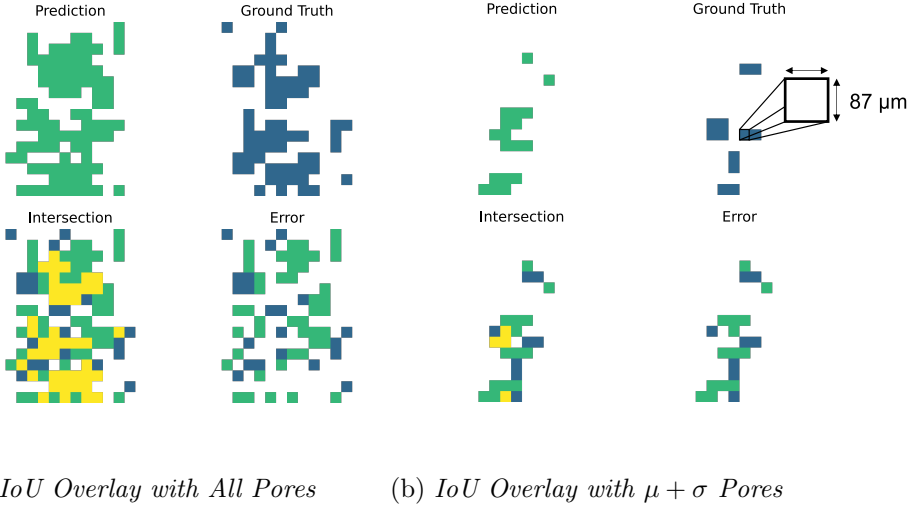
Table 2.1: R² and RMSE prediction performance metrics of pore counts for the pore quantification task utilizing CNN models trained on various datasets and build layer depths for 500 epochs.

2.4.2 Porosity Localization

During the training process, rotation transforms of the entire video sequence were introduced as data augmentation methods and compared against models trained without any rotational transformations. In addition to data augmentations, the datasets were adjusted to allow for training on *All Pores* and on pores with ESD 1 standard deviation above the mean ($\mu + \sigma$ *Pores*) in an effort to investigate the model’s performance on identifying the larger pores within the dataset.

The position of the pores within the build layer was predicting using a sequence of thermal images with the ViViT Dense model trained on either the *Spacing*, *Velocity*, and *All* dataset. The effect of data augmentation and applying a threshold for minimum ESD for pores were investigated with the training of this model as well. The Intersection over Union (IoU) also known as the Jaccard Index was used to quantify the performance of each model’s prediction. The intersection over union quantifies the prediction area overlap onto the target with the highest metric of 1.0 occurring from an exact overlap of the two sets. For the IoU calculation each set only includes the areas of porosity and in the case where both the target and prediction exhibited no porosity, a score of 1.0 was given as the prediction provided an exact match of the ground truth.

The effect of training on the various *Spacing*, *Velocity*, and *All* datasets



(a) *IoU Overlay with All Pores* (b) *IoU Overlay with $\mu + \sigma$ Pores*

Figure 2.8: Comparison of prediction and label values for the model trained on the *All* samples dataset alongside the application of a minimum ESD pore threshold (Fig. 2.8b). The examples correspond to build layer number 16 of the *Velocity* sample and the areas colored in yellow represent the intersection that is considered for IoU calculations (ignoring the background). The ViViT model trained on pores without thresholding (Fig. 2.8a) achieved an IoU score of 0.672 whereas the model trained with $\mu + \sigma$ thresholded pores (Fig. 2.8b) produced a lower IoU score of 0.323.

were investigated for this task as well the impact of rotational transforms on the input sequence. In addition, the prediction performance of the model upon applying a threshold to hide pores smaller than 1 standard deviation above the mean was applied. The prediction results of these models measured for each input label pair within the test dataset with the overall average and maximum IoU scores recorded on Table 2.2. Within the datasets that included *All Pores*, models trained on the *Spacing* datasets performed the best on average IoU scores when trained without rotational transforms. A maximum IoU score of 0.85 was achieved within the model trained on the dataset for *All* samples with rotational transforms applied. Without the applied threshold for minimum pore ESD, the model trained on the *Velocity* produces the lowest IoU score of the three models (Fig. 2.10). One explanation for the higher IoU trend

seen in the *Spacing* dataset compared to that of the *Velocity* dataset is that the *Spacing* sample has a higher degree of porosity compared to that of the *Velocity* sample. This can be attributed to lack of fusion pores within the *Spacing* dataset which are often larger than that of the keyhole pores in the *Velocity* dataset. When viewing the IoU trends in Figure 2.10, this is reflected where the lower layers of the sample achieve higher IoU scores than that of the upper layers of the sample.

However, after a minimum pore ESD threshold is applied, the *Velocity* dataset model performs on par to that of the model trained with the *Spacing* dataset (Fig. 2.11). In all of the cases there was a greater trend in overlap within the lower layers of the sample (Fig. 2.8a) likely due to the higher porosity resulting from the non-nominal process conditions used within those sample steps. With a minimum pore threshold of 1 standard deviation above the mean pore equivalent diameter ($\mu + \sigma$ Pores), all models were able to achieve maximum IoU scores of 1 (Fig. 2.11). These results were achieved towards the top of each sample where nominal process conditions were used and correctly predicted the ground truth of no pores above the threshold were present. (Fig. 2.8b) In some cases, areas with higher levels of porosity produced lower IoU scores after thresholding as the previously larger regions associated with porosity are reduced in size (Fig. 2.8). Overall, the mean IoU increased for all models after the application of a minimum pore ESD threshold. The greatest of these increases is seen in the models trained with the *All* dataset of which scored the highest average IoU of any other models. Rotational transforms did not prove to have a significant impact on improving training as the resulting metrics were often within a percent error from each other.

2.4.3 Model Limitations

The primary limitations of this work include the restricted process parameter range in the datasets, which may hinder the model's ability to generalize to combinations outside this range. While the dataset utilized in this study primarily contains lack of fusion porosity, pore characteristics such as size,

Dataset	Data Augmentation	<i>All Pores</i>		$\mu + \sigma$ <i>Pores</i>	
		Average IoU	Max IoU	Average IoU	Max IoU
<i>Spacing</i>	Rotational	0.25	0.75	0.29	1.0
	None	0.28	0.77	0.28	1.0
<i>Velocity</i>	Rotational	0.16	0.42	0.24	1.0
	None	0.17	0.44	0.29	1.0
<i>All</i>	Rotational	0.22	0.85	0.32	1.0
	None	0.21	0.72	0.32	1.0

Table 2.2: Pore localization prediction performance metrics for ViViT Dense model trained on *Spacing*, *Velocity*, and *All* sample datasets for 1000 epochs on both all segmented pores and pores with equivalent diameters greater than 1 standard deviation above the mean. The adjusted threshold to consider only pores with larger equivalent diameters improved prediction results in build layers with nominal process parameter and low resulting porosity.

shape, and defect origin from either keyholing, lack of fusion, or spatter can be explored in future work. Additionally, the models are limited to raster patterns that travel parallel to the x or y axis of the build plate. The models also require the entire sequence of thermal images associated with layer porosity to be used as input for accurate layer-wise predictions. Lastly, the hardware requirements present a challenge, as the input sequence of images demands a significant portion of the memory (over 40 gigabytes) available on the Nvidia A6000 GPUs used for training.

2.5 Conclusion and Future Work

In this work we investigate the application of machine learning to *in-situ* thermal image process monitoring for the prediction of pore count and pore localization. For this we utilized a CNN architecture and a modified ViViT model with dense prediction heads for various dataset such as *Spacing*, *Velocity*, and *All*. For the task of pore quantification, we have found that the *Spacing* dataset provides the greatest amount of signal within and models trained on the *Velocity* dataset produces the least amount of error. The pore localization task displayed a similar trend with models trained on the *Spacing* dataset achieving the best overlap when evaluating *All Pores*. The model

trained on the *All* dataset showed better performance when evaluating on $\mu + \sigma$ *Pores*.

In both tasks, the effect of rotational transforms were minimal resulting in a negligible difference in prediction outcomes. Our pore localization model experienced improved performance with the application of a minimum pore ESD threshold as it achieved higher average IoU scores, especially within areas of the sample built with nominal processing parameters. These works show the potential of utilizing *in-situ* process monitoring techniques for faster *ex-situ* part certification and future work would aim to develop a more robust digital twin achieving greater defect quantification and localization precision over the entire sample. Further extension upon development of a physical replica, known as a *Product Twin*, would lead to dynamic process parameter optimization which can possibly fix and or prevent projected defects.

2.6 Appendix

2.6.1 Input Cropping and Label Downsampling

The input thermal images were cropped from the original 85 px \times 60 px shape down to a 64 px \times 64 px shape to fit the desired input shape of the network. To achieve this 8 pixels (188.8 μm) were cropped from both the top and bottom of the image and 1 pixel (23.6 μm) was removed from the left hand side of the image. To match the cropped input, the corresponding CT label was first cropped then downscaled to align with the expected 64 px \times 64 px input. The crops of 8 pixels and 1 pixel were converted to their voxel equivalents and rounded to 52 voxels and 7 voxels respectively. This reduced the CT label a size of 520 voxels \times 423 voxels down to 416 voxels \times 416 voxels (Fig. 2.9a). The resulting cropped CT was downscaled by a factor of 24 down to 18 voxels \times 18 voxels along the x and y directions and 1 voxel along the z direction. Further cropping was applied to the x and y directions by 1 voxel on each side to reduce the label down to 16 voxels \times 16 voxels \times 1 voxel (Fig. 2.9b).

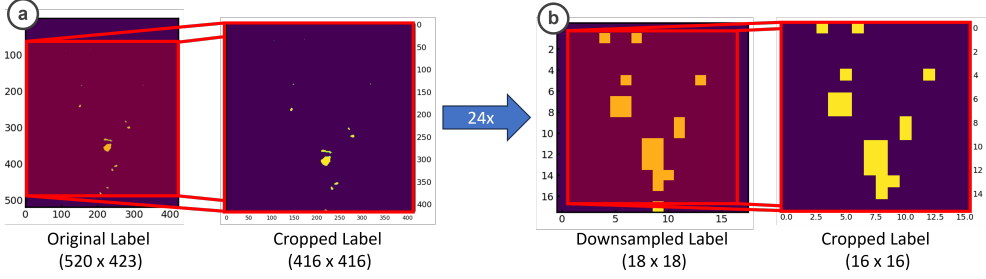


Figure 2.9: Relative porosity locations are derived from the raw CT data which are cropped to capture a consistent area to match the input thermal data (Fig. 2.9a). The CT data is further downsampled factor of 24 and cropped to provide a 16×16 label shape (Fig. 2.9b).

2.6.2 Calculating absolute temperature estimations with data obtained through Stratonics pyrometer

The estimation of absolute temperature was achieved with grey-body assumption where the emissivity remains constant at various wavelengths. Thus, with proper calibration using a NIST-traceable tungsten lamp, the pyrometer was able to read out a temperature estimation within 4% accuracy for stainless steel. [153]. This temperature is estimated with the following formula for hybrid mode temperature estimation (Eq. 2.2) where p_2 is a constant held at 14388 nm-K. Wien's approximation [111] of Planck's law is used to evaluate A_λ (Eq. 2.3) which takes into consideration emissivity and the instrument's detection factor with \bar{I}_1 representing the average intensity calculated over region Ω_p . I_1 and I_2 here represent the radiance from images over Ω_p , for $\lambda_1 = 750\text{nm}$ and $\lambda_2 = 900\text{nm}$ respectively. The temperature ratio T_R (Eq. 2.4) is calculated with R , the average of radiance from images I_1 and I_2 over Ω_p , and hardware constants for contour levels c_1 and c_2 obtained from least squares fitting over calibration data[62]. Contour level defines the region Ω_p with a β value between 0 and 1 through means of marching squares (Eq. 2.5). Our dataset utilizes images taken at $\beta = 0.7$ for its most accurate approximation of the meltpool by single contour as opposed to the multiple contours that appear at $\beta = 0.3$.

$$T_H = \frac{p_2}{\lambda_2 \ln(A_\lambda/I_2)} \quad (2.2)$$

$$A_\lambda = \bar{I}_1 e^{p_2/\lambda_1 T_R} \quad (2.3)$$

$$T_R = \frac{1}{c_1 \ln R + c_2} \quad (2.4)$$

$$c = \beta \times \max(I) \quad (2.5)$$

Sample alignment of thermal images to CT data along the X and Y axes

CT data for both samples had a shape of $1410 \times 900 \times 430$ voxels with values ranging from 0 - 255 depending on data selection type of pore, sample, or pore segmented sample. Common alignment between the *in-situ* pyrometry data and *ex-situ* CT data was established by converting the pyrometry data into voxels and applying a consistent offset. The *in-situ* pyrometry data was converted from pixels ($80 \text{ px} \times 65 \text{ px}$) to microns ($1680 \mu\text{m} \times 1365 \mu\text{m}$) to voxels ($462.81 \text{ voxels} \times 376.03 \text{ voxels}$). The CT data was then shifted to align with the pyrometry data by $-18 \text{ voxels} \times 0 \text{ voxels} \times 63 \text{ voxels}$ for the *Spacing* dataset and $-14 \text{ voxels} \times -2 \text{ voxels} \times 73 \text{ voxels}$ for the *Velocity* dataset.

2.6.3 Trends of IoU scores of ViViT Dense models trained varying pore datasets

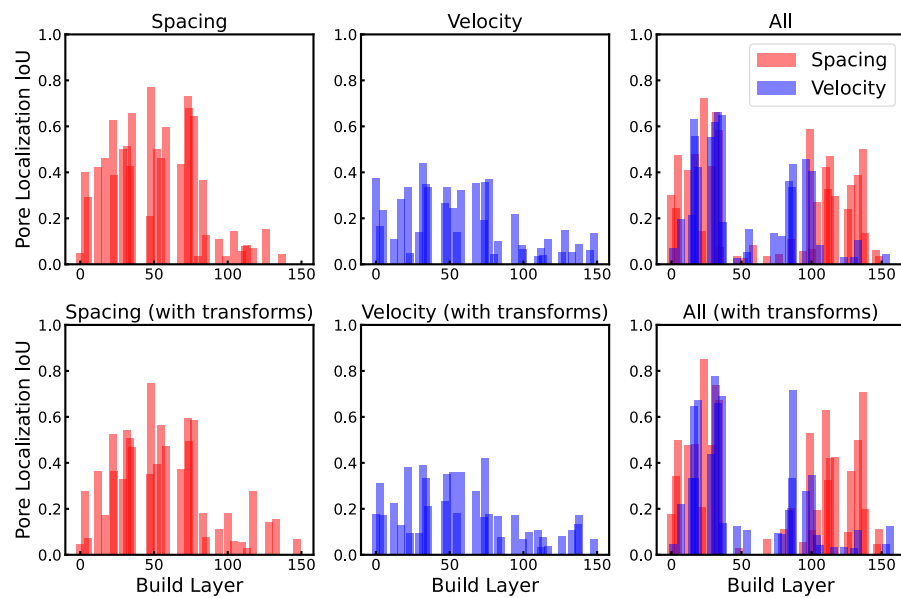


Figure 2.10: ViViT Dense model IoU trends by build layer for various datasets with and without rotational transforms without the application of a minimum pore threshold.

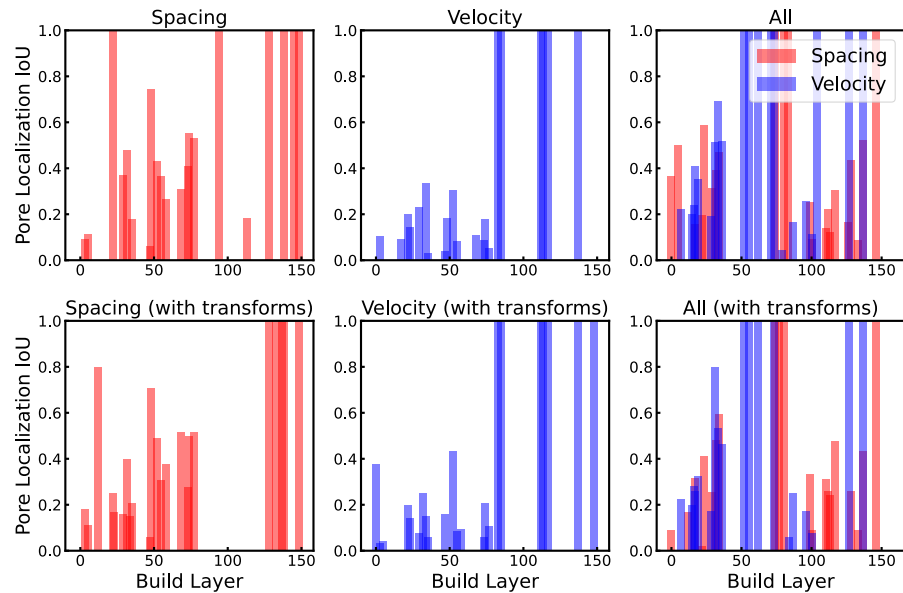


Figure 2.11: ViViT Dense model IoU trends by build layer for various datasets with and without rotational transforms with the application of minimum equivalent diameter pore threshold where equivalent sphere diameter of pores are 1 standard deviation above the mean ($\mu + \sigma$ Pores).

CHAPTER 3

ADDITIVELLM: LARGE LANGUAGE MODELS PREDICT DEFECTS IN METALS ADDITIVE MANUFACTURING

Within the process of Laser Powder Bed Fusion (L-PBF), the selection of optimal process parameters remains a key factor in the fabrication of defect free parts [40, 90]. This is achieved by avoiding the combination of process parameters that can potentially lead to melt pool characteristics resulting in either unfused powder or void initiation causing defect formation within the final part. The following defect regimes of *Keyholing*, *Balling*, and *Lack of Fusion (LoF)* describe the expected melt pool characteristics seen at a given combination of process parameters [90]. These defect regimes can be estimated by methods such as experimental observation [19], computational simulation [190], or surrogate modeling [147].

Equations 4.6 - 4.7 provide criterions dependent on melt pool dimensions and process parameters where when satisfied are expected to avoid their respective defect regimes. Melt pool conditions such as *Keyholing* do not inherently cause defects, rather it is fluctuations and collapse of the rear wall that generates voids leading to the formation of pores [108]. However due to the inaccessibility of *in-situ* cross-sectional melt pool analysis, the formation of *Keyhole* defects is often approximated with Equation 4.6, where width to depth ratios below threshold are likely to result in keyhole porosity[246]. For defects resulting from *Lack of Fusion*, the ratio of hatch spacing and melt pool width along with layer height and depth are evaluated to ascertain the potential formation of porosity [218]. The criterion for full melting across subsequent melt pools is defined as Equation 4.3 where computed values above the threshold can result in unfused powder [152, 218]. *Balling* defects occur due to the hydrodynamic capillary instabilities that occur during high scan speeds and the resulting grooves along the sides of the melt pool result in formation of voids if not remelted [94]. An approximation for the occurrence

of this phenomenon is calculated by comparing the length and width of the melt pool (Eq. 4.7). A ratio above π can indicate the presence of balling, though this value can range depending on the material [246].

$$\frac{Width}{Depth} > 1.5 \quad (3.1)$$

$$\left(\frac{Hatch\ Spacing}{Width}\right)^2 + \left(\frac{Layer\ Height}{Depth}\right)^2 \leq 1 \quad (3.2)$$

$$\frac{Length}{Width} < \pi \quad (3.3)$$

The selection of optimal process parameters often requires extensive domain knowledge of the various domains within the L-PBF process, ranging from material properties to experimental trials. Large Language Models (LLM) present a suitable solution for encapsulating these domains and have demonstrated significant success in reasoning and generating precise responses based on a given prompt [46, 65, 138, 151, 224, 225]. LLMs are able to understand textual descriptions of experimental results and respective context which enables its application as a more human accessible research tool in a wide domain of fields ranging from chemical engineering to robotics [29, 50, 52, 75, 113, 140, 161, 162, 163, 202?]. Implementations such as LLAMA[93, 224, 225], GPT[46], T5[182] and BERT[65] provide a foundation for general purpose use where it can then be fine-tuned for a specific downstream application.

The Bidirectional Encoder Representations from Transformers (BERT)[65] model is one way to architect a LLM and has garnered much attention creating the base for extensions such as RoBERTa (**R**obustly **o**ptimized **B**ERT Approach)[138], ALBERT (**A** Lite **B**ERT)[133], and DistilBERT[194]. These models which improves upon the existing implementation by either employing specific training strategies such as a dataset, batch sizes, sequence lengths, and hyperparameter optimization[133, 138, 194]. The BERT model differs from the classical masked language model in that it randomly masks its input tokens in order to predict the original vocabulary based solely through context[65]. The bidirectional approach for representing inputs that BERT

takes allows for the model to consider a more complete context window of a given sequence, providing tokens on both sides of an applied mask [65]. This is contrast to the unidirectional approach that models such as GPT take in order to more align closer to the sequential nature of text generation [181].

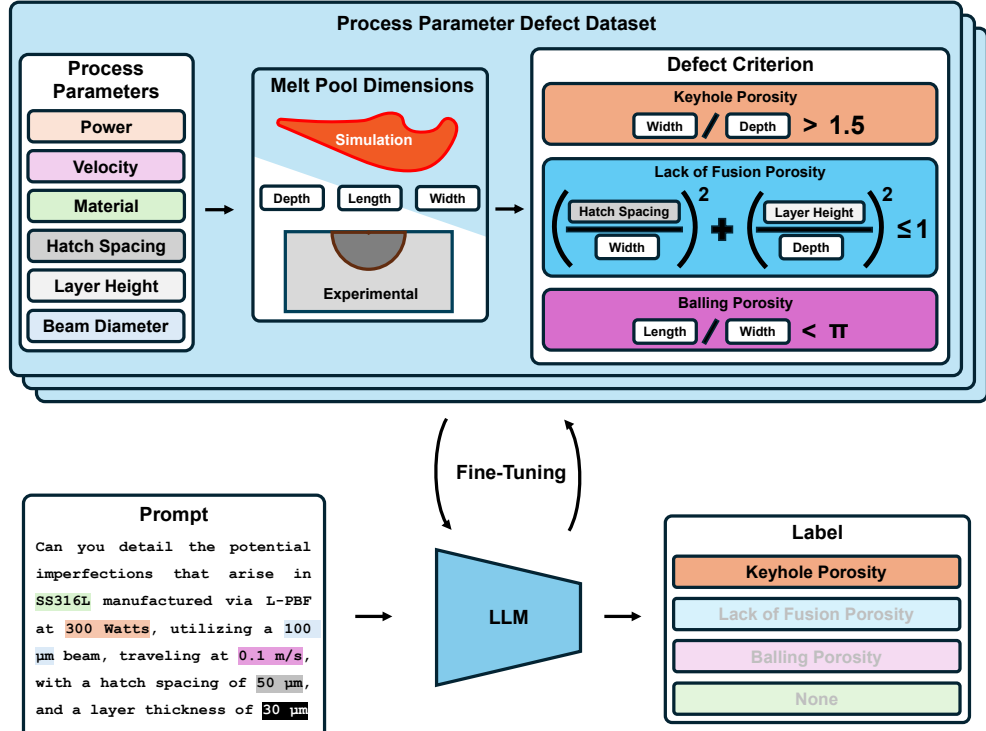


Figure 3.1: A series of LLM models are fine-tuned with a process parameter defect dataset generated from experimental results obtained from literature and simulations performed with FLOW-3D. The corresponding melt pool dimensions are used in the computation of defect criterions used as classifications labels for a specific process parameter combination. A prompt which incorporates the process parameters is provided as input to the model which in turn predicts the potential defect classification.

In this work we propose AdditiveLLM, a comparison of large language models fine-tuned on experimental and simulation based L-PBF melt pool data that able to predict potential defects given a combination of process parameters (Figure 4.1). We focus upon fine-tuning several models including:

DistilBERT[194], SciBERT[38], LLama 3.2[14], and T5[13]. Our selection of models utilize the smaller parameter set variants as this best suits our need for an efficient and lightweight model for specific inferences regarding defect regimes in L-PBF Additive Manufacturing. This approach infers upon the corpus of L-PBF melt pool data formatted as a set of process parameters inputs and defect classification labels. The model predictions provide a classification to a combination of potential defect regimes of *Keyholing*, *Lack of Fusion*, *Balling*, and *None* (for the case where no defects exist). Through inference the models are able to quickly provide insight on potential defects given a specific parameter combination without the need to perform additional simulations or experimental builds.

3.1 Methodology

3.1.1 Task

Given an input text sequence outlining a L-PBF build process with descriptions of process parameters such as material, power, and velocity; Additiv-ELLM aims to predict the most appropriate combination of defect classifications that is likely to occur. The defect classifications of *Keyholing*, *Lack of Fusion*, *Balling*, and *None* are one-hot encoded and provide a set of labels for the multi-label classification task. The *Baseline* (Figure 3.2) and *Prompt* (Figure 3.3) datasets provide structure to the input in the form of order dependent process parameters delineated with [SEP] separation tokens or queries regarding process parameters in the format of natural language respectively. The *Prompt* dataset aims to capture the behavior of the unstructured input expected from a user while the *Baseline* dataset aims to definitively capture each process parameter. These distinct approaches allow for a more flexible use case for the models as the user is able to specifically tune inputs specific to their use case.



Figure 3.2: The highlighted attributes are replaced with the appropriate values and corresponding units, unknown values are replaced with an empty string.

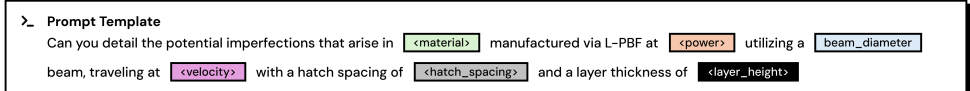


Figure 3.3: The text of each input label pair is formatted to a set of prompt templates, taking in consideration the multiple ways an input query can be structured.

3.1.2 Dataset

The dataset is compiled from literature and simulation values that provide either melt pool dimensional measurements or corresponding defect classifications from a set of process parameters. These process parameters include **material**, **power**, **velocity**, **beam_diameter**, **hatch_spacing**, and **layer_height** and their corresponding units. The majority of the data only consists melt pool dimensional measurements and these data points are processed into defect classifications using estimations for *Keyholing* (Eq. 4.6), *Lack of Fusion*(Eq. 4.3), and *Balling* (Eq. 4.7).

A number of sources were used for our dataset which include literature and simulation data points curated by *Akbari et al.* in *MeltpoolNet*[20] and our own simulations obtained using FLOW-3D[2]. (Figure 3.4) This amounts to a total of 2,779 collected data points spanning over 20 different materials, primarily consisting of Ti-6Al-4V and Stainless Steel 316L (Figure 3.5a). With these sources, the dataset is comprised of over 20 different materials varying with powers and velocity values ranging from 25 W to 5000 W and 1 mm/s to 2000 mm/s respectively.

Upon analyzing the source dataset, the distribution of materials weighs heavily towards Stainless Steel 316L and Ti-6Al-4V with the remaining materials accounting for around less than 40% of the data. *Augmented* samples are obtained by utilizing the original melt pool dimensions and applying a range of

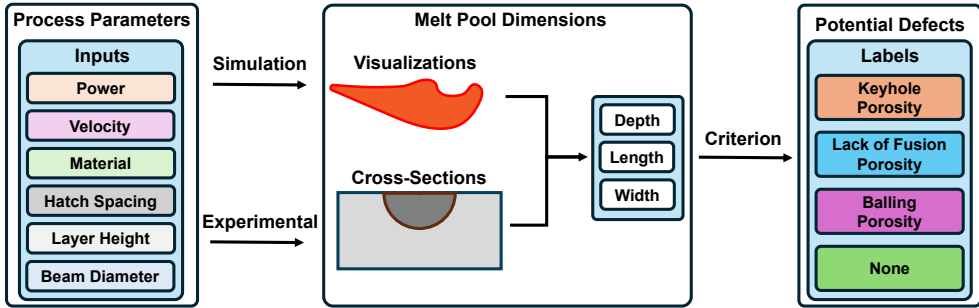


Figure 3.4: Melt pool dimensions dependent on the corresponding process parameters are obtained through either experimental cross-sectional measurements or computational fluid dynamic simulations. The obtained depth, length, and width, dimensions, pass through a set of criterions that determine the potential defects that would arise from the combination of process parameters.

different hatch spacings or layer heights to generate more *Lack of Fusion* classifications. Interestingly, when the two most common materials between the *Source* and *Augmented* dataset, SS316L appears more frequently than Ti-6Al-4V within the *Augmented* dataset (Figure 3.5b) whereas Ti-6Al-4V appears most frequently within the *Source* dataset (Figure 3.5a). An explanation for this can be found in the criterion needed for further augmenting a data sample where both the melt pool depth and width is needed to extrapolate further *Lack of Fusion* criterions over a set of additional hatch spacings and layer heights. With this a number of the Ti-6Al-4V samples within *Source* dataset are missing one of either these melt pool dimensions and are not utilized in further data augmentation. With data augmentation, the size of the dataset multiplies by a factor of around 260 increasing from 2,779 samples to 724,764 samples.

The models were fine-tuned using this data using one hot encoded labels to denote classifications of *Keyhole*, *Lack of Fusion*, *Balling*, and *None*. The most common label within both datasets is the *None* classification which is assigned if neither *Keyhole*, *Lack of Fusion*, or *Balling* is found within the sample. Following this, *Keyhole* is the second most common classification seen within the *Source* dataset and *Lack of Fusion* within the *Augmented* dataset. Within

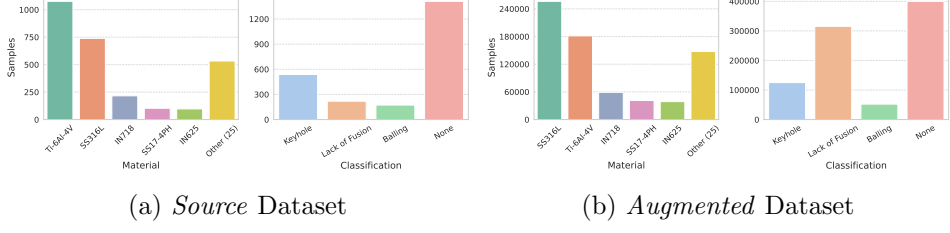


Figure 3.5: Distribution of materials and defect classifications within the dataset comprised of samples from original sources and augmented samples where additional *Lack of Fusion* classifications were obtained.

Source dataset the labels are skewed towards the *None* classification (Figure 3.5a), however with further data augmentation the number of *Lack of Fusion* classifications increases leaving only *Keyhole* and *Balling* underrepresented (Figure 3.5b). Due to their criterions (Equations 4.6 and 4.7) solely reliant on intrinsic melt pool dimensions, acquiring more data points for *Keyhole* and *Balling* classifications requires additional cost to achieve a more uniform label distribution.

The label is formatted to be compatible with a multi-label classification task since these defect regimes are not mutually exclusive to one another. An example of two valid labels would be in the case of a melt pool in key-hole mode creating pores while still producing lack of fusion defects due to excessive layer height. The text input for the dataset is formatted in two separate approaches, the first being *Baseline* (Figure 3.2) structure relying on the bare minimum amount of data and the second as the *Prompt* (Figure 3.3) arrangement resembling inputs more akin to natural language.

Data Generation and Split

The dataset consists of simulation and experimental data derived from sources such as *MeltpoolNet*[20] (`meltpoolclassification.csv`, `meltpoolgeometry.csv`) and a number of our own FLOW-3D[2] simulations (`dimensions_ti64.pkl` and `dimensions_ss316l_10_micron.csv`). The `meltpoolclassification.csv` provides the direct defect classification of a combination of process parameters, however in cases where only the melt pool dimensions are provided, the

defect classifications are obtained using their respective criterions. This data was further augmented by analyzing the *Lack of Fusion* defect criterion on 20 different layer heights and hatch spacings ranging from $0 \mu\text{m}$ to $950 \mu\text{m}$ with the assumption that the melt pool’s width and depth remain the same. Each of these individual files, all of the entries are shuffled and split to 75%, 15%, and 10% for the train, test, and validation datasets respectively. This allows for an equal distribution of samples within each source in the overall dataset splits used to fine-tune the LLM.

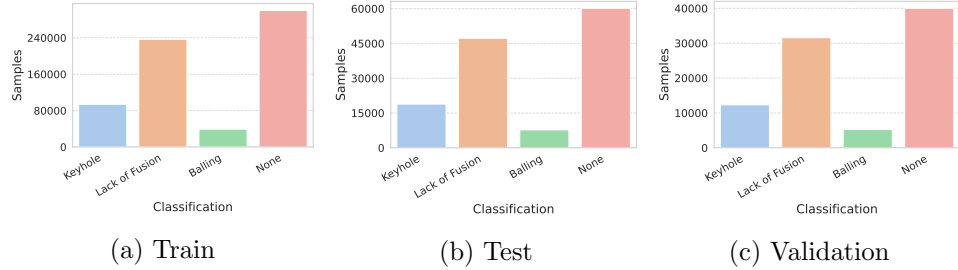


Figure 3.6: Distribution of materials and defect classifications within the train, test, and validation splits are derived from the *Augmented Dataset*.

Baseline Dataset

The *Baseline* configuration of our dataset seeks to provide the minimum input data necessary to fine-tune each model. This is done by utilizing the `[SEP]` token to indicate the distinction between ordered process parameters of `material`, `power`, `velocity`, `beam_diameter`, `hatch_spacing`, and `layer_height` (Figure 3.2). The streamlined `text` input of just the process parameters aims to provide the model only the essential parameters to generate a prediction. This amounted to a total of 724,764 distinct input-label pair combinations with the 75%, 15%, 10% train, test, validation split including 543,573, 108,715, and 72,476 respectively.

Prompt Dataset

The *Prompt* dataset consists of the same process parameter inputs but structured in a way that more closely resembles natural language. This was

achieved through the use of ChatGPT to generate 100 unique prompt templates querying for the potential defect associated with a combination of process parameters. The template provides the same fields as the *Baseline* configuration to generate a set of text inputs for each set of process parameter combinations within the data (Figure 3.3). With the 75%, 15%, and 10% respectively set to the train, test, and validation split, the 100 unique prompt templates are also split accordingly such that there are either 75, 15, or 10 unique prompts generated from each set of process parameters depending on the split of the dataset. This increases the input-label pair of the dataset by 100x to over 70 million distinct pairs over all train, test, and validation splits.

3.1.3 Large Language Models

DistilBERT

DistilBERT is a distilled implementation of the BERT model for the purposes of fine tuning developed by researchers at HuggingFace[194]. DistilBERT achieves a 40% reduction in model size (66 million parameters) compared to the original BERT (110 million parameters) model while retaining 97% of the language understanding capability and gaining a 60% increase in training speed[194]. This model is a suitable candidate for obtaining preliminary insights and evaluating the feasibility of implementing a BERT-based inference approach for process parameter dependent defects. The training process for the classification head a batch-size of 512 and a learning rate of 2E-5.

SciBERT

SciBERT is a specialized implementation of the 110 million parameter BERT model[65] pretrained on large-scale scientific data including numerous publications from computer science to biomedical research [38]. With a dataset of over 1.14 million papers, the authors are able to pretrain the BERT implementation on a corpus of text with the use of domain specific vocabulary allowing better representation of scientific terms and symbols through their SciVocab vocabulary library [38]. When evaluated on Natural Language Processing

(NLP) tasks regarding Named Entity Recognition (NER), PICO Extraction (PICO), and Relation Classification (REL); SciBERT surpasses State Of The Art (SOTA) performance, establishing its proficiency in comprehending and executing scientific tasks [38]. For this reason, we believe that defect classification would be a suitable task for a finetuned implementation of SciBERT with our *Baseline* and *Prompt* datasets. This model’s classification head was fine-tuned with a batch size of 256 and a learning rate of 2E-5.

Llama 3

Llama 3 is the latest iteration of LLMs developed by the AI team at Meta[93]. In comparison to the previous implementations, Llama 3 is trained on a much larger dataset of 15 trillion tokens, boasts a larger context window of up to 128K tokens, and consists of 405 billion parameters for its largest model [93, 224, 225]. For our implementations we utilize Llama-3.2-1B, a 1 billion parameter implementation of the the Llama 3 model that incorporates the logits of the 8 billion and 70 billion parameter Llama 3.1 models during pre-training in order to retain a majority of their performance while reducing the hardware requirements for finetuning[14]. This model was fine-tuned with a batch size of 512 and a learning rate of 2E-5.

T5

Text to Text Transfer Transformer (T5) is an encoder-decoder large language model developed by Google specializing in simple text to text tasks such as translation, summarization, and sentiment analysis [182]. Variations of this model extend up to 11 billion parameters and for our experiment we utilize T5-Small[13] consisting of 60 million parameters for its efficient training speed and performance on a specialized task such as defect classification [13, 182]. This model was fine-tuned with a batch size of 512 and a learning rate of 1E-4 following the guidelines outlined in the documentation [11].

3.1.4 Fine-Tuning

Each of the LLM models were attached with a classification head consisting of a simple Multi-Layer Perceptron (MLP) layer producing four distinct binary classifications and fine-tuned using the *Baseline* and the *Prompt* dataset. In each case the weights of the LLM model remain unfrozen and were trained along with the classification head for up to 25 epochs for *Baseline* fine-tuning and 2 epochs for *Prompt* fine-tuning. Models fine-tuned on the *Prompt* dataset were done so for a shorter number of epochs due to the lengthy training duration resulting from the dataset being 100x larger than that of the *Baseline*. Binary cross entropy was used as the loss function for this multi-label classification task and the inputs were tokenized with each LLM’s respective tokenizer used in pretraining.

The models were fine-tuned on various machines with GPU resources of Nvidia RTX A6000 with 48 GiB of memory and Nvidia RTX 2080Ti with 11 GiB of memory dependent on which where available. The Llama-3.2-1B model could only be fine-tuned with Nvidia RTX A6000 due to its large overhead of 1 billion parameters and also took the most around of time to train. A comprehensive table of the model, equipment, epochs, and runtime of all models is listed in Table 3.3.

3.2 Results and Discussion

3.2.1 Model Results

Table 3.1: Accuracy and F1 metrics obtained from validation set inference on models fine-tuned with *Baseline* dataset for 25 epochs and *Prompt* dataset 2 epochs.

LLM	<i>Baseline</i> Fine-Tuned		<i>Prompt</i> Fine-Tuned	
	Accuracy	F1 Score	Accuracy	F1 Score
DistilBERT	88.41%	0.7959	82.22%	0.7140
SciBERT	90.88%	0.8480	81.40%	0.6801
T5	71.414%	0.5548	79.65%	0.6536
Llama	94.23%	0.9059	64.32%	0.6138

Baseline Fine-Tuned LLMs

Initially each of the LLM models were fine-tuned for 5 epochs on the *Baseline* dataset and further extended to 25 epochs with 5 epoch increments (Table 3.2) which resulted in all models apart from T5 showing significant improvement in evaluation accuracy. To put our baseline results into context with other shallow machine learning implementations we reference the findings by *Akbari et al.*[20] where the authors achieve a 85.78% classification accuracy using the Random Forest model with *MeltpoolNet* data which we derive a significant portion of our dataset from. The distribution of predictions of the fine-tuned LLMs can be found in the Figure 3.11 within the Appendix.

Improvement in evaluation accuracy with epochs is most prominently displayed in the Llama model where the extended training cycles drastically improved the model’s prediction accuracy, achieving an accuracy of 94.23%, the highest accuracy of all the trained models (Table 3.1). The model achieves an F1 score of 0.9059 indicating a small amount of its achieved accuracy is in part due to the composition of the dataset (Figure 3.7 bottom left). Llama’s higher accuracy is expected as its parameter size is over 9x greater (1 billion) to the BERT models which it is compared against (110 million) while taking also significantly more time to train as well. Notably, other models displayed plateauing or decreasing validation accuracy after 20 epochs indicating that further fine-tuning may not present additional benefit.

LLM	5 Epochs	10 Epochs	15 Epochs	20 Epochs	25 Epochs
DistilBERT	84.22%	87.75%	87.75%	88.29%	88.41%
SciBERT	88.29%	88.93%	88.99%	91.32%	90.88%
T5	79.61%	71.45%	76.42%	77.92%	71.41%
Llama	89.18%	91.66%	92.94%	93.01%	94.23%

Table 3.2: Accuracy for models trained on *Baseline* dataset over a series of 25 epochs with 5 epoch increments.

Of the four models trained with the *Baseline* dataset, the T5 model displayed the least potential as its accuracy stagnant throughout all training epochs whereas all other models exhibited an improvement in evaluation accuracy. One reason for this could be attributed to the use of the T5-Small

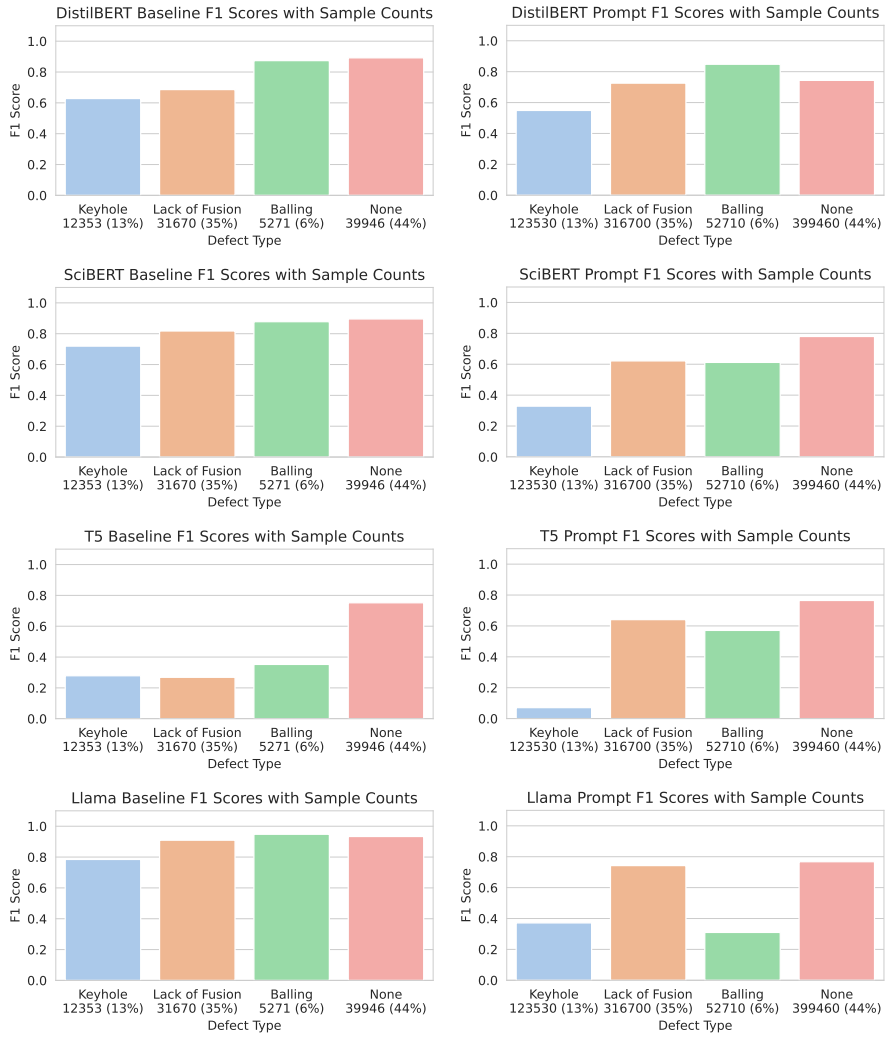


Figure 3.7: F1 Scores for each of the defect types with their corresponding total samples below each class label within either *Baseline* (left) or *Prompt* (right) dataset fine-tuned models. Within evaluation set the 44.76% are classified as *None*, 13.84% as *Keyhole*, 35.48% as *Lack of Fusion*, and 5.90% as *Balling*. Notably F1 scores for the highest performing *Baseline* Llama and *Prompt* DistilBERT fine-tuned models display relatively consistently values throughout all classifications.

model which only consisted of 60 million parameters, the least of all compared models [182]. Its lightweight architecture and smaller dimensionality of 512 contribute to its lack of accuracy improvement after lengthening the number of training epochs [182].

Evaluating the performance of the *Prompt* dataset on LLMs fine tuned on the *Baseline* dataset, all exhibit poor performance. The initial expectation was that the large language models would be able to reason through input prompts and inherently map parameter values to those seen within the *Baseline* dataset. However with the high amount of defect misclassifications, the models seem to be highly dependent on the syntactical structure of process parameter inputs (Figure 3.2) of the *Baseline* dataset. Potentially adjusting the *Baseline* dataset to further include relevant details such as the names of each process parameter inside the input could help inform the model to the context of each value.

***Prompt* Fine-Tuned LLMs**

With the *Prompt* dataset each of the LLMs were fine-tuned for only 2 epochs as the size of the dataset is 100x larger than that of the *Baseline* dataset with the use of 100 different prompt templates. Within the *Prompt* fine-tuned LLMs, the DistilBERT model achieves the highest accuracy (82.22%) with an F1 Score of 0.7140 (Figure 3.7 top right). SciBERT achieves similar performance with T5 and Llama models performing significantly worse.

The poor performance achieved by Llama is surprising as it achieved the highest accuracy and F1 score when evaluated on the *Baseline* dataset, yet performs significantly worse on the *Prompt* dataset. Within the distribution of prediction classifications obtained by fine-tuning with the *Prompt* dataset (Figure 3.12), the Llama model shows a more uniform distribution of predictions in comparison to that of SciBERT or DistilBERT.

Impact of Dataset Composition

We also briefly investigated the effect that dataset composition has on the accuracy and F1 score. For this we look into the more frequent material

of SS316L which amounts to around 35% of our validation dataset and the uncommon IN615 material which consists of around 5% of our total validation set. Looking into the inference results for just these materials on our best performing *Baseline* and *Prompt* fine-tuned models we can gauge the impact that dataset composition has on each of these models.

With the DistilBERT model fine-tuned on the *Prompt* dataset we observe an overall accuracy of 80.76% and an overall F1 score of 0.6867 only on the SS316L samples. With the IN615 samples we observe a higher accuracy of 88.31% and an overall F1 score of 0.8461 (Figure 3.8 top row). The Llama model fine-tuned on the *Baseline* dataset displays a more consistent distribution of scores as with just the SS316L sample it achieves an overall accuracy of 95.84% and a overall F1 score of 0.9308 with the IN615 samples achieving a similar overall accuracy of 0.9459 and overall F1 score of 0.9276 (Figure 3.8 bottom row).

These results show that the Llama model fine-tuned on the *Baseline* dataset is able to extrapolate the defect types well even in the case of class imbalance. However, for the DistilBERT model fine-tuned on the *Prompt* dataset, the limited dataset has more of an impact on the prediction performance of both cases.

3.2.2 *Baseline* vs. *Prompt* Fine-Tuned LLMs

Upon comparing the results obtained from the LLM models fine-tuned on the *Prompt* and *Baseline* datasets (Table 3.1), it is clear that the models fine-tuned on the *Baseline* perform better in all cases with the exception of the T5 model which achieved higher accuracy when trained on the *Prompt* dataset. Between datasets, the two primarily differ in the formatting of process parameters as inputs for fine-tuning each model with the *Baseline* dataset using a template with sparse input parameters along with their corresponding units (Figure 3.2). The *Prompt* template consists of more complex formatting of the dataset where the material parameters are embedded within a natural language input provided to the LLM model (Figure 3.3).

Within these two approaches, the *Prompt* datasets presents higher com-

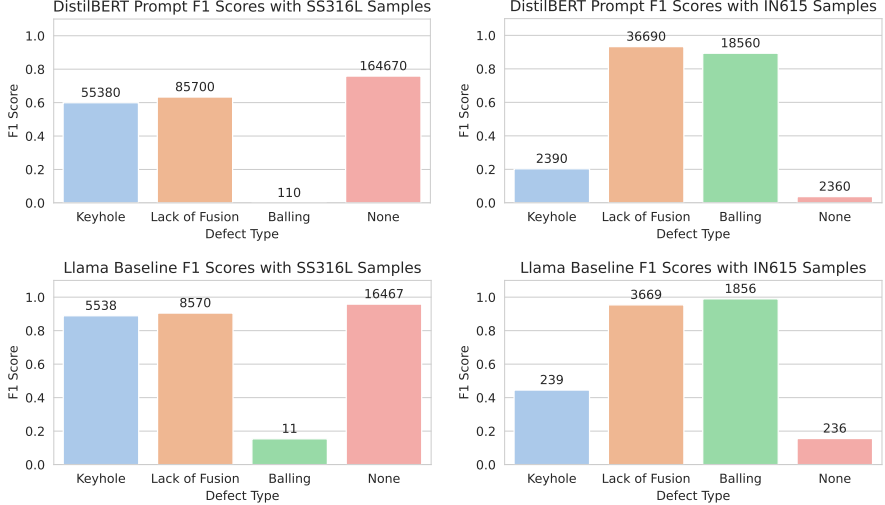


Figure 3.8: Distribution of F1 scores within each corresponding class for DistilBERT *Prompt* and Llama *Baseline* fine-tuned models on SS316L (common) and IN615 (uncommon) samples.

plexity as the parameters for material, power, beam diameters, velocity, hatch spacing, and layer height can be arranged in any number of ways to fit the flow of natural language input. In contrast, the *Baseline* dataset uses a strict template with [SEP] tokens to distinguish each parameter and maintains the same order of parameters throughout the generation of each input. With this, the varying accuracies between the two models can be attributed in part due to the different complexities within each input set where fine-tuning with structured input presents an easier task for the LLM model than that of unstructured natural language inputs of the *Prompt* dataset.

Potentially improving the representation of process parameters within each input format would likely improve each model’s ability to extrapolate upon each dataset. One avenue for this could be through better numerical representation of the input process parameters as most tokenizers do not have an innate understanding of the relationships between numbers [221]. Tokenizers such as xVal [88] and works by Thawani *et al.*[221] and Siyu Yu *et al.*[242] have demonstrated success when processing numerically dense datasets and generating predictions on out-of-distribution inputs. Thus, using a tokenizer

specialized in parsing numerical inputs would potentially help the model understand the relationship between process parameters and generate predictions with higher accuracy.

3.2.3 Principle Component Analysis

With the application of Principle Component Analysis (PCA) the model's ability to distinguish between process parameters and their corresponding defects is more clearly defined. In PCA charts for LLM models fine-tuned with the *Baseline* datasets, a clear distinction can be seen in defects for *Balling* and *Keyhole / Lack of Fusion*. Areas of *Keyhole* and *Lack of Fusion* share a greater degree of overlap due to data augmentation procedure used to obtain *Lack of Fusion* regimes. The data augmentation procedure which adjusts the *Hatch Spacing* and *Layer Thickness* of a given sample increases the number of data points we can use to fine-tune each model. The method does however increase the number of samples classified as Lack of Fusion leading to a greater portion of samples being marked as such.

The PCA chart regarding the *Prompt* dataset (Figure 3.10) exhibits a different trend where all of the different defect regimes have high degrees of overlap on top of one another. This further supports the case that the LLMs fine-tuned on the *Baseline* dataset struggle to interpret the process parameters outlined in the *Prompt* dataset, most likely due to the fact that process parameters are not formatted in its expected syntax. As such, areas of *Keyhole*, *Lack of Fusion*, *Balling*, and *None* have high degrees of overlap as the models fail to extract the significant features of each input.

3.3 Conclusion and Future Work

3.3.1 Conclusion

Analysis of fine-tuned LLM models show that the 1 billion parameter Llama 3 implementation achieves the highest accuracy of 94% on the *Baseline* dataset and DistilBERT achieves the highest comparable accuracy of 82% within the *Prompt* fine-tuned LLMs. It is worth noting that the Llama model presents a

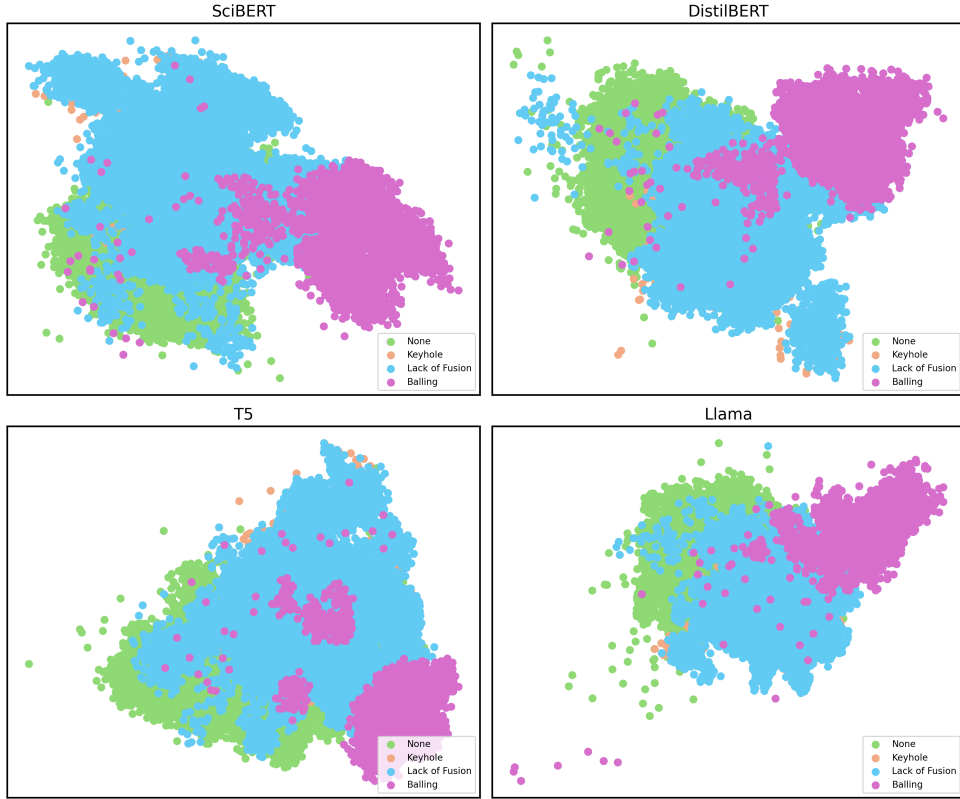


Figure 3.9: Principle Component Analysis (PCA) of LLMs fine-tuned and evaluated with the *Baseline* dataset. For all models, the labels of *Keyhole* and *Lack of Fusion* share a high degree of overlap to the extent that *Lack of Fusion* covers much of the *Keyhole* labels.

significantly longer training duration and parameter set than the other LLMs and more cohesive dataset of the various classifications can alleviate any overfitting. With this it can be seen that larger parameter sets and lengthier training runs improve the evaluation accuracy of models fine tuned on the *Baseline* dataset. The findings here show that LLMs fine-tuned on a process parameter defect dataset are able to reason and predict potential defects existing in experimental and simulation data. The incorporation of natural language allows for a more accessible inputs enabling users to determine optimal build conditions with limited domain knowledge.

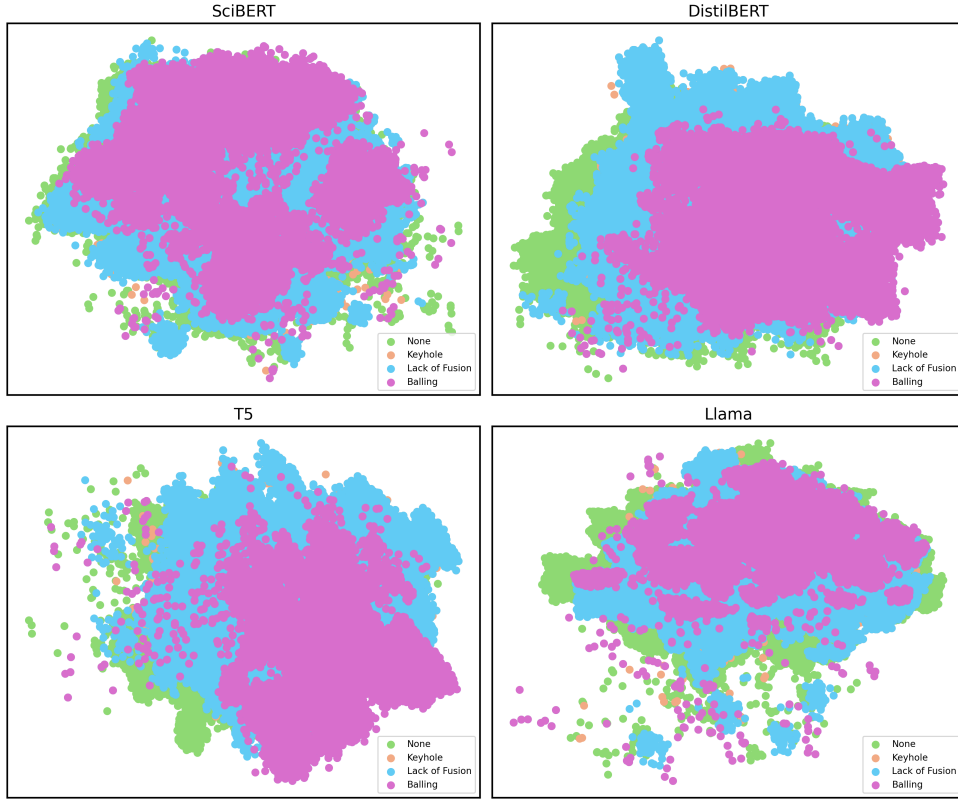


Figure 3.10: Principle Component analysis of LLM models fine-tuned on the *Baseline* dataset and inference using the *Prompt* dataset show high degrees of overlap between all labels indicating the models struggle to extract relevant information when formatted in natural language.

3.3.2 Future Work

Future work in this domain would focus upon obtaining a more diverse dataset with a wider range of materials, parameter sets, and additive processes. Longer fine-tuning of LLMs with the *Prompt* dataset could help expose the models to diverse input set of natural language and produce predictions with greater accuracy. In addition, parts of the existing models such as the tokenizer could be replaced with one better equipped in understanding numerical inputs.

3.3.3 Data Availability

The models and dataset are available within a HuggingFace collection at [ad-ditivellm.ppak.net](https://huggingface.co/ditivellm/ppak.net).

3.4 Appendix

3.4.1 Model Training Resources and Runtimes

Model	Nvidia GPU(s)	Epochs	Runtime (s)
<i>DistilBERT</i>			
Baseline	RTX 2080 Ti 11 GB	5	8886.8791
Baseline	RTX 2080 Ti 11 GB	10	17381.732
Baseline	RTX 2080 Ti 11 GB	20	34532.80
Baseline	A6000 48 GB	25	44721.41
Prompt	RTX 2080 Ti 11 GB	2	261917.09
<i>SciBERT</i>			
Baseline	RTX 2080 Ti 11 GB	5	29574.32
Baseline	RTX 2080 Ti 11 GB	10	64870.11
Baseline	RTX 2080 Ti 11 GB	15	48722.28
Baseline	A6000 48 GB	20	36199.01
Baseline	A6000 48 GB	25	45431.34
Prompt	A6000 48 GB	2	302130.9155
<i>T5</i>			
Baseline	RTX 2080 Ti 11 GB	5	6616.4776
Baseline	RTX 2080 Ti 11 GB	10	12668.9228
Baseline	RTX 2080 Ti 11 GB	15	18136.53
Baseline	RTX 2080 Ti 11 GB	20	25243.55
Baseline	RTX 2080 Ti 11 GB	25	28502.06
Prompt	A6000 48 GB	2	140927.38
<i>Llama</i>			
Baseline	A6000 48 GB	5	100295.01
Baseline	A6000 48 GB	10	203343.7214
Baseline	2 x A800 40 GB	15	187949.0901
Baseline	A800 40 GB	20	123264.0941
Baseline	A6000 48 GB	25	151826.5571
Prompt	2 x A6000 48 GB	0.5	23913.9942
Prompt	4 x Quadro 6000 24 GB	2	24081.6544

Table 3.3: Hardware configurations used for fine-tuning the various large language models along with their corresponding epochs and runtimes.

3.4.2 Model Evaluation Runtimes

Model	<i>Baseline (25 Epochs)</i>	<i>Prompt (2 Epochs)</i>
DistilBERT	1.295249 seconds	1.539689 seconds
SciBERT	4.968237 seconds	4.791886 seconds
T5	0.882309 seconds	0.180063 seconds
Llama	3.231006 seconds	3.161664 seconds

Table 3.4: Sample inference times obtained from querying fine-tuned LLMs hosted on CPU.

3.4.3 Prediction Distribution of LLM fine-tuned on *Baseline* Dataset

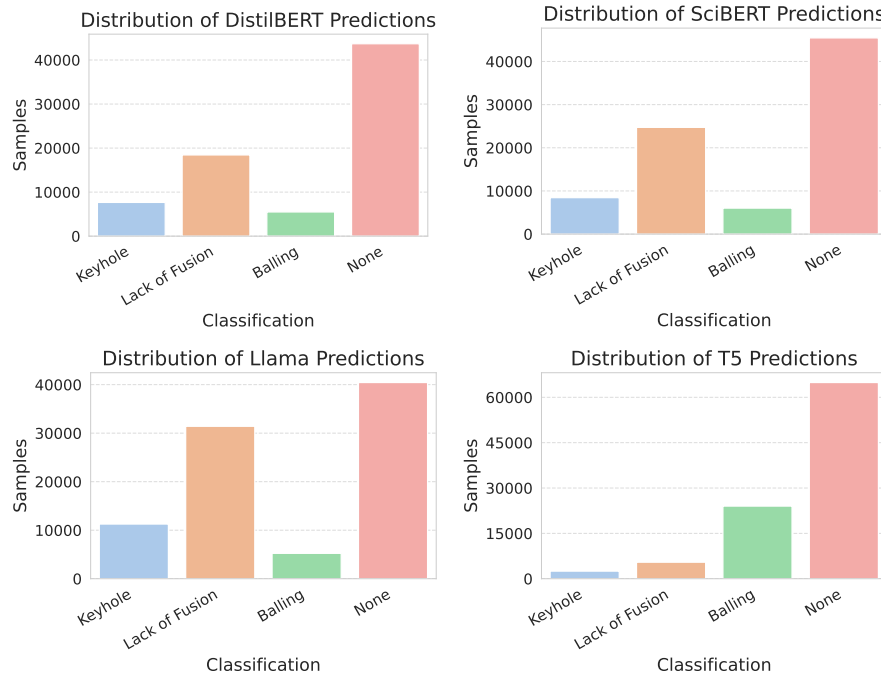


Figure 3.11: LLMs fine-tuned on *Baseline* dataset have prediction distributions similar to that of the *Augmented* dataset with the exception on the T5 model.

3.4.4 Prediction Distribution of LLM fine-tuned on *Prompt* Dataset

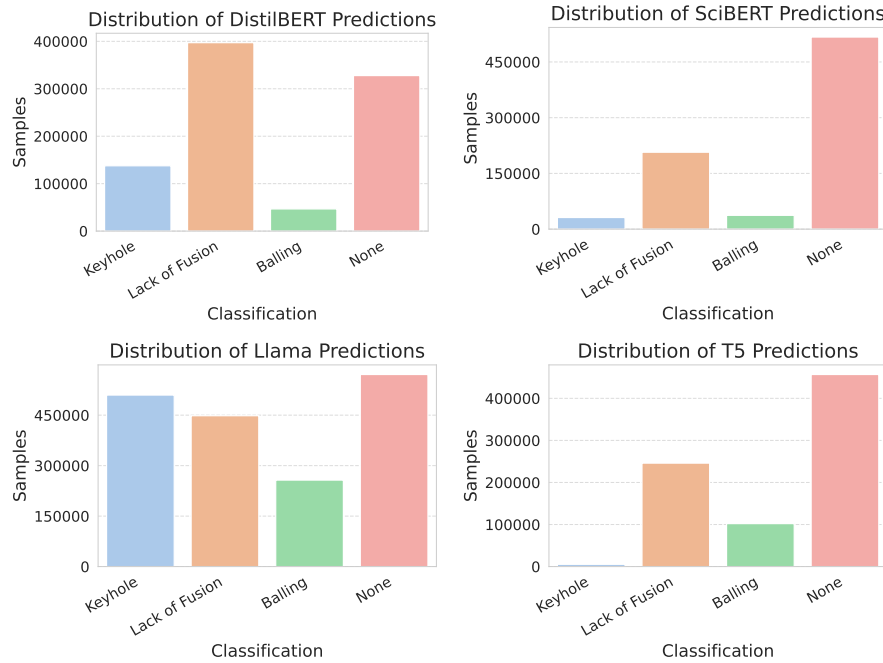


Figure 3.12: LLMs fine-tuned on *Prompt* dataset exhibit a wider range of classification distribution labels with DistilBERT and SciBERT most closely resembling that of the *Augmented* dataset.

CHAPTER 4

AGENTIC ADDITIVE MANUFACTURING ALLOY EVALUATION

4.1 Introduction

Evaluation of an alloy's suitability for fabrication and its appropriate processing parameters is a key component of the Additive Manufacturing (AM) process. In industries that focus on biomedical, aerospace, or energy challenges, their unique applications often involve the selection and evaluation of alloy candidates that are best equipped to perform in their service environment[30, 31, 84, 179, 193, 215]. In addition, considerations such as deformation[114, 175, 185], corrosion resistance[30, 238], and biocompatibility[119, 176, 177] are key motivators for composition refinement which can foster the development of novel alloys. However, the discovery and validation of new AM alloys remains a time-consuming process that often requires expertise in materials science, computational simulations, and experimental analysis[31, 179, 215]. Furthermore, each alloy presents its own set of unique challenges, often requiring specific build parameters to avoid potential defects within part fabrication[31, 72, 85, 107, 117, 142, 145, 180, 231]. The search and optimization of desirable process parameters often requires extensive simulation analysis and experimental trials to validate their suitability within build conditions[104, 185, 216, 217, 218].

For the task of obtaining material properties for a novel elemental composition, Computer Calculation of Phase Diagrams[121] (CALPHAD) is commonly performed to calculate the individual phases of an alloy via Gibbs Free Energy and numerical optimization. CALPHAD provides a rigorous thermodynamic framework for predicting equilibrium phase stability and composition in multicomponent alloys by combining assessed Gibbs energy descriptions of individual phases with numerical minimization of the total free energy. In practice, modern CALPHAD workflows go beyond phase fields, as well-curated mobility and property databases enable the prediction of temperature-

dependent thermophysical quantities such as thermal conductivity (k), specific heat capacity (C_p), and density (ρ).[49, 86]. Thermo-Calc[222] software suite is used to predict An estimation of material properties for a proposed alloy composition is predicted with this method using a library of resources to obtain relevant information regarding various elements, alloys, and application properties.

With the procurement of the material properties of a proposed alloy composition, its suitability for an AM build is assessed through numerical solvers. Solvers such as those developed by Eagar-Tsai[71] and Rosenthal[191] provide preliminary information on the temperature field of a melt pool through an analytical solution. Whereas, OpenFOAM[16] and FLOW-3D[2] utilize Computational Fluid Dynamics (CFD) to provide a more detailed analysis of the underlying fluid flow, heat transfer, and solidification phenomena of the melt pool[212, 250]. The obtained melt pool dimensions are used to calculate potential defect regimes within a process map of beam power and scanning velocity combinations[59, 60, 218]. Specifically, the lack of fusion defect region is of primary concern as insufficient melting induces the formation of large pores and in extreme cases can cause the build process to fail[218]. Insight into this defect regime is essential for the informed selection of optimal build parameters within the process window.

Recent advances in multi-agent systems have demonstrated the potential of Large Language Models (LLMs) to perform complex, goal-oriented tasks that extend beyond the constraints of a single prompt[32, 51, 53, 83, 115, 148, 161, 164]. This has been applied to the monitoring and adjustment of real-time Fuse Deposition Modeling (FDM) builds[115], search and discovery of potential catalyst and drug candidates[161, 164], and optimization of material and molecular design simulations[51, 53]. In these tasks, LLMs autonomously determine the next course of action by reasoning over the information available within the dynamic environment[53, 115, 164]. The next course of action often involves utilizing functionality external to the LLM which is made accessible through a tool call. This can be done through various methods and solution providers include LangChain[4] and LlamaIndex[5]. This work utilizes the Model Context Protocol (MCP)[23] as the library for creating and exposing

tools for the LLM that allow seamless integration into any client with an MCP interface.

With these established goals, this work aims to develop a multi-agent system for the search, proposal, and analysis of novel alloy compositions suitable for additive manufacturing. The inclusion of the LLM allows for the intelligent automation and reasoning of tool generated responses from natural language inputs which can be constructed into valid function inputs. MCP tool binding from `thermo-calc` and `additive-manufacturing` packages allow for the actions such as process map generation and material property prediction to be controlled by agents. The multi-agent system is able to reason and plan through given tasks and dynamically adjust task trajectories based on tool responses. This in turn enables the intelligent automation of routine tasks and accelerates the evaluation of novel alloy compositions within additive manufacturing.

4.2 Methodology

4.2.1 Calculation of Thermophysical Properties

For this task, given an hypothetical element composition of a specific alloy, Thermo-Calc[222] is expected to provide the relevant material properties of density, thermal conductivity, specific heat capacity, electric resistivity, and the liquidus and solidus phase transition temperatures. Thermo-Calc utilizes a CALPHAD based solver to calculate equilibrium phase diagrams and extrapolate properties along with the material property databases to assist with obtaining thermophysical properties for various alloys. The platform also includes their TC-Python SDK allowing for programmatic use of the features, providing an interface for the creation and binding of agentic tools callable via MCP.

With the Thermo-Calc’s property diagram calculation function, a composition of elements is provided to generate a property diagram to extract material properties. Compositions consist of the mass fraction of individual elements and for commonplace alloys, a map of their elemental compositions is obtained from existing literature sources [21, 72, 95, 117, 128, 142, 143, 144,

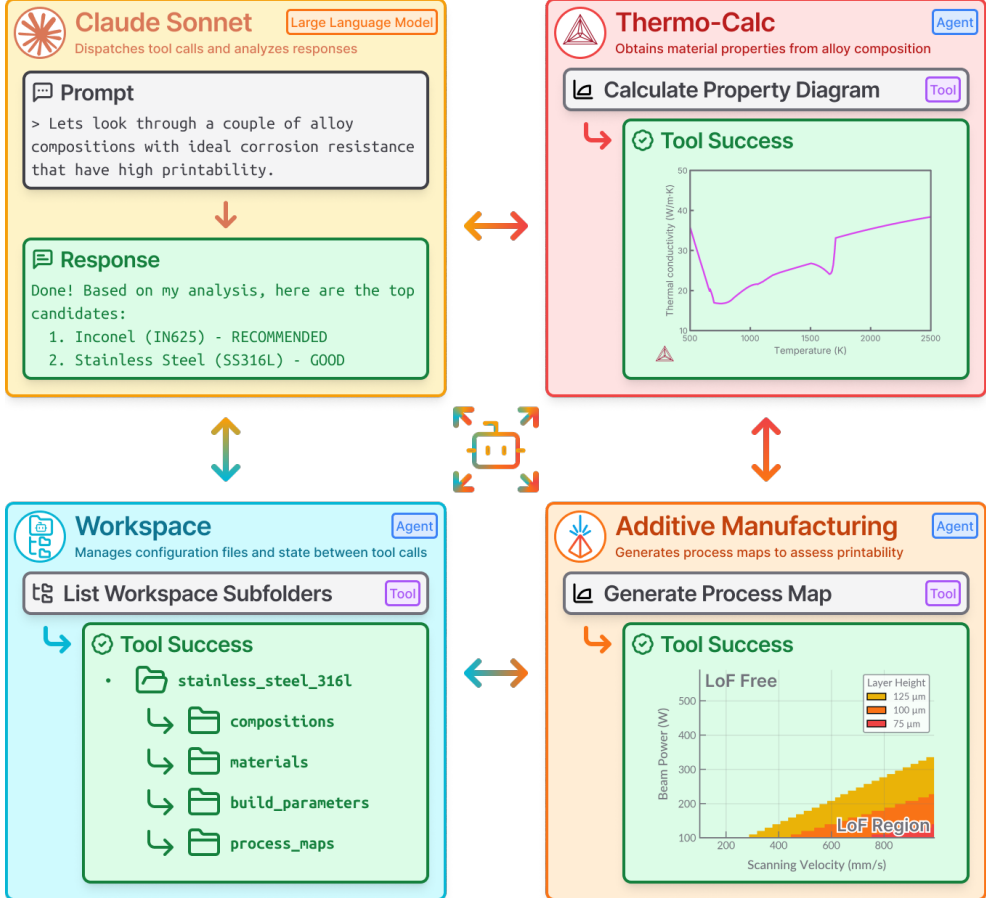


Figure 4.1: **(Top Left)** An input query for alloy compositions regarding the printability of an additively manufactured part suitable for its intended use case is provided to Claude Sonnet. This Large Language Model (LLM) calls the tools necessary to generate and analyze each potential alloy compositions, providing a response of candidates ranked by their content of their lack of fusion fusion regimes. **(Top Right)** Thermo-Calc allows for the retrieval of material properties for an hypothetical alloy composition, for instance thermal conductivity, to be used in down stream lack of fusion calculations. **(Bottom Left)** Workspaces provide a way for each of the tools to effectively communicate with one another and handles state management and file organization. **(Bottom Right)** Tools managed by the Additive Manufacturing subagents then utilize the calculated material properties from the Thermo-Calc subagent to generate a lack of fusion process map to send back to the LLM for analysis and final recommendation.

[180, 189, 197, 214, 216, 231, 239]. In this process, a suitable database (one of TCFE14, TCNI12, TCAL9, TCTI6, and TCHEA7, or PURE5 [195]) is selected to obtain the necessary phase and transport properties with the appropriate SI units. Database selection is determined through matching an alloy's primary element composition to its database counterpart. The element with the highest weight fraction is designated as the "top" element. A composition is deemed as multi-principal if at least three elements have individual weight fractions ≥ 0.15 . Then the appropriate database is selected by elimination in the order as described in Appendix C. The provided compositions and database values are then utilized in equilibrium calculations where the minimization of Gibbs Free Energy is iteratively calculated until convergence is met [8, 12].

Solidus and liquidus phase transition temperatures are extrapolated through tracking the liquid volume fraction. A one-dimensional temperature sweep is performed to find a point where the liquid fraction moves from approximately 0 to 1. The default arguments for the minimum and maximum temperature ranges are 500 K and 3500 K respectively. The obtained solidus and liquidus temperatures are utilized in subsequent tasks to obtain material properties from the proposed alloy. Density ($\rho = B/V$) and specific heat capacity are obtained through Thermo-Calc's user function using the ratio of mass (B) to volume (V) and the temperature derivative of molar enthalpy denoted as HM.T respectively. Thermal conductivity and electrical resistivity are built-in thermodynamic quantities and can be readily obtained at a given temperature. The melting temperature is taken as the average between the solid and liquidus phases.

The calculated material properties of absorptivity, thermal conductivity, liquidus and solidus phase transition temperatures, density, and specific heat capacity are saved as a common material configuration compatible with the additive-manufacturing package. These values will then be utilized with the tools there for initialization and generation of a lack of fusion process map to evaluate the printing feasibility of these material properties.

The accuracy of the material properties thus obtained, are highly dependent on the coverage and fidelity of the Thermo-Calc databases used. For com-

plex alloy chemistries, such as multi-principal element alloys the software may have to interpolate between sparse input data points or extrapolate beyond them. Moreover, the present study does not utilize independently calibrated models and the quantitative accuracy is determined by good agreement with literature trends. All of these factors may introduce some uncertainty in the final predictions.

Absorptivity Calculation and Limitation

Absorptivity is approximated using the series expansion for emissivity in a direction normal to the surface, based on Drude's Theory (Equation 4.1). [45] Here, $\varepsilon_\lambda(T)$ denotes the emissivity at a given wavelength (λ) and temperature (T) where the conductivity of a metal (γ) is expected in units of $(\Omega \cdot \text{cm})^{-1}$.

$$\varepsilon_\lambda(T) = \frac{0.365}{\sqrt{\gamma\lambda}} - \frac{0.0667}{\gamma\lambda} + \frac{0.006}{\sqrt{(\gamma\lambda)^3}} - \dots \quad (4.1)$$

Since resistivity (ρ) and conductivity (γ) are reciprocal properties ($\gamma = \frac{1}{\rho}$), Equation 4.1 can be modified to accept our computed electrical resistivity value and near infrared wavelength of 1070 nm. (Equation 4.2).

$$\varepsilon_\lambda(T) = 0.365\sqrt{\frac{\rho}{\lambda}} - 0.0667\frac{\rho}{\lambda} + 0.006\sqrt{\left(\frac{\rho}{\lambda}\right)^3} - \dots \quad (4.2)$$

This approximation provides a simple estimation of a given alloy's absorptivity and serves a baseline value to use with melt pool calculations. A more comprehensive approach would include the absorptivity value's dependence to applied power and the reflections observed within a melt pool during keyholing[160, 227]. For alloys such as copper which exhibits a large range of absorptivity values (around 5% to 90%)[160] depending on power and laser conditions, the predicted results may be limited by the stated assumptions. Our approach is validated by comparison with experimental data in Appendix D[58, 98, 105, 150].

4.2.2 Lack of Fusion Defect Prediction

Defects created within the laser powder bed fusion process can arise through various means and affect the final part's material and mechanical properties[59, 90, 158]. This includes defects such as porosity, microstructural inhomogeneity, and inclusions which can result in degraded performance in fatigue life as well as mechanical strength[37, 90]. The source of these defects can be attributed to at least one of the following process map defect regimes of either Lack of Fusion (LoF), Keyholing, or Balling[60, 90]. Of these defects, porosity lack of fusion porosity is often larger than that generated by keyholing or balling [204]. Pores presents a significant risk to the fatigue life as it provides a starting point for cracks to nucleate from[37, 208].

The criterion for lack of fusion is primarily concerned with overlap between subsequent melt pool tracks, where adjustments to the hatch spacing along with layer height determine the extent of unfused powder within the scan track.[90, 218] This is modeled by with Equation 4.3[90, 171, 218] where computed ratios greater than 1 are expected to exhibit lack of fusion defects.

$$\left(\frac{\text{Hatch Spacing}}{\text{Melt Pool Width}} \right)^2 + \left(\frac{\text{Layer Height}}{\text{Melt Pool Depth}} \right)^2 \leq 1 \quad (4.3)$$

Hatch spacing and layer height are independent process parameters that are prescribed for the build process. Melt pool dimensions of depth and width are physical values that obtained from either cross-sectional measurements of the scan track[17] or modeling using solvers such as that of the Rosenthal[191, 217, 218] equation (Equation 4.5).

Dimensional Approximation of the Melt Pool

In Equation 4.5, the local temperature T (K) is obtained at a distance z (m) along the travel direction for a radial distance R (m) from the beam position[191, 217]. Additional factors such as the temperature of the plate T_∞ (K), applied power Q (W), scan speed V (m/s), thermal diffusivity α (m^2/s), and thermal conductivity k (W/mK) utilized to provide an approximate calculation of the temperature field[191, 217]. Thermal diffusivity ($\alpha = \frac{k}{\rho C_p}$)

can be obtained from thermal conductivity k (W/mK), density ρ (kg/m³), and specific heat capacity C_p (J/kg·K). Radial distance R is the combined coordinate of $R^2 = z^2 + r^2$ where z (also $-\xi$) is the distance along the center line.

$$z = R + \frac{2\alpha}{V} \ln \left(\frac{2\pi kR\Delta T}{\epsilon P} \right) \quad (4.4)$$

Given the liquidus temperature of a material, Equation 4.5 can be rearranged to provide the bounds of the melt pool. This is shown with Equation 4.4, where $\Delta T = T_{melting} - T_{initial}$ and ϵ represents the dimensionless absorptivity value. The length of the melt pool can be obtained by calculating the length of the temperature field in front and tailing the heat source. The tailing length (Equation 4.15) of the heat source can be obtained from setting the z to R and then solving for R as seen with its derivation included in 4.8.2. This provides a stop point when passing R values into Equation 4.4 with a step size of 1 um when calculating the bounds, recording the maximum to use as the melt pool dimensions.

$$T = T_\infty + \frac{Q}{2\pi kR} \exp \left(\frac{V(z - R)}{2\alpha} \right) \quad (4.5)$$

Model Assumptions and Limitations

With Rosenthal's approximation of a moving heat source a number of assumptions are made which include a melt pool in conduction mode, a point heat source, and temperature-independent thermal properties[191, 218]. The derived melt pool dimensions are limited to a steady state conduction mode melt pool and when applied to the lack of fusion criterion it does not consider dimensional fluctuations of the melt pool that are present in experimental builds[134].

Since these melt pool dynamics are obtained through a purely conduction based approach, factors such as keyholing are not reflected in the obtained dimensions throughout the process map. When viewed through the lens of defects pertaining to lack of fusion, these dimensions present more conservative estimates to the process window. This is from the smaller depth estimations

of the melt pool in conduction mode as to that of a keyholing melt pool which has an elongated lower half[37, 90, 219]. Lack of fusion and keyhole defect regimes do have some degree of overlap however experimental data shows this occurs in combinations of low to medium power and low velocity ranges (Figure 4.12). Energy density can be used as an indicator for the transition between keyhole and conduction mode and for alloys with known energy density transition points, this value is used as a cutoff for conduction based melt pool dimensional approximations [37].

Defect Domain Scope and Applicability

Although this work primarily focuses upon the prediction of lack of fusion defects within a range of power and velocity combinations, it is worth addressing the other two common defect regimes of keyholing and balling.

Keyholing describes the elongated depth of the melt pool as it exits conduction mode, leading to potential defects that can also contribute to lower mechanical strength in the resulting build[37]. A common criterion for keyholing analyzes the width to depth ratio of the melt pool such that a melt pool with a depth 1.5 larger than the width is considered to be keyholing (Equation 4.6) [246].

$$\frac{Width}{Depth} > 1.5 \quad (4.6)$$

However, in order to properly model keyhole behavior within the melt pool, a computational fluid dynamics approach is required to capture effects such as solid/liquid interfaces and the driving force of recoil pressure from material vaporization[125]. Solvers from FLOW-3D[2] and OpenFOAM[16] provide the capability to model these fluid dynamics but present a non-trivial challenge to integrate into this agentic system as they require both significant time and computational cost.

Balling presents another potential source of defects which often occurs at high power and velocity combinations, the grooves generated from the capillary forces initiate voids within the build if not remelted in a subsequent pass[94]. A simplification of the criterion for balling is comparing the length

to width ratio of the melt pool to a set threshold, such as π , such that any ratio greater would indicate balling[246] (Equation 4.7).

$$\frac{Length}{Width} < \pi \quad (4.7)$$

For the case of balling, a threshold based on the ratio length and width of the melt pool is rather simplistic and presents an assumption that this behavior occurs based on the dimensions of the melt pool. Whereas, factors such as the temperature balance between the melt pool and the solid surface provides a more grounded approach to capturing the underlying behaviors that would contribute to balling phenomenon[137]. With this, CFD approximations or surrogate modeling would suit as better options to modeling the potential occurrence of balling, however are not integrated in this approach for previously mentioned reasons.

4.2.3 Model Context Protocol

The Model Context Protocol (MCP) is a standard introduced by Anthropic[24] which provides guidelines for used functionality such as tool calling and resource querying; Particularly suitable for agentic tasks[15, 23, 73, 106]. Along with these features, MCP is compatible with the wider ecosystem of LLM providers with integrations in Software Development Kits (SDKs) developed by Anthropic[15], OpenAI[7], Google[97], and others[106].

Tools

Tools are the primary means in which an LLM is able to perform actions via MCP, invoking external Application Programming Interfaces (APIs) or function calls with the user's approval [15, 73, 106]. Complexity of these tool calls can range from simple stateless actions (network requests to external APIs) or long-lived function operations (simulation runs)[15]. Using the MCP Python SDK[15], these tools can be exposed to the LLM with the appropriate decorator function configuration as seen in 4.8.1. A minimal configuration consisting of the decorator wrapping a tool function is sufficient to register a tool for an LLM. However, additional annotations such as type declarations, docstring

descriptions, and structured outputs significantly improve the model's comprehension and proper utilization of the defined tool.

Resources

Resources provide the LLM capability to search for relevant information regarding a given task. Similar to GET requests established within the Hypertext Transfer Protocol (HTTP)[15], this allows for the query of information stored within databases, filesystems, or other means to be accessible to the LLM[73, 106]. This is particularly useful during the tool calling process as it provides environmental state information regarding around the model. However, during experiments the LLM's utilization of the resource functionality proved unreliable and tools implementing the same functionality of each resource displayed consistently reliable responses.

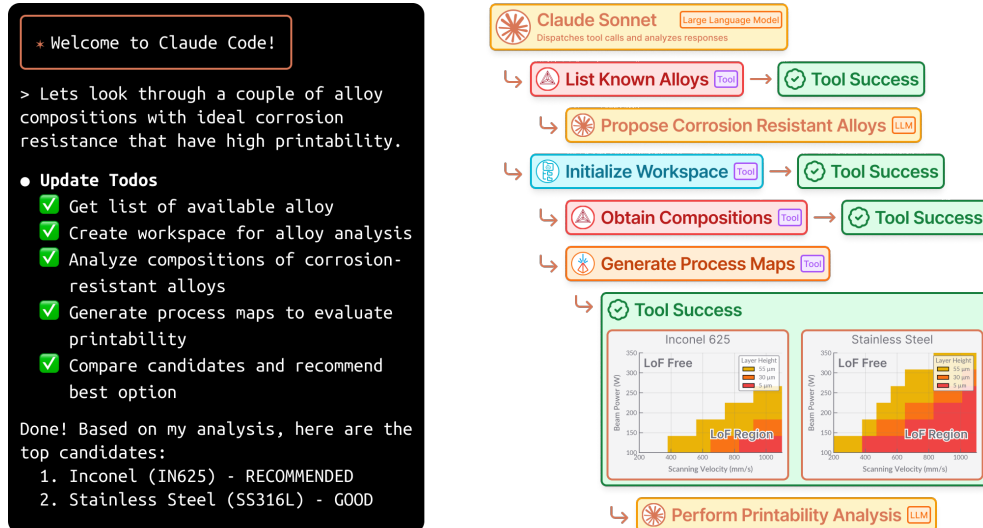


Figure 4.2: **(Left)** Claude Code provides an interface for integrating agentic tools with Claude Sonnet LLM, allowing for natural language input to execute tasks and response analysis. **(Right)** Streamlined summary of tool executions and analysis from the prompt given to Claude Code utilizing subagents for Additive Manufacturing, Thermo-Calc, and Workspace.

4.2.4 Agentic Tools

Tools developed for this application are separated into three different MCP Servers with Python Package Index (PyPi)^[9] identifiers: `additive-manufacturing`, `thermo-calc`, and `workspace-agent`. Each of these packages maintain their own MCP server tools and *Subagent*^[10] (a simple markdown file providing additional context and system prompts to guide tool usage) and are capable of standalone usage. Claude Code^[1] provides a platform for coupling these tools into a multi-agent environment utilizing Claude Sonnet 4^[3] as the primary large language model for orchestrating tool calls and performing response analysis.

Workspace

The `workspace-agent` package, abbreviated to `wa` internally, is responsible for the initialization and management of workspaces within the context of tool calls. It primarily acts as a state management tool for storing JSON serialized class objects and deserializing the stored JSON files to use within tools. This approach allows for different tools to use the same Python class methods and state since the input types to each tool are limited to primitives accessible via command line. Thus, filename references to serialized JSON files are provided as inputs to be loaded and deserialized within each tool since string, int, and formatted list and dict types are valid inputs to tools but Python instances of classes or functions are not.

Workspaces can be initialized via tool call (Figure 4.3) and are subdivided into top-level subfolders (i.e. `compositions`, `materials`, `process_maps`, etc.) containing state and responses for a given domain. Tools to list existing subfolders and their contents act as guides to help the LLM navigate through potential tool input arguments narrow the search window to the most applicable candidates. In addition to being listed as tools, functionality to list subfolders and their content are also exposed as resources accessible via MCP allowing for the LLM and user interface to obtain this information implicitly via syntax (i.e. `@workspace://{{workspace}}/{{subfolder}}/`).

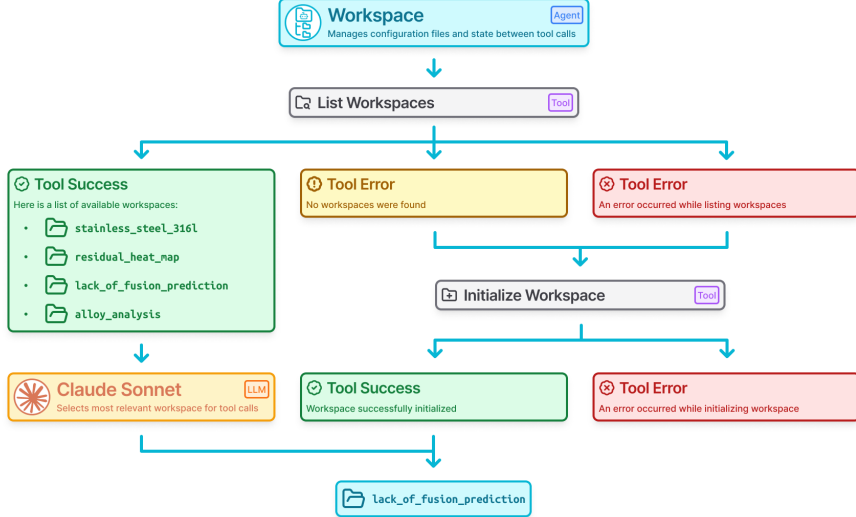


Figure 4.3: A simple tool calling procedure within the Workspace subagent for the task of finding or initializing a workspace. Here an initial tool call is made to list available workspaces and if none are found, a new workspace is created. This newly initialized workspace or the most relevant selected by Claude Sonnet is included in the successful response object.

The MCP server for workspaces operates independently, acting without direct knowledge of other installed MCP servers relying only on the LLM context to provide the appropriate arguments for workspace names and sub-folders to navigate. This architecture allows for the other MCP servers to utilize workspace functionality preventing the issue of tool overlap between packages. This opinionated approach allows for MCP servers that utilize `workspace-agent` to share workspace subfolders such that the output of one MCP server’s tool can be utilized as an input to another MCP server tool.

Thermo-Calc

For this project, the authors developed and published a package with the PyPI[9] identifier `thermo-calc` (aliased internally as `tc`) to facilitate the installation and use of Thermo-Calc’s TC Python module[222]. Along with these installation scripts, Command Line Interface (CLI) and MCP bindings were also implemented for a subset of TC Python’s functionality, those of

which are outlined in Section 4.2.1. With the set of tools managed by the thermo-calc subagent, the material properties of a given alloy composition can be calculated and saved to a shared material configuration that the tools from `additive-manufacturing` can then utilize for process map generation.

In this process, an hypothetical alloy composition element or an existing element name is provided to the large language model in order to create an alloy composition file (Figure 4.4). An alloy composition file is produced by serializing provided element proportions to a JSON file consisting of element keys and mass fractions. (i.e. `{"Fe": 0.9, "C": 0.1}`) Both approaches eventually utilize the alloy composition schema tool, however if the subagent is provided a generic alloy name, it utilizes tools to list known alloys and obtain their compositions to then pass into the alloy composition schema tool.

Once the alloy composition is obtained, the TC-Python API is called to instantiate a server to calculate the Property Diagram for the given set of elemental compositions and temperature range. This returns a `PropertyDiagramResult` which is then saved for later use when calculating phase transition temperatures and other material properties. In a separate tool call, the `PropertyDiagramResult` is loaded for the volume fraction calculation of the liquid phase which the liquidus and solidus phase transition temperatures can be extracted from. The liquidus, solidus, and melting (midpoint between liquidus and solidus) are then saved into a phase transitions temperatures configuration file and utilized later in the calculation of other material properties and serialization of the material schema.

The previously calculated values are managed by `workspace-agent` package and are saved in the `property_diagrams`, `phase_transition_temperatures`, and `compositions` subfolders respectively. The relevant configurations are loaded from these subfolders into the material compilation tool which determines the values for the remaining material properties, those being specific heat capacity, density, thermal conductivity, and absorptivity. These values are instantiated as `Material` class and serialized into the `materials` subfolder as a JSON file for lack of fusion process map generation.

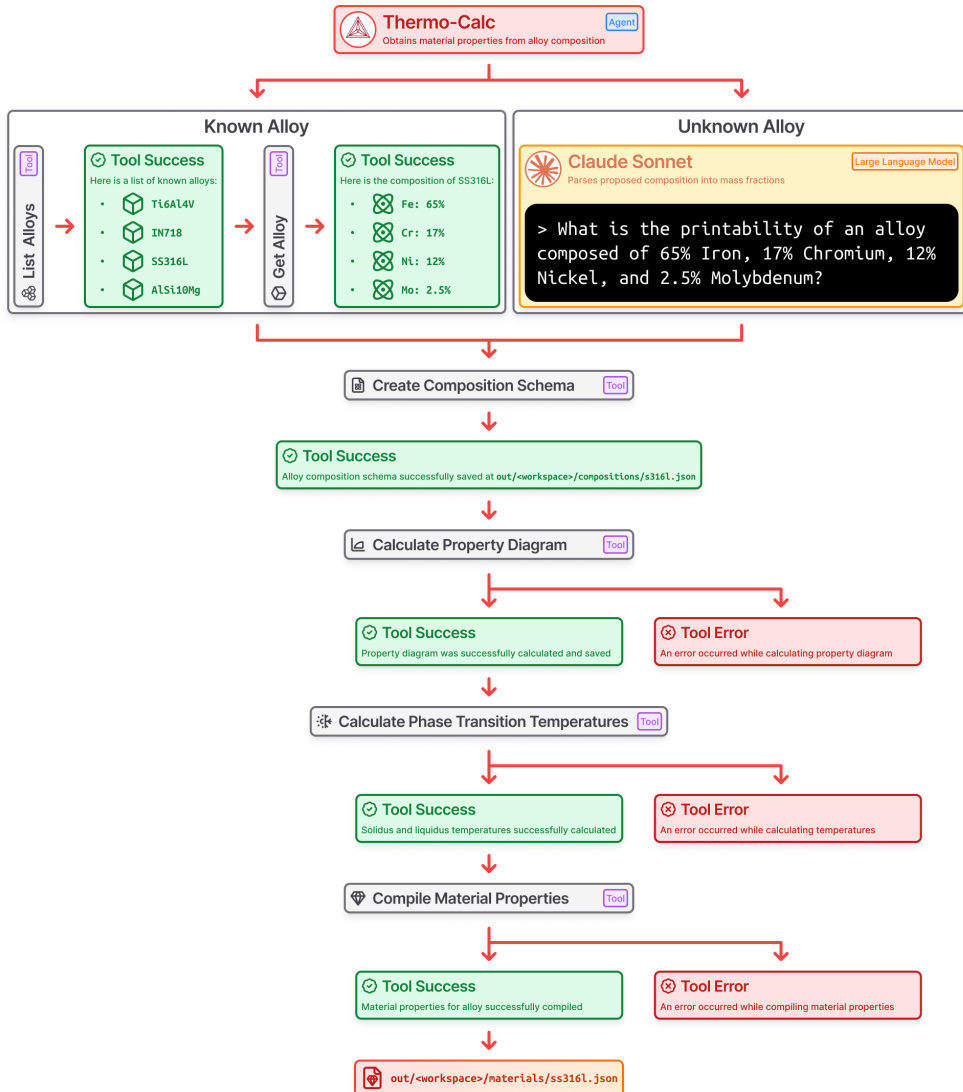


Figure 4.4: Flow diagram outlines the expected tool calling procedure for the Thermo-Calc subagent. In this example the material properties for Stainless Steel are extracted from the calculated property diagram of the alloy's elemental composition. Composition is obtained from a look-up table of known alloys or provided directly to the agentic system and parsed into mass fractions using Claude Sonnet. This process generates a schema file with alloy's material properties recorded for downstream use with other tools.

Additive Manufacturing

The `additive-manufacturing` (`am`) package provides a set of tools to assist with the additive manufacturing build process, currently built around providing feed forward solutions to predict potential build defects and gauge its feasibility. Of the available features, the experimental setup primarily utilizes the package's process map generation capabilities in order to predict potential lack of fusion defect regimes. The exact process for computing the melt pool dimensions necessary for determining the lack of fusion defect regime is outlined in Section 4.2.2, but in short, melt pool dimensions are calculated using an equation from Rosenthal [191] and fed into the lack of fusion defect criterion (Equation 4.3) to classify the input process parameter combination. In the current implementation classifications are limited to within or outside the lack of fusion defect regime as the analytic solution only works for conduction mode and cannot model melt pools in keyhole mode[191].

Process map generation is managed by the additive manufacturing sub-agent responsible for the relevant tools within its MCP server (Figure 4.5). To achieve this configuration files for desired materials and build parameters need to be created before the process map can be initialized and generated. Material configuration contains material dependent properties such as density, thermal diffusivity, thermal conductivity, and liquidus and solidus phase transition temperatures to name a few. Build configuration manages values such as beam power, scan velocity, layer height, and hatch spacing. These configuration files are utilized by the process map initialization tool which creates the subfolder for storing process map results and the process map configuration file for overriding build parameter configurations of beam power and scan velocity. Instead of a single scalar value, process map configuration file overrides the build configuration file with a range of values as to use the same material and build configurations when calculating defect regimes but with either a different power or velocity. The default process map range for power and velocity is 100 to 1000 with steps every 100 W or mm/s respectively. With this, the necessary calculations are performed to obtain lack of fusion regimes for 2 layer heights (-25 μm and +25 μm) in addition to the prescribed layer

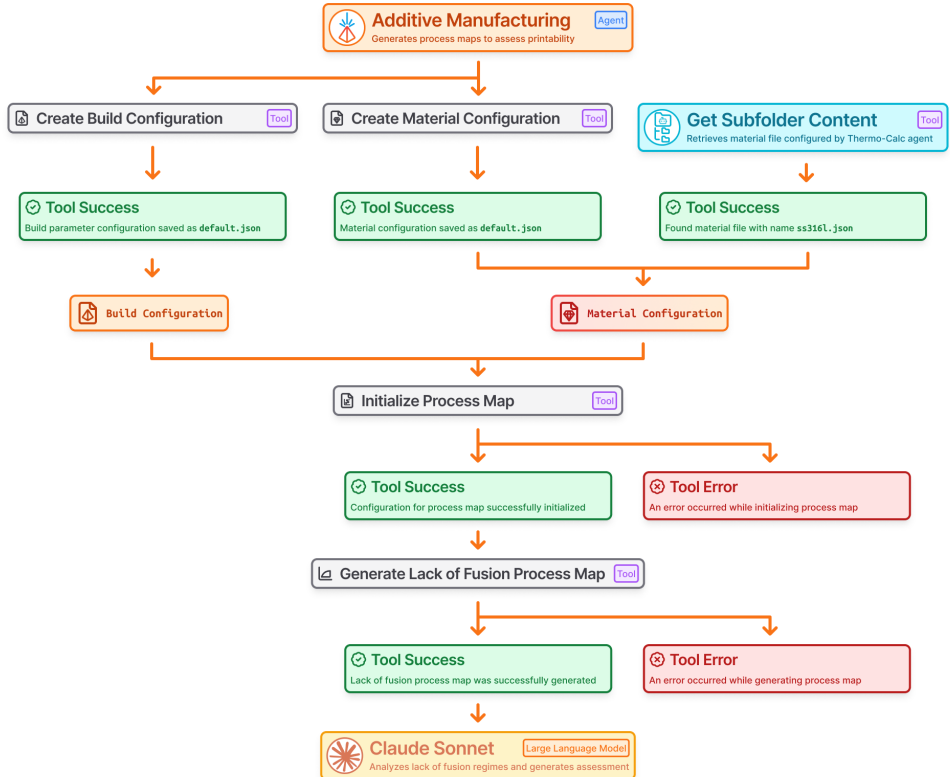


Figure 4.5: Diagram outlines expected tool calling procedure for additive manufacturing subagent for the task for generating and analyzing a lack of fusion process map. Build and material configurations are required to initialize a process map, the latter of which can be obtained from the Thermo-Calc subagent or manually configured by the additive manufacturing subagent. Initializing the process map provides override ranges for power and velocity build parameters for melt pool depth calculations. The tool generates the process map and a response consisting of power and velocity configurations that potentially exhibit lack of fusion defects. Claude Sonnet analyzes this response and provides suggestion for optimal build parameters.

height within the provided range of process parameters.

The Command Line Interface (CLI) provides the basic means of interaction with the `additive-manufacturing` package, however with its MCP integration, inputs and arguments can be left unstructured and functionality is accessible through just natural language when utilized as tools within an MCP server. In addition to natural language functionality, its integration with an LLM (i.e. Claude Sonnet) augments the capabilities of the user enabling easy evaluation of follow-up changes and LLM enabled analysis and feedback of computed results. Through the `workspace-agent` package, material configurations generated with the `thermo-calc` package can be utilized for the generation of process maps, allowing for the end-to-end functionality of proposing alloy compositions to analyzing their lack of fusion process map.

4.2.5 Experiments

Several experiments were performed to investigate the capability of the agentic system. Each experiment consists of a simple prompt regarding the desired alloy or material properties to explore (as shown in Figure 4.2) with the expected generation of a lack of fusion process map along with analysis and suggestion of potential printing parameters to implement. The whole of these experiments aims to cover the wide range of potential use case scenarios supported with the provided tools ranging from known and novel alloy compositions to searching and assessing alloys with a desired material property characteristic.

Known Alloy Compositions

Within the scope of known alloys, the system is expected to adhere to the established approach to obtaining a process map for a given material compositions with the caveat of obtaining these alloy composition from a provided dictionary. In this task it is expected that the LLM only acts to dispatch tools and interpret their subsequent response. This approach would be evaluated on a subset of the known alloys which include: Stainless Steel 316L, Titanium,

Inconel, Aluminum, Tool Steel, Iron, Copper, Hastelloy X, K500, Tungsten, Bronze, and Aluminum 7050.

Material Property Search

For an open ended task, such as that encountered during the search for an alloy composition with specific desirable material properties, the large language model is utilized more. In this case, a similar approach to that of the known alloys is taken to determine an alloy's lack of fusion regime with an initial query given to the LLM to provide a list of candidates with the desired material properties. This included properties such as corrosion resistance, fatigue life, yield stress, Young's modulus, fracture toughness, hardness, and ductility.

Novel Alloy Compositions

The LLM is able to interpret a combination of elements into their respective mass fractions and call the relevant tools to determine the alloy's lack of fusion regime. Compositions outside that of the known alloys were also included in this investigation which primarily entailed the modification of existing alloy compositions such that an element was to be removed or the proportion of one was to be increased. In addition, the agentic system also accepts an hypothetical combination of elements along with their prescribed proportions. This hypothetical combination of elements provides the freedom to combine various elements, such as 50% Fe and 50% N, into the system but in practice is limited by the bounds of thermodynamic calculations and databases of Thermo-Calc. The system was primarily evaluated with compositions ranging from slight modifications of known alloys with a couple of completely hypothetical combination of elements to element compositions proposed by the LLM.

4.3 Results

For the known alloys, the lack of fusion process map was obtained using the provided alloy composition. In these experiments, the large language model is

responsible for the selection of build parameters along with defining the appropriate process map range within the power and velocity process parameters. Of the 12 alloys this experiment was performed upon, 11 were able to produce a suitable lack of fusion process map (Figure 4.6). The one failure in this case occurred with the Tool Steel prompt which resulted in the process hanging while utilizing the property diagram calculation tool. This is potentially due to the number of potential options for "Tool Steel" that the MCP tool had available such as "D2 Tool Steel", "M2 Tool Steel", "A2 Tool Steel" which required further clarification.

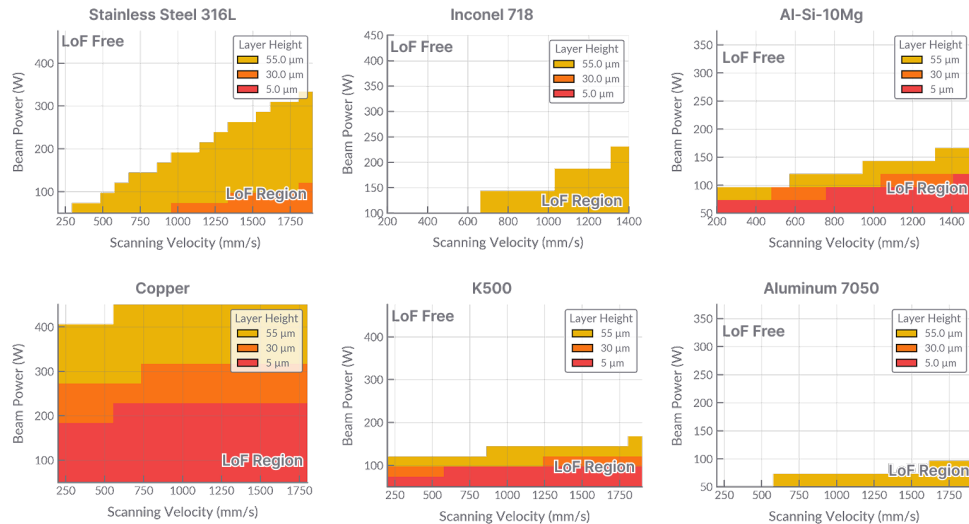


Figure 4.6: Lack of fusion process maps for a selection of known alloys with default hatch spacings of $50\mu\text{m}$ and various layer heights indicated by their respective colors within the legend.

When prompted to search for an alloy with a specific material property, the LLM reasons through number of potential candidates and selects a couple to evaluate. The same procedure is taken for generating process maps for each alloy candidate the results of which are evaluated and compared with emphasis towards minimizing lack of fusion (Figure 4.7). Of the 9 investigated material properties, the agentic system failed to produce process maps for only one of the cases. The failure case occurred while comparing creep

resistance of various alloys, specifically when attempting to generate the process map investigating the nickel based superalloy, Mar-M 247. Besides this exception, all prompts were successful in creating lack of fusion process maps and performing analysis and recommendations based on the feasibility of each alloy candidate.

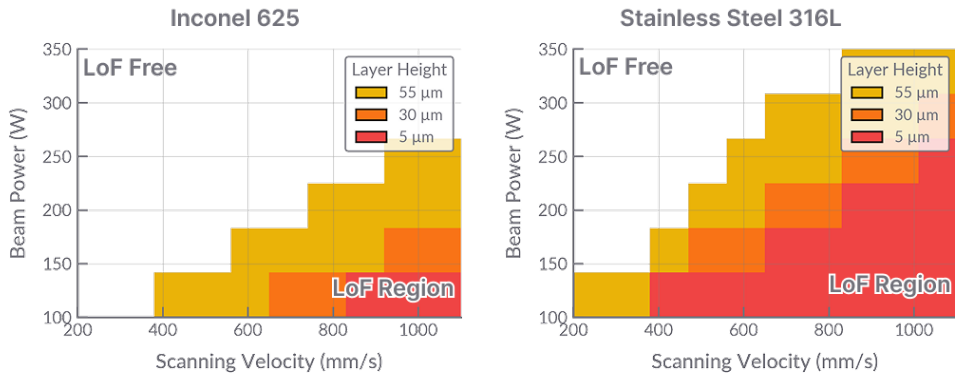


Figure 4.7: Comparison of lack of fusion process maps of between Inconel 625 and Stainless Steel 316L for corrosion resistant applications. Between these two candidates, the LLM ultimately recommended the use of Inconel 625 for its smaller lack of fusion regime.

For the application of corrosion resistance (exact prompt and response provided in 4.8.6), the additive manufacturing subagent recommendation of Inconel 625 aligns with the findings from multiple literature sources[47, 74, 248]. In a study by Zhang et al.[248], the authors investigate corrosion resistance of Inconel 625 and Stainless Steel 316L hybrid alloys under the application of hydrofluoric acid. Inconel is stated to have greater corrosion resistant properties than that of Stainless Steel 316L however, due to its higher Nickel and Chromium content the manufacturing cost is higher as well[248]. Process parameter combinations used with Inconel 625 range from 175 W and 500 mm/s[89] to 1000 W and 600 mm/s[248], all of which are valid process parameters within the prediction of the additive manufacturing subagent.

For novel alloys, compositions are directly evaluated and in some instances produce rather extreme process maps. Of the 10 conducted experiments, 8 were successfully able to produce process maps with 2 failing due to the na-

ture of the alloy composition. Although the system accepts any composition of elements, most hypothetical combination of elements are unsuitable for printing and practical use. As such, slightly adjusting known alloy combinations produces more suitable lack of fusion regimes as seen in the cases where Molybdenum is removed for Stainless Steel 316L or Inconel 625 (Figure 4.8).

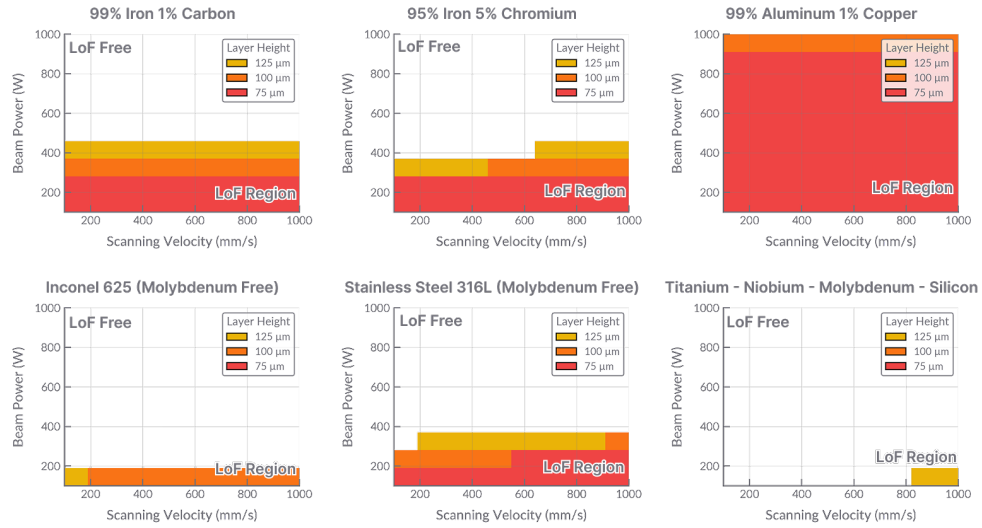


Figure 4.8: Various lack of fusion process maps for novel alloy compositions. (**Top Row**) Hypothetical element compositions for proposed Iron and Aluminum based alloys. (**Bottom Row**) slightly modified known alloy compositions of Inconel and Stainless Steel 316L with the removal of Molybdenum. (**Bottom Right**) An LLM proposed composition when prompted to suggest an novel alloy.

4.3.1 Lack of Fusion Validation of Known Alloy Compositions

Validation was performed on a couple of the common predicted alloy compositions (IN718 and SS316L) to ensure the predicted lack of fusion process aligned with what is found within the literature. In addition, the expected material properties associated with each alloy along with the associated processing parameters were included to provide broader context to what is expected from each alloy.

Inconel 718

Validation of the lack of fusion predictions of known alloys indicate satisfactory overlap between those generated by additive manufacturing subagent and that found within published literature. In a study by Ghanadi et al. [85], lack of fusion was observed at laser powers between 50 to 150 Watts and scan speeds of 700 mm/s to 1200 mm/s when conducted with a prescribed layer height of $25\mu\text{m}$ and hatch space of $40\mu\text{m}$. These process parameters are similar to those implemented using the additive manufacturing subagent ($50\mu\text{m}$ hatch spacing and $30\mu\text{m}$). Although the generated process map for Inconel 718 (Figure 4.6) denotes a slight under prediction of lack of fusion compare to that of the literature, this can be attributed the more general applicability of Rosenthal's equation[191].

The study provides areal surface roughness (Sa) of the top and sides of their printed lattice structure as an indicator for lack of fusion. The authors observed the expected trend that the Sa values decreased with increasing laser power and increasing scan speed, where the lowest Sa value of $26.5 \pm 5.4 \mu\text{m}$ with an ultimate shear strength of $153.2 \pm 7.7 \text{ Mpa}$ and shear strain of 0.33 ± 0.02 at 150 Watts and 200 mm/s[85]. The highest Sa occurrence of $70 \pm 8.9 \mu\text{m}$ with an ultimate shear strength $8.93 \pm 0.9 \text{ Mpa}$ and 0.69 ± 0.03 shear strain recorded at a 50 Watts and 1200 mm/s power and velocity combination[85].

Stainless Steel 316L

The generated process map for Stainless Steel 316L (SS316L) matches the lack of fusion regimes outlined in the literature, with unfavorable process windows at lower powers and higher velocity combinations[19, 107, 174]. Ahmed et al.[19] encounters high densification of SS316L at power and velocity combinations of (150 W, 500 mm/s), (200 W, 700 mm/s), (250 W, 900 mm/s), and (300 W, 1100 mm/s), matching that presented in Figure 4.6.

Within the lack of fusion defect regime, the resulting pore size is heavily dependent on the factors of height and width of the melt pool along with the hatch spacing and layer height of the build[48, 172]. For hatch spacings ranging from $25 \mu\text{m}$ to $55 \mu\text{m}$, equivalent pore sizes upwards of $160 \mu\text{m}$ can

be observed (power at around 100 W, 30 μm layer height, and 1.4 m/s scan velocity)[172]. Within the range of scan velocities from around 1.05 m/s to 1.75 m/s, an average pore diameter of around 30 μm with a standard deviation of 16 μm and approximate maximum of 130 μm was observed (with previously mentioned process parameters and 50 μm hatch spacing)[172].

In more nominal processing conditions, the percentage of porosity within a part is observed to change as a function of energy density. This is reflected in work by Tucho et al. where the authors manufactured a number of samples and recorded that porosity by volume within a part decreases from over 3% with energy densities of around 50 J/mm³ to less than 1% at energy densities of 65 J/mm³[228]. The authors also found that hardness increases linearly with energy density as a hardness values of 188 \pm 4 HV was observed at an energy density of 80 J/mm³ from a value of 168 \pm 15 HV at an energy density of 50 J/mm³[228]. With regard to mechanical properties, it was found that tensile strength and yield strength could be improved through layer remelting as Lu et al. recorded a respective increase from 674 MPa to 725 MPa and 591 MPa to 643 MPa with process parameters of power at 250 W, scan velocity at 950 mm/s, hatch spacing of 110 μm , and layer height of 30 μm [19, 141].

4.4 Discussion

In this agentic system, all tasks are completed with tools performing deterministic actions; the large language model merely orchestrates and analyses the response of dispatched tool calls. As a result, fidelity of the system's predictions relies primarily on the accuracy of the developed tools. To that point, this work limits its process map prediction to the lack of fusion regime as it utilizes a conduction mode limited analytical approach to obtain melt pool dimensions[191]. With these separation of concerns, determining the source of invalid predictions is simplified where incorrect evaluation of results can be attributed to the large language model and production of inaccurate predictions can be assigned to the tool.

Within the experimental trials a few prompts produced incorrect results as such was the case in evaluating a material with optimal hardness. In

this case the lack of fusion process maps were correctly generated however the LLM recommended the use of Enhanced Maraging Steel over the other two candidates (Figure 4.9). From visually interpreting the process maps, it is clear that Enhanced Maraging Steel has the largest lack of fusion regime when compared to its counterparts. One potential cause of this misinterpretation could be attributed to the response data structure returned to the LLM after a tool call. Since the lack of fusion regimes are returned as power and velocity combinations within a list of tuples (i.e. $[(100, 100), (150, 100), \dots]$), the LLM may have misinterpreted these values to be valid process windows rather than lack of fusion regimes. Proper key names and serializing of results would help reduce these types of LLM mistakes.

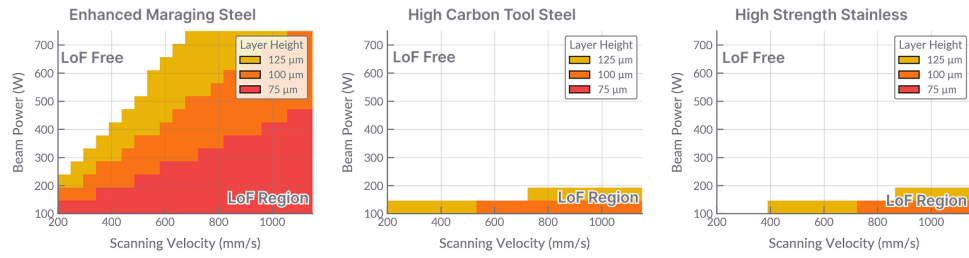


Figure 4.9: High hardness alloy candidates with their respective lack of fusion process maps. LLM makes an error by recommending Enhanced Maraging Steel over High Strength Stainless Steel for its smaller lack of fusion region.

The deterministic nature of these tools does present the question of the benefit of introducing an LLM into the system, as if the tools can work on their own individually, what would be the purpose of including an LLM into the architecture. This is a valid concern as the common workflows of each tool can be connected to each other through a parent script, achieving the same effect. However, the inclusion of an LLM and the separation of tools into their own subagents allows for several unique capabilities. The most apparent of these is the utilization of natural language when interacting with the developed tools. This allows the user to directly interact with the available tooling without explicitly adhering to the strict syntax and argument guidelines required by the CLI. Another is the LLM's ability to analyze results providing user interpre-

tive feedback on a tool’s response. This supports another key ability of LLM agents which is to establish a feedback loop and respond to changes within its context. The integration of LLM Agents within the developed tools not only enhances the user experience with these tools but establishes an automation framework enabling researcher to efficiently utilize their available tools.

4.4.1 Comparison to Existing Tool Integration Frameworks

Other alternatives to tool calling and agentic system frameworks exist to the Model Context Protocol (MCP) such as LangChain[4] and LlamaIndex[5], however, these approaches lack first party integration into the LLM that MCP provides. The alternative approaches are no less capable than MCP and have their own specific features as seen in other various agentic works [52, 115]. The primary reasoning behind using MCP as the framework for designing the agentic tools is expected long term support and ease of use that the protocol provides when applied to other models and the broader support it has with providers such as Anthropic, Google, and OpenAI. Although much of these tests were performed with the Claude model from Anthropic, initial implementations show that these experiments can be performed on the latest models from OpenAI (ChatGPT) and Google (Gemini) as well.

4.5 Conclusion

This multi-agent system augments the researcher’s ability to investigate and evaluate known and novel alloy compositions for processing via additive manufacturing. This is achieved through invoking tool calls via the Model Context Protocol (MCP) to perform thermophysical calculations and melt pool dimensional approximations to generate a lack of fusion process map. In addition, these tools can leverage the generalized knowledge of LLMs to assist in more generalized tasks such as suggesting alloy compositions for desired material properties through querying its large base of knowledge. The predictions from this system provide a suitable starting point of process parameters for experimental trials that would avoid potential areas of lack of fusion. Expansions upon this work would explore a more comprehensive search for processing pa-

rameters that would also consider the keyholing and balling defect regimes. This work sets the foundation for complex tool usage and automated research within the additive manufacturing field.

4.6 Future Work

Although the authors have provided a comprehensive study on the use of agentic tools within the additive manufacturing space, there remain a couple of aspects to this work that would benefit from further research.

4.6.1 Technical Roadmap

Objective

Extension upon this work would expand upon the generation of a robust process map which considers additional build parameter and processing factors such as beam size, melt pool fluid dynamics, and varying absorptivity. Specifically, process regimes for keyholing and balling would be incorporated into the final alloy evaluation when selecting a set of build parameters within a process window. Additionally, validation of novel alloy compositions and process parameters proposed by the agentic system would include fabricating samples evaluation through tensile tests.

Methodology

In order to obtain melt pool dimensions which more accurately match those created experimentally, a more comprehensive solver will need to be utilized. Options include CFD solvers developed by FLOW-3D [2], OpenFOAM[16], or one specifically for the purpose of defining defect regimes. With each of these approaches, the tradeoff between computational cost and accuracy would be of primary concern.

Within the agentic system, the overall framework will still build upon the Model Context Protocol and further utilize features such as resources and tool calling. Design improvements would include tool consolidate to reduce potential tool bloat and clarify adjustments to reduce the frequency of faulty

tool calls. Additionally, consideration towards optimizing token and time cost between various LLM providers will be incorporated as well.

Evaluation Metrics

Evaluation of the updated solver will compare the melt pool dimensional values to those observed within the literature. Metrics here will include the percent error observed between the two dimensional measurements. Additionally, the solver's ability to model behaviors such as balling and keyholing will be scrutinized further and the computed defect regimes will be contrasted to those found within the literature.

Sample fabrication would have a more qualitative evaluation metric as machine or composition specific factors may hinder the manufacturing of parts consisting of novel alloy compositions. A scenario where the novel composition sample is ultimately fabricated but under a certain process conditions not mentioned by the agentic system. After fabrication, the mechanical properties such as yield strength, ultimate tensile strength, and hardness would be evaluated as well.

Timeline

The objectives outlined within this technical roadmap such as improvements to the agentic system are currently in progress and will be expanded upon further in a future work. Other considerations such as part fabrication and mechanical testing relies on the selection or development of a CFD solver that can produce more accurate melt pool dimensions suitable for a more comprehensive process map.

4.7 Data Availability

The multi-agent system developed for this work along with the data associated with experimental prompts are available at the following link: <https://github.com/BaratiLab/Agentic-Additive-Manufacturing-Alloy-Evaluation>.

The various tools within the agentic system are hosted on the Python Package Index (PyPI) and installable with their respective package names:

- `additive-manufacturing`
- `thermo-calc`
- `workspace-agent`

4.8 Appendix

4.8.1 Model Context Protocol Example Tool

4.8.2 Melt Pool Length

Rosenthal's equation[191] can be rewritten to provide the bounds for the melt pool. If z is substituted with R , the width of the melt pool shrinks to zero and becomes the furthest point in the melt pool.

$$z = R + \frac{2\alpha}{V} \ln \left(\frac{2\pi k R \Delta T}{\epsilon P} \right) \quad (4.8)$$

$$R = R + \frac{2\alpha}{V} \ln \left(\frac{2\pi k R \Delta T}{\epsilon P} \right) \quad (4.9)$$

$$0 = \frac{2\alpha}{V} \ln \left(\frac{2\pi k R \Delta T}{\epsilon P} \right) \quad (4.10)$$

Since the coefficient term $\frac{2\alpha}{V}$ will be a non-zero value, ignore this term to simplify calculation.

$$\frac{2\alpha}{V} \neq 0; 0 = \ln \left(\frac{2\pi k R \Delta T}{\epsilon P} \right) \quad (4.11)$$

Taking the exponential of both sides and solving for R produces the following equation that provides the expected length of the melt pool from the heat source.

$$e^{\ln(\frac{2\pi k R \Delta T}{\epsilon P})} = e^0 \quad (4.12)$$

$$\frac{2\pi k R \Delta T}{\epsilon P} = 1 \quad (4.13)$$

$$2\pi k R \Delta T = \epsilon P \quad (4.14)$$

$$R = \frac{\epsilon P}{2\pi k \Delta T} \quad (4.15)$$

```

1 @app.tool(
2     title="Run Layer with Solver",
3     description="Runs solver on a segments file (segments
4         file should be one layer) and saves the generated
5         meshes.",
6     structured_output=True,
7 )
8 def solver_run_layer(
9     workspace: str,
10    segments_foldername: str,
11    layer_number: int,
12    build_config_filename: str = "default.json",
13    material_config_filename: str = "default.json",
14    mesh_config_filename: str = "default.json",
15    run_name: str | None = None,
16 ) -> Union[ToolSuccess[Path], ToolError]:
17     """
18     Runs solver for segments at a specified layer number.
19     Args:
20         workspace: Folder name of existing workspace
21         segments_foldername: Folder name of where segments
22             are expected to be found.
23         layer_number: Layer number to run solver on,
24             typically starts from 1. For testing out, try
25             skipping the first several layers as those
26             sometimes don't include part geometry.
27         distance_xy_max: Maximum segment length when
28             parsing (defaults to 1.0 mm).
29         build_config_filename: build config file to use
30             with solver.
31         material_config_filename: material config file to
32             use with solver.
33         mesh_config_filename: mesh config file to use with
34             solver.
35         run_name: Name of folder to save generated meshes
36             at, typically autogenerated.
37     """
38     ...

```

Figure 4.10: Example tool implementation shown via Solver tool defined in additive-manufacturing package.

4.8.3 Database Selection

1. **Ti-based alloys:** if top element is "Ti" → TCTI6.
2. **Ni-based alloys:** if top element is "Ni" or the Ni fraction is ≥ 0.30 → TCNI12.
3. **Fe-based alloys:** if top element is "Fe" (and the previous Ni criteria were not satisfied) → TCFE14.
4. **Al-based alloys:** if top element is "Al" (and none of the above criteria applied) → TCAL9.
5. **Pure elements:** if we have a pure metal which is just a single element → PURE5.
6. **Fallback:** if none of the conditions above are met (maybe for MPEAs) → TCHEA7.

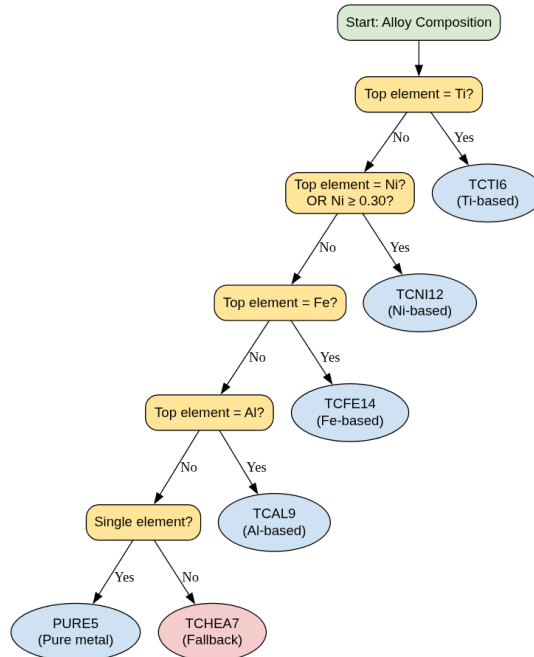


Figure 4.11: Database selection decision tree

4.8.4 Validation of Predicted Absorptivity

Alloy	Reported Absorptivity	Drude-Model Absorptivity
SS316L	0.35-0.60	0.4479
Ti-6Al-4V	0.27-0.6	0.4520
Hastelloy X	0.45–0.64	0.4413
M300 Steel	0.35	0.43

Table 4.1: Comparison between reported (literature) absorptivity and Drude-model calculated absorptivity at 1070 nm.

4.8.5 Lack of Fusion and Keyhole Boundaries of Known Alloys

Literature results for defect classifications regarding 316L Stainless Steel and Inconel 718 were analyzed to uncover potential lack of fusion and keyhole regions over a range of power and velocity combinations.[20, 219]. Logistic Regression was applied to determine boundary between the keyholing and lack of fusion regions. With respect to SS316L, a higher degree of overlap between these two defect regimes is visible due to the greater amount of samples when compared to that of the IN718 plot (Figure 4.12).

The boundary set by logistic regression implies that given the two defection classifications, if a defect were to occur it would be either keyhole or lack of fusion since it is expected that between these two regions a nominal process window could exist. This boundary is utilized as a threshold to limit the extent in which the Rosenthal's equation can be applied to determine lack of fusion defects before exiting conduction mode. In addition, sensitivity analysis on the boundary was performed by removing data points with the keyhole classification and the boundary was calculated only with lack of fusion data points. This resulted in a more conservative boundary in which defects would be classified as lack of fusion.

4.8.6 LLM Prompt and Response for Corrosion Resistant Material Property Search

The following prompt was provided to the agentic system:

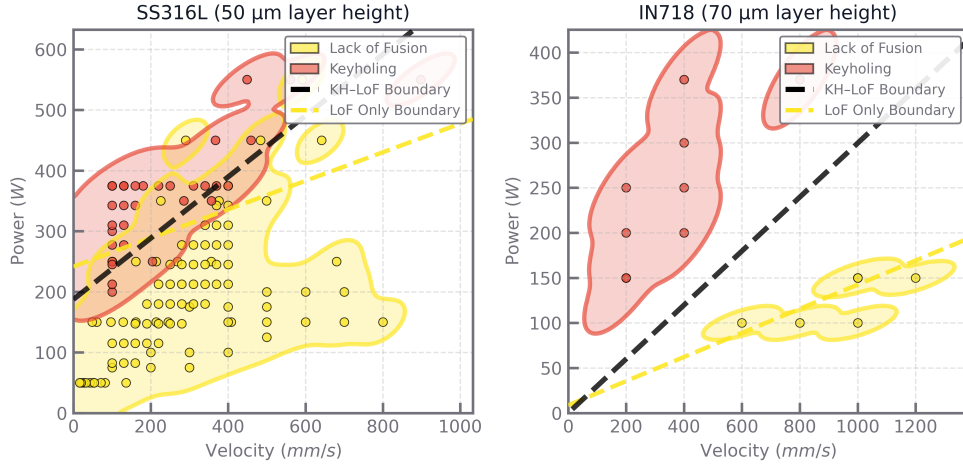


Figure 4.12: Literature values for SS316L and IN718 melt pool classifications expected defect regions for each respective alloy. Logistic regression is applied to establish a boundary between the two regions to reference as threshold to the extent in which Rosenthal's equation can be used to predict lack of fusion defects.

Lets look through a couple of alloy compositions to find a suitable candidate ideal for corrosion resistance that express high printability?

After successful tool calls, the LLM responded with the following:

```

1 Based on my analysis of corrosion-resistant alloys, here
2     are the top candidates:
3
4 IN625 (Inconel 625) - RECOMMENDED
5
6 Composition: 62.5% Ni, 22.9% Cr, 9.4% Mo, 5.2% Fe
7 - Corrosion Resistance: Excellent in marine, chemical,
8     and high-temperature environments
9 - Printability: Superior - Only 3 lack-of-fusion
10    conditions at low power (100W) with high velocities
11 - Process Window: Wide range of successful parameters
12    (150-400W, 200-1100 mm/s)
13
14 SS316L (Stainless Steel 316L) - GOOD ALTERNATIVE
15
16 Composition: 67.4% Fe, 17.6% Cr, 12.4% Ni, 2.6% Mo
17 - Corrosion Resistance: Very good, especially against
18    chloride environments
19 - Printability: More challenging - 17 lack-of-fusion
20    conditions at low power, 38 at higher layer heights
21 - Process Window: Narrower than IN625, requires careful
22    parameter control
23
24 Key Findings:
25
26 1. IN625 shows superior printability with fewer defect-
27    prone parameter combinations
28 2. SS316L has more extensive lack-of-fusion regions,
29    particularly at 55 m layer height
30 3. Both alloys offer excellent corrosion resistance, but
31    IN625 provides better process reliability
32
33 Recommendation: IN625 is the optimal choice, combining
34    exceptional corrosion resistance with superior
35    additive manufacturing printability.

```

Figure 4.13: Prompt response and reasoning provided by agentic system for evaluating lack of fusion process map for known alloys.

CHAPTER 5

PROPOSED WORK AND TIMELINE

5.1 Proposed Work: Agentic Process Optimization for Selective Laser Sintering

Within the additive manufacturing process there are many operational and environmental factors that can affect the build quality or build feasibility of the final part [48, 108, 218]. Mitigation of these effects is often achieved using feedforward process control where model based approaches are applied to anticipate problematic conditions that can lead to issues during the build process [44, 165, 241]. Feedback control addresses these issues during the build process utilizing visual [115], thermal [64, 251], or depth [206] information obtained through various sensors to dynamically adjust parameters and toolpath trajectories in an effort to resolve potential build defects. The use of specialized LLMs, referred to as *agents*, has enabled the intelligent automation of tool orchestration and feedback control for complex tasks within the space of additive manufacturing [115, 173] as well as other fields such as catalyst discovery [163] and mechanical design [113]. These advances enable automated thought, action, and observation workflows within the research process, utilizing perception and reasoning to make informed decisions to ensure successful task execution [84, 115, 163, 173]. In this proposed work an agentic system enables the intelligent automation of parameter optimization and *in-situ* process monitoring during the selective laser sintering process.

5.1.1 Experimental Platform

SLS4All Inova Mk1

The selective laser sintering process will be performed using the Inova Mk1 (Fig. 5.3) for a range of materials such as PA12, PA12 GF, and other experimental powder compositions. The Inova Mk1 is an open source, low cost,

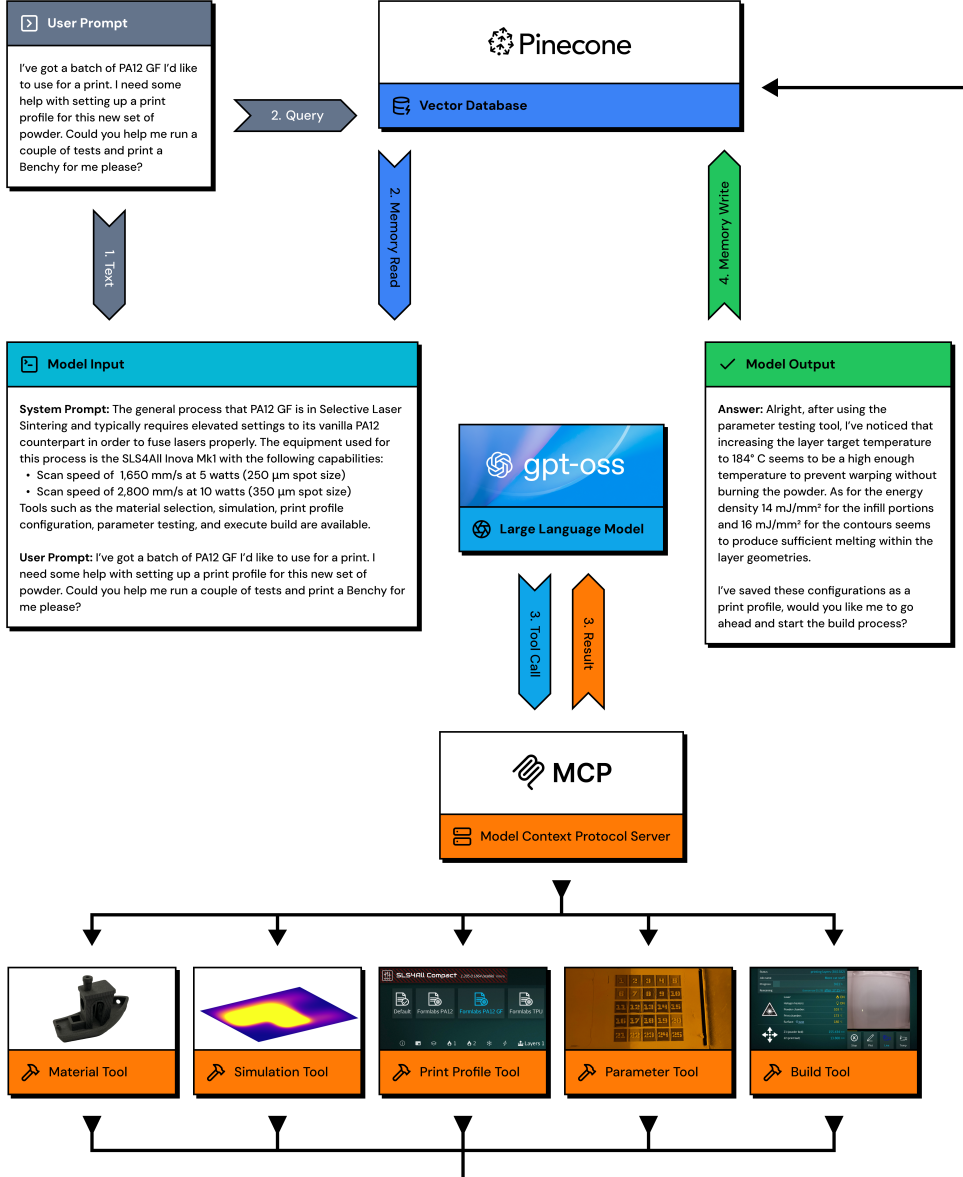
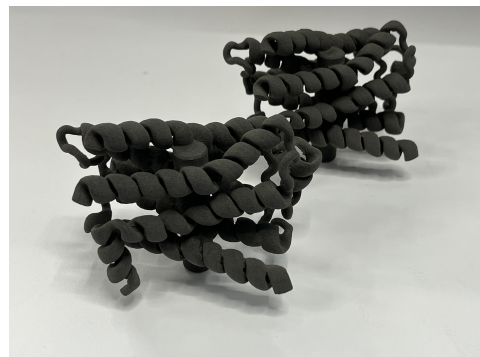


Figure 5.1: Flow diagram depicts simplified user interaction with agentic system for parameter selection and process monitoring for the Inova Mk1. (1) The user prompt is provided as model input (2) and (4) query for the vector database. Results from the vector database is appended to the model input and provided to a LLM. The LLM executes relevant (3) tool calls via MCP with their results added to the vector database. (4) Generated responses from the LLM are added to the vector database for use with future prompts.

selective laser sintering machine developed by SLS4All founders Tomas Starek and Pavel Dyntera [211]. This machine was purchased as kit from SLS4All and assembled over the course of several months producing successful prints (Fig. 5.2b) using Formlab's PA12 GF [78]. The Inova Mk1 utilizes a 450 nm blue diode laser capable of delivering 10 watts of power [211]. The machine is capable of an effective build volume of 150 mm x 150 mm x 185 mm and utilizes an array of 4 halogen lamps for surface heating control and a 5 heating elements for build chamber temperature control [211]. Surface temperature monitoring and control is achieved with a *ThermoCam Waveshare MLX90640* [6] capable of producing a 32 x 24 pixel thermal image for temperatures ranging from 0 °C to 300 °C. The optical camera utilizes an Omnivision OV5647 sensor capable of streaming a 1920 x 1080 pixel image at 30 frames per second. Average scan speed is around 1,650 mm/s at 5 watts (250 µm spot size) and 2,800 mm/s at 10 watts (350 µm spot size) [211]. The firmware controlling the hardware components such as the galvometers, laser, stepper motors, sensors, and heating elements runs off a combination of open-source software programs including *Klipper* [123], *SLS4All.Compact* [70].



(a) SLS4All Inova Mk1



(b) Printed β_2 Protein Model

Figure 5.2: Inova Mk1 (a) assembled from kit prints complex geometries, such as the β_2 protein molecule (b), only capable through the SLS process.

Platform Limitations

The Inova Mk1 present several software and hardware limitations. Although the software is primarily open-source, modules disclosing specific feature implementations such as part slicing and tool path generation are considered proprietary and only provided in a compiled state. In addition, there is little documentation regarding the machine's exposed Application Programming Interface (API) as the dashboard web interface is streamed from the host. With regard to the installed sensors, relative to thermal and optical imaging equipment used in other *in-situ* process monitoring works [44, 155, 156, 167, 172], the resolution and frame rate that these sensors provide is comparatively coarse. This adds a potential constraint to the quality of real-time information that can be utilized by the agentic system when testing process parameters and executing builds. The manufacturer also suggest material restrictions to primarily polymer based powders with a melting temperature of 200 °C [211].

5.1.2 Agentic System

The agentic system (Figure 5.1) will allow for the intelligent automation of parameter selection and process monitoring through the guidance of a locally deployed large language model (potentially GPT-OSS 20b [169]). Integration with a vector database (i.e. Pinecone) enables the use of dynamic memory such that previous system outputs and tool call results can be recalled for future prompts, providing additional context for the large language model to use during reasoning. Lastly, the system is able to interact with its environment through agentic tool calls following the Model Context Protocol. As indicated in Figure 5.1, these include tools for material selection, simulation, print profile configuration, parameter testing, and build monitoring.

Material Selection Tool

The material selection tool allows for inference on specified materials and their approximate properties. For example, if provided a mixture of various powders and additives, an approximation of critical temperature values such

as melting, glass transition, or solidus would be calculated. This would be achieved through a various ensemble of modeling tools ranging from a simple rule of mixtures to coarse resolution simulations depending on the argument complexity.

Simulation Tool

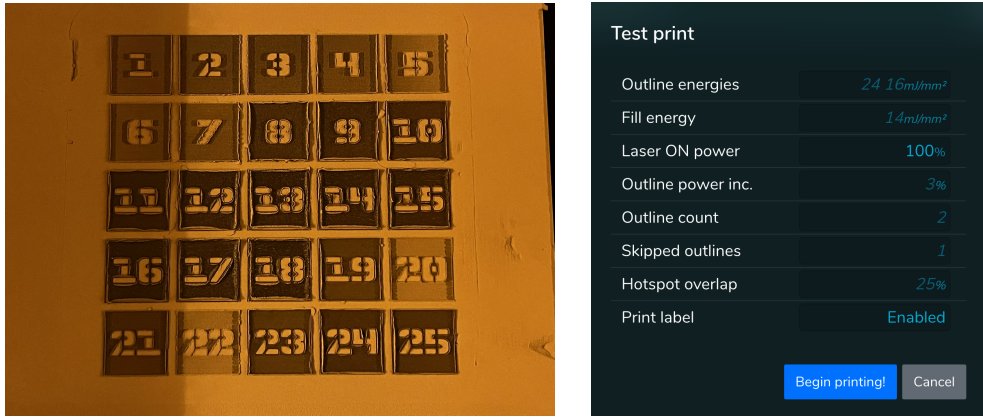
The primary purpose of the simulation tool is to approximate the local dimensions of the sintered material after the application of heat. Various methods such as Finite Element Analysis [129] and other numerical modeling techniques [120, 235] specific to the selective laser sintering process and materials will be used to gather general feasibility insight on process parameters before testing.

Parameter Testing Tool

The parameter testing tool is a feature specific to the Inova Mk1 such that when experimenting with new powders, a 5 x 5 grid of labeled patches (Figure 5.3a) can be printed on the surface of the print bed. This allows for the rapid testing of print parameters through patch specific configurations such as outline and fill energy densities (Figure 5.3b). In addition to executing patch prints, the tool will utilize the available sensors to extract quality information regarding each printed patch to determine which patch configuration to test next.

Print Profile Tool

The print profile tool sets the various build parameters for a specific material within the Inova Mk1 for future use. Notable parameters include surface and chamber temperatures, energy densities for the fill and contours, desired layer height, and recoater speed. This tool is expected to be executed once successful use of the parameter testing tool is completed.



(a) Printed Parameter Testing Patches

(b) Patch Configuration

Figure 5.3: 5 x 5 grid of patches (a) printed for testing PA12 GF powder, each with their own parameter configuration (b).

Build Monitoring Tool

The build monitoring tool will initialize the process for printing a specified part along with monitoring the process for potential anomalies. This tool will utilize the available sensors to observe each layer and terminate the build if failure is detected.

5.1.3 Evaluation

The agentic system will be evaluated on a range of polymers and polymer based composites with the mechanical properties tested to the ASTM 638-22 standard [61]. The setup will first determine the necessary build parameters needed to print a specific material and validate the print profile using the build monitoring tool. The evaluated prints will consist of standard additive manufacturing benchmarking samples along with tensile specimens.

5.2 Proposed Work: Continual Learning enabled Additive Manufacturing Large Language Model

In this work a continual learning pipeline will be developed to further integrate the collected results from agentic system into the large language model. Continual learning is the ability for a system to incrementally update and exploit available knowledge acquired throughout its lifetime [198, 232, 236]. This can be achieved through fine-tuning where the goal is to retain the existing capabilities and avoid catastrophic forgetting while retraining with new updated data [116, 198, 232]. This catastrophic forgetting issue can be mitigated through augmenting the original training data with the newly acquired data in a process called Continual Learning via Rehearsal (CLR) [198, 203]

With this, dataset curation is of upmost importance to ensure fidelity in the continual learning process. Background information regarding the expected outcomes of this specific selective laser sintering process will be curated from research articles and other technical specific to the polymer based SLS. Process parameter related outcomes such as the dimensions of the sintered volume will be sourced from simulations along with experimental literature finding if found. Lastly, successful iterations of the previously mentioned agentic system will be included as well in order to reinforce successful policy trajectories. Integration of this continual learning pipeline is expected to enable enhanced reasoning capabilities and this will be evaluated on the ratio of successful to incorrect policy trajectories of the agentic system with and without continual learning.

5.3 Timeline

My proposed milestones and timeline for completing the thesis are shown in Table 5.1.

Milestone	Timeline
Data collection and System Development	February - April 2026
Experimental Testing and Evaluation	April - June 2026
Thesis Writing	June - July 2026
Thesis Defense	July 2026

Table 5.1: Milestones and proposed timeline for completing the thesis.

BIBLIOGRAPHY

- [1] Claude 3.7 Sonnet and Claude Code, . URL <https://www.anthropic.com/news/clause-3-7-sonnet>.
- [2] FLOW-3D, . URL <https://www.flow3d.com/>.
- [3] Introducing Claude 4, . URL <https://www.anthropic.com/news/clause-4>.
- [4] LangChain, . URL <https://www.langchain.com>.
- [5] LlamaIndex - Build Knowledge Assistants over your Enterprise Data, . URL <https://www.llamaindex.ai/>.
- [6] MLX90640 IR Array Thermal Imaging Camera, 32×24 Pixels, 55° Field of View, I2C Interface, . URL https://www.waveshare.com/product/modules/sensors/mlx90640-d55-thermal-camera.htm?__SID=U.
- [7] Model context protocol (MCP) - OpenAI Agents SDK, . URL <https://openai.github.io/openai-agents-python/mcp/>.
- [8] Property Model Calculator, . URL <https://thermocalc.com/products/thermo-calc/property-model-calculator/>.
- [9] PyPI · The Python Package Index, . URL <https://pypi.org/>.
- [10] Subagents, . URL <https://docs.anthropic.com/en/docs/clause-code/sub-agents>.
- [11] T5, . URL https://huggingface.co/docs/transformers/v4.14.1/model_doc/t5.

- [12] Cross Plots for Alloy Design, June 2023. URL <https://thermocalc.com/blog/icme-workflows-using-cross-plots-to-visualize-the-tradeoff-of-properties-in-alloys>
- [13] google-t5/t5-small · Hugging Face, March 2024. URL <https://huggingface.co/google-t5/t5-small>.
- [14] meta-llama/Llama-3.2-1B · Hugging Face, December 2024. URL <https://huggingface.co/meta-llama/Llama-3.2-1B>.
- [15] modelcontextprotocol/python-sdk, August 2025. URL <https://github.com/modelcontextprotocol/python-sdk>. original-date: 2024-09-24T21:01:35Z.
- [16] OpenFOAM, June 2025. URL <https://www.openfoam.com/>.
- [17] Nesma T. Aboulkhair, Ian Maskery, Chris Tuck, Ian Ashcroft, and Nicola M. Everitt. On the formation of AlSi10Mg single tracks and layers in selective laser melting: Microstructure and nano-mechanical properties. *Journal of Materials Processing Technology*, 230:88–98, April 2016. ISSN 0924-0136. doi: 10.1016/j.jmatprotec.2015.11.016. URL <https://www.sciencedirect.com/science/article/pii/S0924013615302028>.
- [18] Ankur K. Agrawal, Behzad Rankouhi, and Dan J. Thoma. Predictive process mapping for laser powder bed fusion: A review of existing analytical solutions. *Current Opinion in Solid State and Materials Science*, 26(6):101024, December 2022. ISSN 1359-0286. doi: 10.1016/j.cossms.2022.101024. URL <https://www.sciencedirect.com/science/article/pii/S1359028622000444>.
- [19] N. Ahmed, I. Barsoum, G. Haidemenopoulos, and R. K. Abu Al-Rub. Process parameter selection and optimization of laser powder bed fusion for 316L stainless steel: A review. *Journal of Manufacturing Processes*, 75:415–434, March 2022. ISSN 1526-6125. doi: 10.1016/j.jmapro.2021.12.064. URL <https://www.sciencedirect.com/science/article/pii/S1526612522000160>.

- [20] Parand Akbari, Francis Ogoke, Ning-Yu Kao, Kazem Meidani, Chun-Yu Yeh, William Lee, and Amir Barati Farimani. MeltpoolNet: Melt pool characteristic prediction in Metal Additive Manufacturing using machine learning. *Additive Manufacturing*, 55:102817, July 2022. ISSN 2214-8604. doi: 10.1016/j.addma.2022.102817. URL <https://www.sciencedirect.com/science/article/pii/S2214860422002172>.
- [21] Parand Akbari, Masoud Zamani, and Amir Mostafaei. Machine learning prediction of mechanical properties in metal additive manufacturing. *Additive Manufacturing*, 91:104320, July 2024. ISSN 2214-8604. doi: 10.1016/j.addma.2024.104320. URL <https://www.sciencedirect.com/science/article/pii/S221486042400366X>.
- [22] Sawsan Alqahtani, Mir Tafseer Nayeem, Md Tahmid Rahman Laskar, Tasnim Mohiuddin, and M. Saiful Bari. Stop Taking Tokenizers for Granted: They Are Core Design Decisions in Large Language Models, January 2026. URL <http://arxiv.org/abs/2601.13260>. arXiv:2601.13260 [cs].
- [23] Anthropic. Introducing the Model Context Protocol, November 2024. URL <https://www.anthropic.com/news/model-context-protocol>.
- [24] Anthropic. Anthropic, 2025. URL <https://www.anthropic.com>.
- [25] Anurag Arnab, Mostafa Dehghani, Georg Heigold, Chen Sun, Mario Lučić, and Cordelia Schmid. ViViT: A Video Vision Transformer, November 2021. URL <http://arxiv.org/abs/2103.15691>. arXiv:2103.15691 [cs].
- [26] Mary Arnhart, Andrew Polonsky, Thomas Ivanoff, John Mitchell, Daryl Dagel, Jonathan Madison, and Bradley Jared. IN-SITU PYROMETRY AS AN INDICATORFOR DEFECTS IN ADDIVITELY MANUFACTURED METALS - REVISITED. In *Proposed for presentation at the TMS in Anaheim, California*. US DOE, February 2022. doi: 10.2172/2001881. URL <https://www.osti.gov/servlets/purl/2001881/>.

- [27] Dzmitry Bahdanau, Kyunghyun Cho, and Yoshua Bengio. Neural Machine Translation by Jointly Learning to Align and Translate, May 2016. URL <http://arxiv.org/abs/1409.0473>. arXiv:1409.0473 [cs, stat].
- [28] Bowen Baker, Joost Huizinga, Leo Gao, Zehao Dou, Melody Y. Guan, Aleksander Madry, Wojciech Zaremba, Jakub Pachocki, and David Farhi. Monitoring Reasoning Models for Misbehavior and the Risks of Promoting Obfuscation, March 2025. URL <http://arxiv.org/abs/2503.11926>. arXiv:2503.11926 [cs].
- [29] Suryanarayanan Balaji, Rishikesh Magar, Yayati Jadhav, and Amir Barati Farimani. GPT-MolBERTa: GPT Molecular Features Language Model for molecular property prediction, October 2023. URL <http://arxiv.org/abs/2310.03030>. arXiv:2310.03030 [physics].
- [30] Amit Bandyopadhyay and Bryan Heer. Additive manufacturing of multi-material structures. *Materials Science and Engineering: R: Reports*, 129:1–16, July 2018. ISSN 0927-796X. doi: 10.1016/j.mser.2018.04.001. URL <https://www.sciencedirect.com/science/article/pii/S0927796X18300780>.
- [31] Amit Bandyopadhyay, Kellen D. Traxel, Melanie Lang, Michael Juhasz, Noam Eliaz, and Susmita Bose. Alloy design via additive manufacturing: Advantages, challenges, applications and perspectives. *Materials Today*, 52:207–224, January 2022. ISSN 1369-7021. doi: 10.1016/j.mattod.2021.11.026. URL <https://www.sciencedirect.com/science/article/pii/S1369702121004314>.
- [32] Alison Bartsch and Amir Barati Farimani. LLM-Craft: Robotic Crafting of Elasto-Plastic Objects With Large Language Models. *IEEE Robotics and Automation Letters*, 10(10):10450–10457, October 2025. ISSN 2377-3766. doi: 10.1109/LRA.2025.3597835. URL <https://ieeexplore.ieee.org/document/11122568>.
- [33] Katharina Bartsch, Alexander Pettke, Artur Hübert, Julia Lakämper, and Fritz Lange. On the digital twin application and the role of artifi-

cial intelligence in additive manufacturing: a systematic review. *Journal of Physics: Materials*, 4(3):032005, April 2021. ISSN 2515-7639. doi: 10.1088/2515-7639/abf3cf. URL <https://dx.doi.org/10.1088/2515-7639/abf3cf>.

- [34] Ivanna Baturynska, Oleksandr Semeniuta, and Kristian Martinsen. Optimization of Process Parameters for Powder Bed Fusion Additive Manufacturing by Combination of Machine Learning and Finite Element Method: A Conceptual Framework. *Procedia CIRP*, 67:227–232, January 2018. ISSN 2212-8271. doi: 10.1016/j.procir.2017.12.204. URL <https://www.sciencedirect.com/science/article/pii/S2212827117311484>.
- [35] J. J. Beaman, D. L. Bourell, C. C. Seepersad, and D. Kovar. Additive Manufacturing Review: Early Past to Current Practice. *Journal of Manufacturing Science and Engineering*, 142(110812), September 2020. ISSN 1087-1357. doi: 10.1115/1.4048193. URL <https://doi.org/10.1115/1.4048193>.
- [36] Joseph J. Beaman and Carl R. Deckard. Selective laser sintering with assisted powder handling, July 1990. URL <https://patents.google.com/patent/US4938816A/en>.
- [37] Costanzo Bellini, Filippo Berto, Vittorio Di Cocco, Francesco Iacoviello, Larisa Patricia Mocanu, and Nima Razavi. Additive manufacturing processes for metals and effects of defects on mechanical strength: a review. *Procedia Structural Integrity*, 33:498–508, January 2021. ISSN 2452-3216. doi: 10.1016/j.prostr.2021.10.057. URL <https://www.sciencedirect.com/science/article/pii/S2452321621001529>.
- [38] Iz Beltagy, Kyle Lo, and Arman Cohan. SciBERT: A Pretrained Language Model for Scientific Text, September 2019. URL <http://arxiv.org/abs/1903.10676>. arXiv:1903.10676 [cs].

- [39] M. Berzins, T. H. C. Childs, K. W. Dalgarno, G. R. Ryder, and G. Stein. Densification and Distortion in Selective Laser Sintering of Polycarbonate. 1995. URL <http://hdl.handle.net/2152/68759>.
- [40] Jack Beuth, Jason Fox, Joy Gockel, Colt Montgomery, Rui Yang, Haipeng Qiao, Emre Can Soylemez, Pete Reesewatt, Amin Anvari, Sneha Narra, and Nathan Klingbeil. Process Mapping for Qualification Across Multiple Direct Metal Additive Manufacturing Processes. 2013. URL <https://hdl.handle.net/2152/88656>.
- [41] M. Biegler, B. Graf, and M. Rethmeier. In-situ distortions in LMD additive manufacturing walls can be measured with digital image correlation and predicted using numerical simulations. *Additive Manufacturing*, 20: 101–110, March 2018. ISSN 2214-8604. doi: 10.1016/j.addma.2017.12.007. URL <https://www.sciencedirect.com/science/article/pii/S2214860417305316>.
- [42] Michael Borish, Brian K. Post, Alex Roschli, Phillip C. Chesser, Lonnie J. Love, Katherine T. Gaul, Matthew Sallas, and Nikolaos Tsiamis. In-Situ Thermal Imaging for Single Layer Build Time Alteration in Large-Scale Polymer Additive Manufacturing. *Procedia Manufacturing*, 34:482–488, January 2019. ISSN 2351-9789. doi: 10.1016/j.promfg.2019.06.202. URL <https://www.sciencedirect.com/science/article/pii/S2351978919309321>.
- [43] Michael Borish, Brian K. Post, Alex Roschli, Phillip C. Chesser, and Lonnie J. Love. Real-Time Defect Correction in Large-Scale Polymer Additive Manufacturing via Thermal Imaging and Laser Profilometer. *Procedia Manufacturing*, 48:625–633, January 2020. ISSN 2351-9789. doi: 10.1016/j.promfg.2020.05.091. URL <https://www.sciencedirect.com/science/article/pii/S2351978920315432>.
- [44] Berkay Bostan, Shawn Hinnebusch, David Anderson, and Albert C. To. Accurate detection of local porosity in laser powder bed fusion through deep learning of physics-based in-situ infrared camera

signatures. *Additive Manufacturing*, 101:104701, March 2025. ISSN 2214-8604. doi: 10.1016/j.addma.2025.104701. URL <https://www.sciencedirect.com/science/article/pii/S221486042500065X>.

- [45] Mikaél' A. Bramson. *Infrared Radiation*. Springer US, Boston, MA, 1968. ISBN 978-1-4757-0913-1 978-1-4757-0911-7. doi: 10.1007/978-1-4757-0911-7. URL <http://link.springer.com/10.1007/978-1-4757-0911-7>.
- [46] Tom B. Brown, Benjamin Mann, Nick Ryder, Melanie Subbiah, Jared Kaplan, Prafulla Dhariwal, Arvind Neelakantan, Pranav Shyam, Girish Sastry, Amanda Askell, Sandhini Agarwal, Ariel Herbert-Voss, Gretchen Krueger, Tom Henighan, Rewon Child, Aditya Ramesh, Daniel M. Ziegler, Jeffrey Wu, Clemens Winter, Christopher Hesse, Mark Chen, Eric Sigler, Mateusz Litwin, Scott Gray, Benjamin Chess, Jack Clark, Christopher Berner, Sam McCandlish, Alec Radford, Ilya Sutskever, and Dario Amodei. Language Models are Few-Shot Learners, July 2020. URL <http://arxiv.org/abs/2005.14165>. arXiv:2005.14165 [cs].
- [47] Ömer Saltuk Böyükbaşı, Tarık Serindağ, Uğur Gürol, Ali Günen, and Gürel Çam. Improving oxidation resistance of wire arc additive manufactured Inconel 625 Ni-based superalloy by pack aluminizing. *CIRP Journal of Manufacturing Science and Technology*, 46:89–97, November 2023. ISSN 1755-5817. doi: 10.1016/j.cirpj.2023.07.011. URL <https://www.sciencedirect.com/science/article/pii/S1755581723001207>.
- [48] Stefania Cacace and Quirico Semeraro. On the Lack of fusion porosity in L-PBF processes. *Procedia CIRP*, 112:352–357, January 2022. ISSN 2212-8271. doi: 10.1016/j.procir.2022.09.008. URL <https://www.sciencedirect.com/science/article/pii/S2212827122011489>.
- [49] Carelyn E. Campbell, Ursula R. Kattner, and Zi-Kui Liu. The development of phase-based property data using the CALPHAD method and infrastructure needs. *Integrating Materials and Manufacturing Innovation*, 3(1):158–180, December 2014. ISSN 2193-9772. doi: 10.1186/2193-9772-3-12. URL <https://doi.org/10.1186/2193-9772-3-12>.

- [50] Arvind Car, Sai Sravan Yarlagadda, Alison Bartsch, Abraham George, and Amir Barati Farimani. PLATO: Planning with LLMs and Affordances for Tool Manipulation, September 2024. URL <http://arxiv.org/abs/2409.11580>. arXiv:2409.11580.
- [51] Achuth Chandrasekhar and Amir Barati Farimani. Automating MD simulations for Proteins using Large language Models: NAMD-Agent, July 2025. URL <http://arxiv.org/abs/2507.07887>. arXiv:2507.07887 [cs].
- [52] Achuth Chandrasekhar, Jonathan Chan, Francis Ogoke, Olabode Ajenifujah, and Amir Barati Farimani. AMGPT: A large language model for contextual querying in additive manufacturing. *Additive Manufacturing Letters*, 11:100232, December 2024. ISSN 2772-3690. doi: 10.1016/j.addlet.2024.100232. URL <https://www.sciencedirect.com/science/article/pii/S2772369024000409>.
- [53] Akshat Chaudhari, Janghoon Ock, and Amir Barati Farimani. Modular Large Language Model Agents for Multi-Task Computational Materials Science, May 2025. URL <https://chemrxiv.org/engage/chemrxiv/article-details/681239c150018ac7c5d5accf>.
- [54] Rajat Chaudhary, Paride Fabbri, Enrico Leoni, Francesca Mazzanti, Raziye Akbari, and Carlo Antonini. Additive manufacturing by digital light processing: a review. *Progress in Additive Manufacturing*, 8(2):331–351, April 2023. ISSN 2363-9520. doi: 10.1007/s40964-022-00336-0. URL <https://doi.org/10.1007/s40964-022-00336-0>.
- [55] Ze Chen, Changjun Han, Ming Gao, Sastry Yagnanna Kandukuri, and Kun Zhou. A review on qualification and certification for metal additive manufacturing. *Virtual and Physical Prototyping*, 17(2):382–405, April 2022. ISSN 1745-2759. doi: 10.1080/17452759.2021.2018938. URL <https://doi.org/10.1080/17452759.2021.2018938>. _eprint: <https://doi.org/10.1080/17452759.2021.2018938>.

- [56] Daniel R. Clymer, Jonathan Cagan, and Jack Beuth. Power–Velocity Process Design Charts for Powder Bed Additive Manufacturing. *Journal of Mechanical Design*, 139(100907), August 2017. ISSN 1050-0472. doi: 10.1115/1.4037302. URL <https://doi.org/10.1115/1.4037302>.
- [57] Sam Coeck, Manisha Bisht, Jan Plas, and Frederik Verbist. Prediction of lack of fusion porosity in selective laser melting based on melt pool monitoring data. *Additive Manufacturing*, 25:347–356, January 2019. ISSN 2214-8604. doi: 10.1016/j.addma.2018.11.015. URL <https://www.sciencedirect.com/science/article/pii/S2214860418306687>.
- [58] Peter S. Cook and David J. Ritchie. Determining the laser absorptivity of Ti-6Al-4V during laser powder bed fusion by calibrated melt pool simulation. *Optics & Laser Technology*, 162:109247, July 2023. ISSN 0030-3992. doi: 10.1016/j.optlastec.2023.109247. URL <https://www.sciencedirect.com/science/article/pii/S0030399223001408>.
- [59] Ross Cunningham, Andrea Nicolas, John Madsen, Eric Fodran, Elias Anagnostou, Michael D. Sangid, and Anthony D. Rollett. Analyzing the effects of powder and post-processing on porosity and properties of electron beam melted Ti-6Al-4V. *Materials Research Letters*, 5(7):516–525, November 2017. ISSN null. doi: 10.1080/21663831.2017.1340911. URL <https://doi.org/10.1080/21663831.2017.1340911>. eprint: <https://doi.org/10.1080/21663831.2017.1340911>.
- [60] Ross W. Cunningham. *Defect Formation Mechanisms in Powder-Bed Metal Additive Manufacturing*. Ph.D., Carnegie Mellon University, United States – Pennsylvania, 2018. URL <https://www.proquest.com/docview/2043940962/abstract/19C86E9053284D80PQ/1>.
- [61] D20 Committee. Test Method for Tensile Properties of Plastics. URL <http://www.astm.org/cgi-bin/resolver.cgi?D638-22>.
- [62] Daryl J. Dagel, Grant D. Grosssetete, Danny O. MacCallum, and Scott P. Korey. Four-color imaging pyrometer for mapping temperatures of laser-based metal processes. page 986103, Balti-

more, Maryland, United States, May 2016. doi: 10.1117/12.2223083. URL <http://proceedings.spiedigitallibrary.org/proceeding.aspx?doi=10.1117/12.2223083>.

- [63] James Damon, Stefan Dietrich, Florian Vollert, Jens Gibmeier, and Volker Schulze. Process dependent porosity and the influence of shot peening on porosity morphology regarding selective laser melted AlSi10Mg parts. *Additive Manufacturing*, 20:77–89, March 2018. ISSN 2214-8604. doi: 10.1016/j.addma.2018.01.001. URL <https://www.sciencedirect.com/science/article/pii/S2214860417304621>.
- [64] Wim Devesse, Dieter De Baere, Michaël Hinderdael, and Patrick Guillaume. Hardware-in-the-loop control of additive manufacturing processes using temperature feedback. *Journal of Laser Applications*, 28(2):022302, March 2016. ISSN 1042-346X. doi: 10.2351/1.4943911. URL <https://doi.org/10.2351/1.4943911>.
- [65] Jacob Devlin, Ming-Wei Chang, Kenton Lee, and Kristina Toutanova. BERT: Pre-training of Deep Bidirectional Transformers for Language Understanding, May 2019. URL <http://arxiv.org/abs/1810.04805>. arXiv:1810.04805.
- [66] Adrien Dolimont, Sébastien Michotte, Edouard Rivière-Lorphèvre, François Ducobu, Charlotte de Formanoir, Stéphane Godet, and Enrico Filippi. Effect of HIPping (Hot Isostatic Pressing) on electron beam melting Ti6Al4V parts after machining. *AIP Conference Proceedings*, 1769(1):190006, October 2016. ISSN 0094-243X. doi: 10.1063/1.4963616. URL <https://doi.org/10.1063/1.4963616>.
- [67] Sean P. Donegan, Edwin J. Schwalbach, and Michael A. Groeber. Multimodal Registration and Fusion of In Situ and Ex Situ Metal Additive Manufacturing Data. *JOM*, 73(11):3250–3262, November 2021. ISSN 1543-1851. doi: 10.1007/s11837-021-04883-9. URL <https://doi.org/10.1007/s11837-021-04883-9>.

- [68] Christo Dordlofva. A Design for Qualification Framework for the Development of Additive Manufacturing Components—A Case Study from the Space Industry. *Aerospace*, 7(3):25, March 2020. ISSN 2226-4310. doi: 10.3390/aerospace7030025. URL <https://www.mdpi.com/2226-4310/7/3/25>. Number: 3.
- [69] Alexey Dosovitskiy, Lucas Beyer, Alexander Kolesnikov, Dirk Weissenborn, Xiaohua Zhai, Thomas Unterthiner, Mostafa Dehghani, Matthias Minderer, Georg Heigold, Sylvain Gelly, Jakob Uszkoreit, and Neil Houlsby. An Image is Worth 16x16 Words: Transformers for Image Recognition at Scale, June 2021. URL <http://arxiv.org/abs/2010.11929> [cs].
- [70] Pavel Dyntera and Tomas Starek. sls4all/SLS4All.Compact, December 2025. URL <https://github.com/sls4all/SLS4All.Compact>. original-date: 2024-07-12T10:57:55Z.
- [71] T. W. Eagar and N. S. Tsai. Temperature fields produced by traveling distributed heat sources. *Weld. Res. Suppl.; (United States)*, December 1983. URL <https://www.osti.gov/biblio/5782268>. Institution: Massachusetts Institute of Technology, Cambridge Number: CONF-830485-.
- [72] P. Edwards, A. O’Conner, and M. Ramulu. Electron Beam Additive Manufacturing of Titanium Components: Properties and Performance. *Journal of Manufacturing Science and Engineering*, 135 (061016), November 2013. ISSN 1087-1357. doi: 10.1115/1.4025773. URL <https://doi.org/10.1115/1.4025773>.
- [73] Abul Ehtesham, Aditi Singh, Gaurav Kumar Gupta, and Saket Kumar. A survey of agent interoperability protocols: Model Context Protocol (MCP), Agent Communication Protocol (ACP), Agent-to-Agent Protocol (A2A), and Agent Network Protocol (ANP), May 2025. URL <http://arxiv.org/abs/2505.02279>. arXiv:2505.02279 [cs].

- [74] Jiang-kun Fan, Hong-ci Yang, Pei-zhe Zhang, Jia-yu Li, Zhan-jie Jing, Fu-long Chen, De-gui Liu, Bin Tang, Hong-chao Kou, and Jin-shan Li. Mechanism of high temperature oxidation of Inconel 625 superalloy with various solution and ageing heat treatment processes. *Transactions of Nonferrous Metals Society of China*, 34(11):3662–3676, November 2024. ISSN 1003-6326. doi: 10.1016/S1003-6326(24)66632-X. URL <https://www.sciencedirect.com/science/article/pii/S100363262466632X>.
- [75] Amir Barati Farimani. Large Language Models Monitor and Control Additive Manufacturing. AIChE, October 2024. URL <https://aiche.confex.com/aiche/2024/meetingapp.cgi/Paper/701277>.
- [76] Shaw C. Feng, Yan Lu, Albert T. Jones, and Zhuo Yang. Additive Manufacturing In Situ and Ex Situ Geometric Data Registration. *Journal of Computing and Information Science in Engineering*, 22(061003), May 2022. ISSN 1530-9827. doi: 10.1115/1.4054202. URL <https://doi.org/10.1115/1.4054202>.
- [77] Shuo Feng, Zhuoer Chen, Benjamin Bircher, Ze Ji, Lars Nyborg, and Samuel Bigot. Predicting laser powder bed fusion defects through in-process monitoring data and machine learning. *Materials & Design*, 222: 111115, October 2022. ISSN 0264-1275. doi: 10.1016/j.matdes.2022.111115. URL <https://www.sciencedirect.com/science/article/pii/S0264127522007377>.
- [78] Formlabs. Nylon 12 GF Powder, 2026. URL <https://formlabs.com/store/materials/nylon-12-gf-powder/>.
- [79] Philip Gage. A new algorithm for data compression. *The C Users Journal archive*, February 1994. URL <https://www.semanticscholar.org/paper/A-new-algorithm-for-data-compression-Gage/1aa9c0045f1fe8c79cce03c7c14ef4b4643a21f8>.
- [80] Aniruddha Gaikwad, Reza Yavari, Mohammad Montazeri, Kevin Cole, Linkan Bian, and Prahalada Rao. Toward the digital twin of addi-

tive manufacturing: Integrating thermal simulations, sensing, and analytics to detect process faults. *IISE Transactions*, 52(11):1204–1217, November 2020. ISSN 2472-5854. doi: 10.1080/24725854.2019.1701753. URL <https://doi.org/10.1080/24725854.2019.1701753>. eprint: <https://doi.org/10.1080/24725854.2019.1701753>.

- [81] Manuela Galati and Luca Iuliano. A literature review of powder-based electron beam melting focusing on numerical simulations. *Additive Manufacturing*, 19:1–20, January 2018. ISSN 2214-8604. doi: 10.1016/j.addma.2017.11.001. URL <https://www.sciencedirect.com/science/article/pii/S2214860417300635>.
- [82] Juan Luis Gastaldi, John Terilla, Luca Malagutti, Brian DuSell, Tim Vieira, and Ryan Cotterell. The Foundations of Tokenization: Statistical and Computational Concerns, April 2025. URL <http://arxiv.org/abs/2407.11606>. arXiv:2407.11606 [cs].
- [83] Abraham George and Amir Barati Farimani. LLM Trainer: Automated Robotic Data Generating via Demonstration Augmentation using LLMs, September 2025. URL <http://arxiv.org/abs/2509.20070>. arXiv:2509.20070 [cs].
- [84] Alireza Ghafarollahi and Markus J. Buehler. AtomAgents: Alloy design and discovery through physics-aware multi-modal multi-agent artificial intelligence, July 2024. URL <http://arxiv.org/abs/2407.10022>. arXiv:2407.10022 [cs].
- [85] Nahal Ghanadi, Kwangtae Son, Marco Alvarado, Seongun Yang, Hsin-Mei Kao, Chih-Hung Chang, Brian K. Paul, and Somayeh Pasebani. Effect of LPBF Processing Parameters on Inconel 718 Lattice Structures: Geometrical Characteristics, Surface Morphology, and Mechanical Properties. *Materials & Design*, 253:113864, May 2025. ISSN 0264-1275. doi: 10.1016/j.matdes.2025.113864. URL <https://www.sciencedirect.com/science/article/pii/S0264127525002849>.

- [86] Aïmen E. Gheribi and Patrice Chartrand. Application of the CALPHAD method to predict the thermal conductivity in dielectric and semiconductor crystals. *Calphad*, 39:70–79, December 2012. ISSN 0364-5916. doi: 10.1016/j.calphad.2012.06.002. URL <https://www.sciencedirect.com/science/article/pii/S0364591612000508>.
- [87] Joy Gockel and Jack Beuth. Understanding Ti-6Al-4V Microstructure Control in Additive Manufacturing via Process Maps. 2013. URL <https://hdl.handle.net/2152/88657>.
- [88] Siavash Golkar, Mariel Pettee, Michael Eickenberg, Alberto Bietti, Miles Cranmer, Geraud Krawezik, Francois Lanusse, Michael McCabe, Ruben Ohana, Liam Parker, Bruno Régaldo-Saint Blancard, Tiberiu Tesileanu, Kyunghyun Cho, and Shirley Ho. xVal: A Continuous Numerical Tokenization for Scientific Language Models, December 2024. URL <http://arxiv.org/abs/2310.02989>. arXiv:2310.02989 [stat].
- [89] J. A. Gonzalez, J. Mireles, S. W. Stafford, M. A. Perez, C. A. Terrazas, and R. B. Wicker. Characterization of Inconel 625 fabricated using powder-bed-based additive manufacturing technologies. *Journal of Materials Processing Technology*, 264:200–210, February 2019. ISSN 0924-0136. doi: 10.1016/j.jmatprotec.2018.08.031. URL <https://www.sciencedirect.com/science/article/pii/S092401361830373X>.
- [90] Jerard V. Gordon, Sneha P. Narra, Ross W. Cunningham, He Liu, Hangman Chen, Robert M. Suter, Jack L. Beuth, and Anthony D. Rollett. Defect structure process maps for laser powder bed fusion additive manufacturing. *Additive Manufacturing*, 36:101552, December 2020. ISSN 2214-8604. doi: 10.1016/j.addma.2020.101552. URL <https://www.sciencedirect.com/science/article/pii/S2214860420309246>.
- [91] Akhilesh Gotmare, Nitish Shirish Keskar, Caiming Xiong, and Richard Socher. A Closer Look at Deep Learning Heuristics: Learning rate restarts, Warmup and Distillation, October 2018. URL <http://arxiv.org/abs/1810.13243>. arXiv:1810.13243 [cs, stat].

- [92] M. Grasso, A. Remani, A. Dickins, B. M. Colosimo, and R. K. Leach. In-situ measurement and monitoring methods for metal powder bed fusion: an updated review. *Measurement Science and Technology*, 32(11):112001, July 2021. ISSN 0957-0233. doi: 10.1088/1361-6501/ac0b6b. URL <https://dx.doi.org/10.1088/1361-6501/ac0b6b>.
- [93] Aaron Grattafiori, Abhimanyu Dubey, Abhinav Jauhri, Abhinav Pandey, Abhishek Kadian, Ahmad Al-Dahle, Aiesha Letman, Akhil Mathur, Alan Schelten, Alex Vaughan, Amy Yang, Angela Fan, Anirudh Goyal, Anthony Hartshorn, Aobo Yang, Archi Mitra, Archie Sravankumar, Artem Korenev, Arthur Hinsvark, Arun Rao, Aston Zhang, Au-relien Rodriguez, Austen Gregerson, Ava Spataru, Baptiste Roziere, Bethany Biron, Binh Tang, Bobbie Chern, Charlotte Caucheteux, Chaya Nayak, Chloe Bi, Chris Marra, Chris McConnell, Christian Keller, Christophe Touret, Chunyang Wu, Corinne Wong, Cristian Canton Fer rer, Cyrus Nikolaidis, Damien Allonsius, Daniel Song, Danielle Pintz, Danny Livshits, Danny Wyatt, David Esiobu, Dhruv Choudhary, Dhruv Mahajan, Diego Garcia-Olano, Diego Perino, Dieuwke Hupkes, Egor Lakomkin, Ehab AlBadawy, Elina Lobanova, Emily Dinan, Eric Michael Smith, Filip Radenovic, Francisco Guzmán, Frank Zhang, Gabriel Synnaeve, Gabrielle Lee, Georgia Lewis Anderson, Govind Thattai, Graeme Nail, Gregoire Mialon, Guan Pang, Guillem Cucurell, Hailey Nguyen, Hannah Korevaar, Hu Xu, Hugo Touvron, Iliyan Zarov, Imanol Arrieta Ibarra, Isabel Kloumann, Ishan Misra, Ivan Evtimov, Jack Zhang, Jade Copet, Jaewon Lee, Jan Geffert, Jana Vranes, Jason Park, Jay Mahadeokar, Jeet Shah, Jelmer van der Linde, Jennifer Billock, Jenny Hong, Jenya Lee, Jeremy Fu, Jianfeng Chi, Jianyu Huang, Jiawen Liu, Jie Wang, Jiecao Yu, Joanna Bitton, Joe Spisak, Jongsoo Park, Joseph Rocca, Joshua Johnstun, Joshua Saxe, Junteng Jia, Kalyan Vasuden Alwala, Karthik Prasad, Kartikeya Upasani, Kate Plawiak, Ke Li, Kenneth Heafield, Kevin Stone, Khalid El-Arini, Krithika Iyer, Kshitiz Malik, Kuenley Chiu, Kunal Bhalla, Kushal Lakhota, Lauren Rantala-Yeary, Laurens van der Maaten, Lawrence Chen, Liang Tan,

Liz Jenkins, Louis Martin, Lovish Madaan, Lubo Malo, Lukas Blecher, Lukas Landzaat, Luke de Oliveira, Madeline Muzzi, Mahesh Pasupuleti, Mannat Singh, Manohar Paluri, Marcin Kardas, Maria Tsimpoukelli, Mathew Oldham, Mathieu Rita, Maya Pavlova, Melanie Kambadur, Mike Lewis, Min Si, Mitesh Kumar Singh, Mona Hassan, Naman Goyal, Narjes Torabi, Nikolay Bashlykov, Nikolay Bogoychev, Niladri Chatterji, Ning Zhang, Olivier Duchenne, Onur Çelebi, Patrick Alrassy, Pengchuan Zhang, Pengwei Li, Petar Vasic, Peter Weng, Prajjwal Bhargava, Pratik Dubal, Praveen Krishnan, Punit Singh Koura, Puxin Xu, Qing He, Qingxiao Dong, Ragavan Srinivasan, Raj Ganapathy, Ramon Calderer, Ricardo Silveira Cabral, Robert Stojnic, Roberta Raileanu, Rohan Maheswari, Rohit Girdhar, Rohit Patel, Romain Sauvestre, Ronnie Polidoro, Roshan Sumbaly, Ross Taylor, Ruan Silva, Rui Hou, Rui Wang, Saghar Hosseini, Sahana Chennabasappa, Sanjay Singh, Sean Bell, Seohyun Sonia Kim, Sergey Edunov, Shaoliang Nie, Sharan Narang, Sharath Rappothy, Sheng Shen, Shengye Wan, Shruti Bhosale, Shun Zhang, Simon Vandenhende, Soumya Batra, Spencer Whitman, Sten Sootla, Stephane Collot, Suchin Gururangan, Sydney Borodinsky, Tamar Herman, Tara Fowler, Tarek Sheasha, Thomas Georgiou, Thomas Scialom, Tobias Speckbacher, Todor Mihaylov, Tong Xiao, Ujjwal Karn, Vedanuj Goswami, Vibhor Gupta, Vignesh Ramanathan, Viktor Kerkez, Vincent Gonguet, Virginie Do, Vish Vogeti, Vítor Albiero, Vladan Petrovic, Weiwei Chu, Wenhan Xiong, Wenyin Fu, Whitney Meers, Xavier Martinet, Xiaodong Wang, Xiaofang Wang, Xiaoqing Ellen Tan, Xide Xia, Xinfeng Xie, Xuchao Jia, Xuewei Wang, Yaelle Goldschlag, Yashesh Gaur, Yasmine Babaei, Yi Wen, Yiwen Song, Yuchen Zhang, Yue Li, Yuning Mao, Zacharie Delpierre Coudert, Zheng Yan, Zhengxing Chen, Zoe Papakipos, Aaditya Singh, Aayushi Srivastava, Abha Jain, Adam Kelsey, Adam Shajnfeld, Adithya Gangidi, Adolfo Victoria, Ahuva Goldstand, Ajay Menon, Ajay Sharma, Alex Boesenber, Alexei Baevski, Allie Feinstein, Amanda Kallet, Amit Sangani, Amos Teo, Anam Yunus, Andrei Lupu, Andres Alvarado, Andrew Caples, Andrew Gu, Andrew Ho, Andrew Poulton, Andrew Ryan, Ankit Ramchandani, Annie Dong,

Annie Franco, Anuj Goyal, Aparajita Saraf, Arkabandhu Chowdhury, Ashley Gabriel, Ashwin Bharambe, Assaf Eisenman, Azadeh Yazdan, Beau James, Ben Maurer, Benjamin Leonhardi, Bernie Huang, Beth Loyd, Beto De Paola, Bhargavi Paranjape, Bing Liu, Bo Wu, Boyu Ni, Braden Hancock, Bram Wasti, Brandon Spence, Brani Stojkovic, Brian Gamido, Britt Montalvo, Carl Parker, Carly Burton, Catalina Mejia, Ce Liu, Changhan Wang, Changkyu Kim, Chao Zhou, Chester Hu, Ching-Hsiang Chu, Chris Cai, Chris Tindal, Christoph Feichtenhofer, Cynthia Gao, Damon Civin, Dana Beaty, Daniel Kreymer, Daniel Li, David Adkins, David Xu, Davide Testuggine, Delia David, Devi Parikh, Diana Liskovich, Didem Foss, Dingkang Wang, Duc Le, Dustin Holland, Edward Dowling, Eissa Jamil, Elaine Montgomery, Eleonora Presani, Emily Hahn, Emily Wood, Eric-Tuan Le, Erik Brinkman, Esteban Arcaute, Evan Dunbar, Evan Smothers, Fei Sun, Felix Kreuk, Feng Tian, Filippos Kokkinos, Firat Ozgenel, Francesco Caggioni, Frank Kanayet, Frank Seide, Gabriela Medina Florez, Gabriella Schwarz, Gada Badeer, Georgia Swee, Gil Halpern, Grant Herman, Grigory Sizov, Guangyi, Zhang, Guna Lakshminarayanan, Hakan Inan, Hamid Shojanazeri, Han Zou, Hannah Wang, Hanwen Zha, Haroun Habeeb, Harrison Rudolph, Helen Suk, Henry Aspegren, Hunter Goldman, Hongyuan Zhan, Ibrahim Damlaj, Igor Molybog, Igor Tufanov, Ilias Leontiadis, Irina-Elena Veliche, Itai Gat, Jake Weissman, James Geboski, James Kohli, Janice Lam, Japhet Asher, Jean-Baptiste Gaya, Jeff Marcus, Jeff Tang, Jennifer Chan, Jenny Zhen, Jeremy Reizenstein, Jeremy Teboul, Jessica Zhong, Jian Jin, Jingyi Yang, Joe Cummings, Jon Carvill, Jon Shepard, Jonathan McPhie, Jonathan Torres, Josh Ginsburg, Junjie Wang, Kai Wu, Kam Hou U, Karan Saxena, Kartikay Khandelwal, Katayoun Zand, Kathy Matosich, Kaushik Veeraraghavan, Kelly Michelena, Keqian Li, Kiran Jagadeesh, Kun Huang, Kunal Chawla, Kyle Huang, Lailin Chen, Lakshya Garg, Lavender A, Leandro Silva, Lee Bell, Lei Zhang, Liangpeng Guo, Licheng Yu, Liron Moshkovich, Luca Wehrstedt, Madian Khabsa, Manav Avalani, Manish Bhatt, Martynas Mankus, Matan Hasson, Matthew Lennie, Matthias

Reso, Maxim Groshev, Maxim Naumov, Maya Lathi, Meghan Keneally, Miao Liu, Michael L. Seltzer, Michal Valko, Michelle Restrepo, Mihir Patel, Mik Vyatskov, Mikayel Samvelyan, Mike Clark, Mike Macey, Mike Wang, Miquel Jubert Hermoso, Mo Metanat, Mohammad Rastegari, Munish Bansal, Nandhini Santhanam, Natascha Parks, Natasha White, Navyata Bawa, Nayan Singhal, Nick Egebo, Nicolas Usunier, Nikhil Mehta, Nikolay Pavlovich Laptev, Ning Dong, Norman Cheng, Oleg Chernoguz, Olivia Hart, Omkar Salpekar, Ozlem Kalinli, Parkin Kent, Parth Parekh, Paul Saab, Pavan Balaji, Pedro Rittner, Philip Bontrager, Pierre Roux, Piotr Dollar, Polina Zvyagina, Prashant Ratanchandani, Pritish Yuvraj, Qian Liang, Rachad Alao, Rachel Rodriguez, Rafi Ayub, Raghatham Murthy, Raghu Nayani, Rahul Mitra, Ran-gaprabhu Parthasarathy, Raymond Li, Rebekkah Hogan, Robin Battley, Rocky Wang, Russ Howes, Ruty Rinott, Sachin Mehta, Sachin Siby, Sai Jayesh Bondu, Samyak Datta, Sara Chugh, Sara Hunt, Sargun Dhillon, Sasha Sidorov, Satadru Pan, Saurabh Mahajan, Saurabh Verma, Seiji Yamamoto, Sharadh Ramaswamy, Shaun Lindsay, Shaun Lindsay, Sheng Feng, Shenghao Lin, Shengxin Cindy Zha, Shishir Patil, Shiva Shankar, Shuqiang Zhang, Shuqiang Zhang, Sinong Wang, Sneha Agarwal, Soji Sajuyigbe, Soumith Chintala, Stephanie Max, Stephen Chen, Steve Kehoe, Steve Satterfield, Sudarshan Govindaprasad, Sumit Gupta, Summer Deng, Sungmin Cho, Sunny Virk, Suraj Subramanian, Sy Choudhury, Sydney Goldman, Tal Remez, Tamar Glaser, Tamara Best, Thilo Koehler, Thomas Robinson, Tianhe Li, Tianjun Zhang, Tim Matthews, Timothy Chou, Tzook Shaked, Varun Vontimitta, Victoria Ajayi, Victoria Montanez, Vijai Mohan, Vinay Satish Kumar, Vishal Mangla, Vlad Ionescu, Vlad Poenaru, Vlad Tiberiu Mihailescu, Vladimir Ivanov, Wei Li, Wenchen Wang, Wenwen Jiang, Wes Bouaziz, Will Constable, Xiaocheng Tang, Xiaojian Wu, Xiaolan Wang, Xilun Wu, Xinbo Gao, Yaniv Kleinman, Yanjun Chen, Ye Hu, Ye Jia, Ye Qi, Yenda Li, Yilin Zhang, Ying Zhang, Yossi Adi, Youngjin Nam, Yu, Wang, Yu Zhao, Yuchen Hao, Yundi Qian, Yunlu Li, Yuzi He, Zach Rait, Zachary DeVito, Zef Rosnbrick, Zhaoduo Wen, Zhenyu Yang, Zhiwei

Zhao, and Zhiyu Ma. The Llama 3 Herd of Models, November 2024.
URL <http://arxiv.org/abs/2407.21783>. arXiv:2407.21783 [cs].

- [94] Dongdong Gu and Yifu Shen. Balling phenomena during direct laser sintering of multi-component Cu-based metal powder. *Journal of Alloys and Compounds*, 432(1):163–166, April 2007. ISSN 0925-8388. doi: 10.1016/j.jallcom.2006.06.011. URL <https://www.sciencedirect.com/science/article/pii/S0925838806007122>.
- [95] Harvey Hack, Richard Link, Erik Knudsen, Brad Baker, and Scott Olig. Mechanical properties of additive manufactured nickel alloy 625. *Additive Manufacturing*, 14:105–115, March 2017. ISSN 2214-8604. doi: 10.1016/j.addma.2017.02.004. URL <https://www.sciencedirect.com/science/article/pii/S2214860416302408>.
- [96] James Haley, Clay Leach, Brian Jordan, Ryan Dehoff, and Vincent Paquit. In-situ digital image correlation and thermal monitoring in directed energy deposition additive manufacturing. *Optics Express*, 29(7):9927–9941, March 2021. ISSN 1094-4087. doi: 10.1364/OE.416659. URL <https://opg.optica.org/oe/abstract.cfm?uri=oe-29-7-9927>.
- [97] Hamsa Buvaraghan and Derek Egan. MCP Toolbox for Databases (formerly Gen AI Toolbox for Databases) now supports Model Context Protocol (MCP), April 2025. URL <https://cloud.google.com/blog/products/ai-machine-learning/mcp-toolbox-for-databases-now-supports-model-context-protocol>.
- [98] Xing He, Decheng Kong, Yiqi Zhou, Li Wang, Xiaoqing Ni, Liang Zhang, Wenheng Wu, Ruixue Li, Xiaogang Li, and Chaofang Dong. Powder recycling effects on porosity development and mechanical properties of Hastelloy X alloy during laser powder bed fusion process. *Additive Manufacturing*, 55:102840, July 2022. ISSN 2214-8604. doi: 10.1016/j.addma.2022.102840. URL <https://www.sciencedirect.com/science/article/pii/S2214860422002391>.

- [99] Hamidreza Hekmatjou, Zhi Zeng, Jiajia Shen, J. P. Oliveira, and Homam Naffakh-Moosavy. A Comparative Study of Analytical Rosen-thal, Finite Element, and Experimental Approaches in Laser Welding of AA5456 Alloy. *Metals*, 10(4):436, April 2020. ISSN 2075-4701. doi: 10.3390/met10040436. URL <https://www.mdpi.com/2075-4701/10/4/436>. Number: 4.
- [100] AmirPouya Hemmasian, Francis Ogoke, Parand Akbari, Jonathan Malen, Jack Beuth, and Amir Barati Farimani. Surrogate modeling of melt pool temperature field using deep learning. *Additive Manufacturing Letters*, 5:100123, April 2023. ISSN 2772-3690. doi: 10.1016/j.addlet.2023.100123. URL <https://www.sciencedirect.com/science/article/pii/S277236902300004X>.
- [101] J. Hesselvig, R. T. Nygaard, M. K. Budzik, and M. Sandberg. Efficient continuum-based modelling and analysis of polymer SLS: Insights into particle sintering and densification in straight and corner scanning passes. *Additive Manufacturing*, 109:104828, July 2025. ISSN 2214-8604. doi: 10.1016/j.addma.2025.104828. URL <https://www.sciencedirect.com/science/article/pii/S2214860425001927>.
- [102] H. C. H Ho, I Gibson, and W. L Cheung. Effects of energy density on morphology and properties of selective laser sintered polycarbonate. *Journal of Materials Processing Technology*, 89-90:204–210, May 1999. ISSN 0924-0136. doi: 10.1016/S0924-0136(99)00007-2. URL <https://www.sciencedirect.com/science/article/pii/S0924013699000072>.
- [103] Joseph Hofman and Katrin Wudy. In situ process monitoring in laser-based powder bed fusion of polyamide 12 using thermal imaging. *The International Journal of Advanced Manufacturing Technology*, 122(9):4127–4138, October 2022. ISSN 1433-3015. doi: 10.1007/s00170-022-10169-4. URL <https://doi.org/10.1007/s00170-022-10169-4>.

- [104] P. Honarmandi, R. Seede, L. Xue, D. Shoukr, P. Morcos, B. Zhang, C. Zhang, A. Elwany, I. Karaman, and R. Arroyave. A rigorous test and improvement of the Eagar-Tsai model for melt pool characteristics in laser powder bed fusion additive manufacturing. *Additive Manufacturing*, 47:102300, November 2021. ISSN 2214-8604. doi: 10.1016/j.addma.2021.102300. URL <https://www.sciencedirect.com/science/article/pii/S2214860421004590>.
- [105] Hiroshi Honda and Makoto Watanabe. Measurement of Laser Absorptivity of Inconel Powders with Additive Manufacturing Machine. *MATERIALS TRANSACTIONS*, 66(1):107–112, January 2025. ISSN 1345-9678, 1347-5320. doi: 10.2320/matertrans.MT-M2024124. URL https://www.jstage.jst.go.jp/article/matertrans/66/1/66_MT-M2024124/_article.
- [106] Xinyi Hou, Yanjie Zhao, Shenao Wang, and Haoyu Wang. Model Context Protocol (MCP): Landscape, Security Threats, and Future Research Directions, April 2025. URL <http://arxiv.org/abs/2503.23278> [cs]. arXiv:2503.23278 [cs].
- [107] Guoliang Huang, Huan Chen, Zhaodandan Ma, Ruiqian Zhang, Jingyuan Pei, Ziyi Lie, Peinan Du, Xiaoqiang Peng, Ying Liu, and Ke Huang. Microstructure and mechanical properties of stainless steel additively manufactured via laser powder bed fusion in high-dense process parameter window. *Materials Science and Engineering: A*, 928:148033, April 2025. ISSN 0921-5093. doi: 10.1016/j.msea.2025.148033. URL <https://www.sciencedirect.com/science/article/pii/S0921509325002515>.
- [108] Yuze Huang, Tristan G. Fleming, Samuel J. Clark, Sebastian Marussi, Kamel Fezzaa, Jeyan Thiyagalingam, Chu Lun Alex Leung, and Peter D. Lee. Keyhole fluctuation and pore formation mechanisms during laser powder bed fusion additive manufacturing. *Nature Communications*, 13(1):1170, March 2022. ISSN 2041-1723. doi: 10.

- 1038/s41467-022-28694-x. URL <https://www.nature.com/articles/s41467-022-28694-x>.
- [109] Charles W. Hull. Apparatus for production of three-dimensional objects by stereolithography, March 1986. URL <https://patents.google.com/patent/US4575330A/en>.
 - [110] Maurizio Iebba, Antonello Astarita, Daniela Mistretta, Ivano Colonna, Mariacira Liberini, Fabio Scherillo, Carmine Pirozzi, Rosario Borrelli, Stefania Franchitti, and Antonino Squillace. Influence of Powder Characteristics on Formation of Porosity in Additive Manufacturing of Ti-6Al-4V Components. *Journal of Materials Engineering and Performance*, 26(8):4138–4147, August 2017. ISSN 1544-1024. doi: 10.1007/s11665-017-2796-2. URL <https://doi.org/10.1007/s11665-017-2796-2>.
 - [111] Katsushi Ikeuchi, editor. *Computer Vision: A Reference Guide*. Springer International Publishing, Cham, 2021. ISBN 978-3-030-63415-5 978-3-030-63416-2. doi: 10.1007/978-3-030-63416-2. URL <https://link.springer.com/10.1007/978-3-030-63416-2>.
 - [112] Shahriar Imani Shahabad, Gholamreza Karimi, and Ehsan Toyserkani. An Extended Rosenthal’s Model for Laser Powder-Bed Fusion Additive Manufacturing: Energy Auditing of Thermal Boundary Conditions. *Lasers in Manufacturing and Materials Processing*, 8(3):288–311, September 2021. ISSN 2196-7237. doi: 10.1007/s40516-021-00148-0. URL <https://doi.org/10.1007/s40516-021-00148-0>.
 - [113] Yayati Jadhav and Amir Barati Farimani. Large Language Model Agent as a Mechanical Designer, May 2024. URL <http://arxiv.org/abs/2404.17525>. arXiv:2404.17525 [cs].
 - [114] Yayati Jadhav, Joseph Berthel, Chunshan Hu, Rahul Panat, Jack Beuth, and Amir Barati Farimani. StressD: 2D Stress estimation using denoising diffusion model. *Computer Methods in Applied Mechanics and Engineering*, 416:116343, November 2023. ISSN 0045-7825. doi:

10.1016/j.cma.2023.116343. URL <https://www.sciencedirect.com/science/article/pii/S004578252300467X>.

- [115] Yayati Jadhav, Peter Pak, and Amir Barati Farimani. LLM-3D print: Large language models to monitor and control 3D printing. *Additive Manufacturing*, page 105027, November 2025. ISSN 2214-8604. doi: 10.1016/j.addma.2025.105027. URL <https://www.sciencedirect.com/science/article/pii/S2214860425003926>.
- [116] Joel Jang, Seonghyeon Ye, Sohee Yang, Joongbo Shin, Janghoon Han, Gyeonghun Kim, Stanley Jungkyu Choi, and Minjoon Seo. Towards Continual Knowledge Learning of Language Models. *ArXiv*, October 2021. URL <https://www.semanticscholar.org/paper/Towards-Continual-Knowledge-Learning-of-Language-Jang-Ye/ce828f9986b196308a3e40b1de58af1e8e68d728>.
- [117] Elias Jelis, Matthew Clemente, Stacey Kerwien, Nuggehalli M. Ravindra, and Michael R. Hespos. Metallurgical and Mechanical Evaluation of 4340 Steel Produced by Direct Metal Laser Sintering. *JOM*, 67(3): 582–589, March 2015. ISSN 1543-1851. doi: 10.1007/s11837-014-1273-8. URL <https://doi.org/10.1007/s11837-014-1273-8>.
- [118] Meng Jiang, Xi Chen, Yanbin Chen, and Wang Tao. Mitigation of porosity defects in fiber laser welding under low vacuum. *Journal of Materials Processing Technology*, 276:116385, February 2020. ISSN 0924-0136. doi: 10.1016/j.jmatprotec.2019.116385. URL <https://www.sciencedirect.com/science/article/pii/S0924013619303577>.
- [119] Chen Jiao, Deqiao Xie, Zhijing He, Huixin Liang, Lida Shen, Youwen Yang, Zongjun Tian, Guofeng Wu, and Changjiang Wang. Additive manufacturing of Bio-inspired ceramic bone Scaffolds: Structural Design, mechanical properties and biocompatibility. *Materials & Design*, 217:110610, May 2022. ISSN 0264-1275. doi: 10.1016/j.matdes.2022.110610. URL <https://www.sciencedirect.com/science/article/pii/S0264127522002313>.

- [120] M. Kandis and T. L. Bergman. A Simulation-Based Correlation of the Density and Thermal Conductivity of Objects Produced by Laser Sintering of Polymer Powders. *Journal of Manufacturing Science and Engineering*, 122(3):439–444, November 1999. ISSN 1087-1357. doi: 10.1115/1.1286558. URL <https://doi.org/10.1115/1.1286558>.
- [121] Larry Kaufman and Harold Bernstein. *Computer Calculation of Phase Diagrams with Special Reference to Refractory Metals*. Academic Press, 1970. ISBN 978-0-12-402050-4.
- [122] Mevlüt Yunus Kayacan and Nihat Yılmaz. An investigation on the measurement of instantaneous temperatures in laser assisted additive manufacturing by thermal imagers. *Measurement*, 160:107825, August 2020. ISSN 0263-2241. doi: 10.1016/j.measurement.2020.107825. URL <https://www.sciencedirect.com/science/article/pii/S0263224120303638>.
- [123] KevinOConnor. Klipper3d/klipper, February 2026. URL <https://github.com/Klipper3d/klipper>. original-date: 2016-05-25T15:42:06Z.
- [124] M. W Khaing, J. Y. H Fuh, and L Lu. Direct metal laser sintering for rapid tooling: processing and characterisation of EOS parts. *Journal of Materials Processing Technology*, 113(1):269–272, June 2001. ISSN 0924-0136. doi: 10.1016/S0924-0136(01)00584-2. URL <https://www.sciencedirect.com/science/article/pii/S0924013601005842>.
- [125] Hyungson Ki, Jyoti Mazumder, and Pravansu S. Mohanty. Modeling of laser keyhole welding: Part I. mathematical modeling, numerical methodology, role of recoil pressure, multiple reflections, and free surface evolution. *Metallurgical and Materials Transactions A*, 33(6):1817–1830, June 2002. ISSN 1543-1940. doi: 10.1007/s11661-002-0190-6. URL <https://doi.org/10.1007/s11661-002-0190-6>.
- [126] G. L. Knapp, T. Mukherjee, J. S. Zuback, H. L. Wei, T. A. Palmer, A. De, and T. DebRoy. Building blocks for a digital twin of addi-

- tive manufacturing. *Acta Materialia*, 135:390–399, August 2017. ISSN 1359-6454. doi: 10.1016/j.actamat.2017.06.039. URL <https://www.sciencedirect.com/science/article/pii/S1359645417305141>.
- [127] Takeshi Kojima, Shixiang Shane Gu, Machel Reid, Yutaka Matsuo, and Yusuke Iwasawa. Large Language Models are Zero-Shot Reasoners, January 2023. URL <http://arxiv.org/abs/2205.11916>. arXiv:2205.11916 [cs].
- [128] Y. Kok, X. P. Tan, P. Wang, M. L. S. Nai, N. H. Loh, E. Liu, and S. B. Tor. Anisotropy and heterogeneity of microstructure and mechanical properties in metal additive manufacturing: A critical review. *Materials & Design*, 139:565–586, February 2018. ISSN 0264-1275. doi: 10.1016/j.matdes.2017.11.021. URL <https://www.sciencedirect.com/science/article/pii/S0264127517310493>.
- [129] S. Kolossov, E. Boillat, R. Glardon, P. Fischer, and M. Locher. 3D FE simulation for temperature evolution in the selective laser sintering process. *International Journal of Machine Tools and Manufacture*, 44(2):117–123, February 2004. ISSN 0890-6955. doi: 10.1016/j.ijmachtools.2003.10.019. URL <https://www.sciencedirect.com/science/article/pii/S089069550300289X>.
- [130] Alex Krizhevsky, Ilya Sutskever, and Geoffrey E. Hinton. ImageNet classification with deep convolutional neural networks. *Communications of the ACM*, 60(6):84–90, May 2017. ISSN 0001-0782, 1557-7317. doi: 10.1145/3065386. URL <https://dl.acm.org/doi/10.1145/3065386>.
- [131] J. P. Kruth, M. C. Leu, and T. Nakagawa. Progress in Additive Manufacturing and Rapid Prototyping. *CIRP Annals*, 47(2):525–540, January 1998. ISSN 0007-8506. doi: 10.1016/S0007-8506(07)63240-5. URL <https://www.sciencedirect.com/science/article/pii/S0007850607632405>.
- [132] Sanjay Kumar. Selective laser sintering: A qualitative and objective approach. *JOM*, 55(10):43–47, October 2003. ISSN 1543-1851.

doi: 10.1007/s11837-003-0175-y. URL <https://doi.org/10.1007/s11837-003-0175-y>.

- [133] Zhenzhong Lan, Mingda Chen, Sebastian Goodman, Kevin Gimpel, Piyush Sharma, and Radu Soricut. ALBERT: A Lite BERT for Self-supervised Learning of Language Representations, February 2020. URL <http://arxiv.org/abs/1909.11942>. arXiv:1909.11942 [cs].
- [134] Erlei Li, Haopeng Shen, Lin Wang, Geoff Wang, and Zongyan Zhou. Laser shape variation influence on melt pool dynamics and solidification microstructure in laser powder bed fusion. *Additive Manufacturing Letters*, 6:100141, July 2023. ISSN 2772-3690. doi: 10.1016/j.addlet.2023.100141. URL <https://www.sciencedirect.com/science/article/pii/S2772369023000221>.
- [135] Zhiwen Li, Zhifen Zhang, Shuai Zhang, Jie Wang, Zijian Bai, Zhengyao Du, Ke Huang, Qi Zhang, Yu Su, Guangrui Wen, and Xuefeng Chen. In-situ monitoring in laser powder bed fusion based on acoustic signal time-frequency synchrosqueezing transform and multi-scale spatially interactive fusion convolutional neural network. *Journal of Manufacturing Processes*, 126:471–486, September 2024. ISSN 1526-6125. doi: 10.1016/j.jmapro.2024.07.068. URL <https://www.sciencedirect.com/science/article/pii/S1526612524007229>.
- [136] Zijie Li, Dule Shu, and Amir Barati Farimani. Scalable transformer for pde surrogate modeling. *Advances in Neural Information Processing Systems*, 36, 2024. URL https://proceedings.neurips.cc/paper_files/paper/2023/hash/590daf74f99ee85df3d8c007df9c8187-Abstract-Conference.html.
- [137] Viktor Lindström, Giandomenico Lupo, Jian Yang, Vladyslav Turlo, and Christian Leinenbach. A simple scaling model for balling defect formation during laser powder bed fusion. *Additive Manufacturing*, 63:103431, February 2023. ISSN 2214-8604. doi: 10.1016/j.addma.2023.103431. URL <https://www.sciencedirect.com/science/article/pii/S2214860423000441>.

- [138] Yinhan Liu, Myle Ott, Naman Goyal, Jingfei Du, Mandar Joshi, Danqi Chen, Omer Levy, Mike Lewis, Luke Zettlemoyer, and Veselin Stoyanov. RoBERTa: A Robustly Optimized BERT Pretraining Approach, July 2019. URL <http://arxiv.org/abs/1907.11692>. arXiv:1907.11692.
- [139] Jonathan Long, Evan Shelhamer, and Trevor Darrell. Fully Convolutional Networks for Semantic Segmentation, March 2015. URL <http://arxiv.org/abs/1411.4038>. arXiv:1411.4038 [cs].
- [140] Cooper Lorsung and Amir Barati Farimani. Explain Like I'm Five: Using LLMs to Improve PDE Surrogate Models with Text, November 2024. URL <http://arxiv.org/abs/2410.01137>. arXiv:2410.01137.
- [141] Pan Lu, Zhang Cheng-Lin, Wang Liang, Liu Tong, and Li Xiao-Cheng. Research on mechanical properties and microstructure by selective laser melting of 316L stainless steel. *Materials Research Express*, 6(12):1265h7, January 2020. ISSN 2053-1591. doi: 10.1088/2053-1591/ab6b67. URL <https://doi.org/10.1088/2053-1591/ab6b67>.
- [142] S. L. Lu, H. P. Tang, Y. P. Ning, N. Liu, D. H. StJohn, and M. Qian. Microstructure and Mechanical Properties of Long Ti-6Al-4V Rods Additively Manufactured by Selective Electron Beam Melting Out of a Deep Powder Bed and the Effect of Subsequent Hot Isostatic Pressing. *Metallurgical and Materials Transactions A*, 46(9):3824–3834, September 2015. ISSN 1543-1940. doi: 10.1007/s11661-015-2976-3. URL <https://doi.org/10.1007/s11661-015-2976-3>.
- [143] Lukas Löber, Frank Peter Schimansky, Uta Kühn, Florian Pyczak, and Jürgen Eckert. Selective laser melting of a beta-solidifying TNM-B1 titanium aluminide alloy. *Journal of Materials Processing Technology*, 214(9):1852–1860, September 2014. ISSN 0924-0136. doi: 10.1016/j.jmatprotec.2014.04.002. URL <https://www.sciencedirect.com/science/article/pii/S0924013614001277>.
- [144] Diego Manfredi, Flaviana Calignano, Manickavasagam Krishnan, Ricardo Canali, Elisa Paola Ambrosio, and Eleonora Atzeni. From Pow-

- ders to Dense Metal Parts: Characterization of a Commercial AlSiMg Alloy Processed through Direct Metal Laser Sintering. *Materials*, 6(3): 856–869, March 2013. ISSN 1996-1944. doi: 10.3390/ma6030856. URL <https://www.mdpi.com/1996-1944/6/3/856>.
- [145] C. P. Martendal, P. D. B. Esteves, C. Lüthi, L. Deillon, M. Afrasiabi, and M. Bambach. Mitigating defects at copper-steel interfaces via a lack of fusion-informed power increment strategy in multi-material laser powder bed fusion. *Materials & Design*, 258:114597, October 2025. ISSN 0264-1275. doi: 10.1016/j.matdes.2025.114597. URL <https://www.sciencedirect.com/science/article/pii/S0264127525010172>.
- [146] Ronan McCann, Muhannad A. Obeidi, Cian Hughes, Eanna McCarthy, Darragh S. Egan, Rajani K. Vijayaraghavan, Ajey M. Joshi, Victor Acinas Garzon, Denis P. Dowling, Patrick J. McNally, and Dermot Brabazon. In-situ sensing, process monitoring and machine control in Laser Powder Bed Fusion: A review. *Additive Manufacturing*, 45: 102058, September 2021. ISSN 2214-8604. doi: 10.1016/j.addma.2021.102058. URL <https://www.sciencedirect.com/science/article/pii/S2214860421002232>.
- [147] Nandana Menon, Sudeeptha Mondal, and Amrita Basak. Multi-Fidelity Surrogate-Based Process Mapping with Uncertainty Quantification in Laser Directed Energy Deposition. *Materials*, 15(8):2902, January 2022. ISSN 1996-1944. doi: 10.3390/ma15082902. URL <https://www.mdpi.com/1996-1944/15/8/2902>. Number: 8.
- [148] Chad Merrill, Akshay Raman, Abraham George, and Amir Barati Farimani. LLM-drone: aerial additive manufacturing with drones planned using large language models. *Construction Robotics*, 9(2):20, August 2025. ISSN 2509-8780. doi: 10.1007/s41693-025-00162-0. URL <https://doi.org/10.1007/s41693-025-00162-0>.
- [149] Raya Mertens, Stijn Clijsters, Karolien Kempen, and Jean-Pierre Kruth. Optimization of Scan Strategies in Selective Laser Melting of Aluminum

Parts With Downfacing Areas. *Journal of Manufacturing Science and Engineering*, 136(061012), October 2014. ISSN 1087-1357. doi: 10.1115/1.4028620. URL <https://doi.org/10.1115/1.4028620>.

- [150] KC Mills. Recommended Values of Thermophysical Properties for Selected Commercial Alloys, 2002. URL <http://www.sciencedirect.com:5070/book/monograph/9781855735699/recommended-values-of-thermophysical-properties-for-selected-commercial-alloys>. ISBN: 9781855735699.
- [151] Shervin Minaee, Tomas Mikolov, Narjes Nikzad, Meysam Chenaghlu, Richard Socher, Xavier Amatriain, and Jianfeng Gao. Large Language Models: A Survey, February 2024. URL <http://arxiv.org/abs/2402.06196>. arXiv:2402.06196.
- [152] Justin P. Miner, Austin Ngo, Christian Gobert, Tharun Reddy, John J. Lewandowski, Anthony D. Rollett, Jack Beuth, and Sneha Prabha Narra. Impact of melt pool geometry variability on lack-of-fusion porosity and fatigue life in powder bed fusion-laser beam Ti–6Al–4V. *Additive Manufacturing*, 95:104506, September 2024. ISSN 2214-8604. doi: 10.1016/j.addma.2024.104506. URL <https://www.sciencedirect.com/science/article/pii/S2214860424005529>.
- [153] John A. Mitchell, Thomas A. Ivanoff, Daryl Dagel, Jonathan D. Madison, and Bradley Jared. Linking pyrometry to porosity in additively manufactured metals. *Additive Manufacturing*, 31:100946, January 2020. ISSN 2214-8604. doi: 10.1016/j.addma.2019.100946. URL <https://www.sciencedirect.com/science/article/pii/S2214860419309868>.
- [154] Yuichiro Miyata, Masayuki Okugawa, Yuichiro Koizumi, and Takayoshi Nakano. Inverse Columnar-Equiaxed Transition (CET) in 304 and 316L Stainless Steels Melt by Electron Beam for Additive Manufacturing (AM). *Crystals*, 11:856, July 2021. doi: 10.3390/crust11080856.

- [155] Alexander J. Myers, Guadalupe Quirarte, Jack L. Beuth, and Jonathan A. Malen. Two-color thermal imaging of the melt pool in powder-blown laser-directed energy deposition. *Additive Manufacturing*, 78:103855, 2023. URL <https://www.sciencedirect.com/science/article/pii/S2214860423004682>.
- [156] Alexander J. Myers, Guadalupe Quirarte, Francis Ogoke, Brandon M. Lane, Syed Zia Uddin, Amir Barati Farimani, Jack L. Beuth, and Jonathan A. Malen. High-resolution melt pool thermal imaging for metals additive manufacturing using the two-color method with a color camera. *Additive Manufacturing*, 73:103663, 2023. URL <https://www.sciencedirect.com/science/article/pii/S2214860423002762>.
- [157] Reiichiro Nakano, Jacob Hilton, Suchir Balaji, Jeff Wu, Long Ouyang, Christina Kim, Christopher Hesse, Shantanu Jain, Vineet Kosaraju, William Saunders, Xu Jiang, Karl Cobbe, Tyna Eloundou, Gretchen Krueger, Kevin Button, Matthew Knight, Benjamin Chess, and John Schulman. WebGPT: Browser-assisted question-answering with human feedback, June 2022. URL <http://arxiv.org/abs/2112.09332>. arXiv:2112.09332 [cs].
- [158] G. K. L. Ng, A. E. W. Jarfors, G. Bi, and H. Y. Zheng. Porosity formation and gas bubble retention in laser metal deposition. *Applied Physics A*, 97(3):641–649, November 2009. ISSN 1432-0630. doi: 10.1007/s00339-009-5266-3. URL <https://doi.org/10.1007/s00339-009-5266-3>.
- [159] H. J. Niu and I. T. H. Chang. Selective laser sintering of gas atomized M2 high speed steel powder. *Journal of Materials Science*, 35(1):31–38, January 2000. ISSN 1573-4803. doi: 10.1023/A:1004720011671. URL <https://doi.org/10.1023/A:1004720011671>.
- [160] G. Nordet, C. Gorny, Y. Mayi, J. Daligault, M. Dal, A. Efferelli, E. Blanchet, F. Coste, and P. Peyre. Absorptivity measurements during laser powder bed fusion of pure copper with a 1 kW cw green laser. *Optics & Laser Technology*, 147:107612, March 2022. ISSN 0030-3992. doi:

10.1016/j.optlastec.2021.107612. URL <https://www.sciencedirect.com/science/article/pii/S0030399221007003>.

- [161] Janghoon Ock, Chakradhar Guntuboina, and Amir Barati Farimani. Catalyst Energy Prediction with CatBERTa: Unveiling Feature Exploration Strategies through Large Language Models. *ACS Catalysis*, 13(24):16032–16044, December 2023. doi: 10.1021/acscatal.3c04956. URL <https://doi.org/10.1021/acscatal.3c04956>.
- [162] Janghoon Ock, Srivathsan Badrinarayanan, Rishikesh Magar, Akshay Antony, and Amir Barati Farimani. Multimodal language and graph learning of adsorption configuration in catalysis. *Nature Machine Intelligence*, pages 1–11, November 2024. ISSN 2522-5839. doi: 10.1038/s42256-024-00930-7. URL <https://www.nature.com/articles/s42256-024-00930-7>.
- [163] Janghoon Ock, Tirtha Vinchurkar, Yayati Jadhav, and Amir Barati Farimani. Adsorb-Agent: Autonomous Identification of Stable Adsorption Configurations via Large Language Model Agent, December 2024. URL <http://arxiv.org/abs/2410.16658>. arXiv:2410.16658 [cs].
- [164] Janghoon Ock, Radheesh Sharma Meda, Srivathsan Badrinarayanan, Neha S. Aluru, Achuth Chandrasekhar, and Amir Barati Farimani. Large Language Model Agent for Modular Task Execution in Drug Discovery, June 2025. URL <http://arxiv.org/abs/2507.02925>. arXiv:2507.02925 [cs].
- [165] Francis Ogoke and Amir Barati Farimani. Thermal Control of Laser Powder Bed Fusion Using Deep Reinforcement Learning, January 2021. URL <http://arxiv.org/abs/2102.03355>. arXiv:2102.03355 [physics].
- [166] Francis Ogoke, Quanliang Liu, Olabode Ajenifujah, Alexander Myers, Guadalupe Quirarte, Jack Beuth, Jonathan Malen, and Amir Barati Farimani. Inexpensive High Fidelity Melt Pool Models in Additive Manufacturing Using Generative Deep Diffusion, November 2023. URL <http://arxiv.org/abs/2311.16168>. arXiv:2311.16168 [cond-mat].

- [167] Francis Ogoke, Peter Pak, Alexander Myers, Guadalupe Quirarte, Jack Beuth, Jonathan Malen, and Amir Barati Farimani. Deep learning for melt pool depth contour prediction from surface thermal images via vision transformers. *Additive Manufacturing Letters*, 11: 100243, December 2024. ISSN 2772-3690. doi: 10.1016/j.addlet.2024.100243. URL <https://www.sciencedirect.com/science/article/pii/S2772369024000513>.
- [168] W. O'Neill, C. J. Sutcliffe, R. Morgan, A. Landsborough, and K. K. B. Hon. Investigation on Multi-Layer Direct Metal Laser Sintering of 316L Stainless Steel Powder Beds. *CIRP Annals*, 48(1):151–154, January 1999. ISSN 0007-8506. doi: 10.1016/S0007-8506(07)63153-9. URL <https://www.sciencedirect.com/science/article/pii/S0007850607631539>.
- [169] OpenAI, Sandhini Agarwal, Lama Ahmad, Jason Ai, Sam Altman, Andy Applebaum, Edwin Arbus, Rahul K. Arora, Yu Bai, Bowen Baker, Haiming Bao, Boaz Barak, Ally Bennett, Tyler Bertao, Nivedita Brett, Eugene Brevdo, Greg Brockman, Sebastien Bubeck, Che Chang, Kai Chen, Mark Chen, Enoch Cheung, Aidan Clark, Dan Cook, Marat Dukhan, Casey Dvorak, Kevin Fives, Vlad Fomenko, Timur Garipov, Kristian Georgiev, Mia Glaese, Tarun Gogineni, Adam Goucher, Lukas Gross, Katia Gil Guzman, John Hallman, Jackie Hehir, Johannes Heidecke, Alec Helyar, Haitang Hu, Romain Huet, Jacob Huh, Saachi Jain, Zach Johnson, Chris Koch, Irina Kofman, Dominik Kundel, Jason Kwon, Volodymyr Kyrylov, Elaine Ya Le, Guillaume Leclerc, James Park Lennon, Scott Lessans, Mario Lezcano-Casado, Yuanzhi Li, Zhuohan Li, Ji Lin, Jordan Liss, Lily, Liu, Jiancheng Liu, Kevin Lu, Chris Lu, Zoran Martinovic, Lindsay McCallum, Josh McGrath, Scott McKinney, Aidan McLaughlin, Song Mei, Steve Mostovoy, Tong Mu, Gideon Myles, Alexander Neitz, Alex Nichol, Jakub Pachocki, Alex Paino, Dana Palmie, Ashley Pantuliano, Giambattista Parascandolo, Jongsoo Park, Leher Pathak, Carolina Paz, Ludovic Peran, Dmitry Pimenov, Michelle Pokrass, Elizabeth Proehl, Huida Qiu, Gaby Raila,

Filippo Raso, Hongyu Ren, Kimmy Richardson, David Robinson, Bob Rotsted, Hadi Salman, Suvansh Sanjeev, Max Schwarzer, D. Sculley, Harshit Sikchi, Kendal Simon, Karan Singhal, Yang Song, Dane Stuckey, Zhiqing Sun, Philippe Tillet, Sam Toizer, Foivos Tsimpourlas, Nikhil Vyas, Eric Wallace, Xin Wang, Miles Wang, Olivia Watkins, Kevin Weil, Amy Wendling, Kevin Whinnery, Cedric Whitney, Hannah Wong, Lin Yang, Yu Yang, Michihiro Yasunaga, Kristen Ying, Wojciech Zaremba, Wenting Zhan, Cyril Zhang, Brian Zhang, Eddie Zhang, and Shengjia Zhao. gpt-oss-120b & gpt-oss-20b Model Card, August 2025. URL <http://arxiv.org/abs/2508.10925>. arXiv:2508.10925 [cs].

- [170] Nerea Ordás, Luis Carlos Ardila, Iñigo Iturriza, Fermín Garcianda, Pedro Álvarez, and Carmen García-Rosales. Fabrication of TBMs cooling structures demonstrators using additive manufacturing (AM) technology and HIP. *Fusion Engineering and Design*, 96-97:142–148, October 2015. ISSN 0920-3796. doi: 10.1016/j.fusengdes.2015.05.059. URL <https://www.sciencedirect.com/science/article/pii/S0920379615300107>.
- [171] Peter Pak and Amir Barati Farimani. AdditiveLLM: Large language models predict defects in metals additive manufacturing. *Additive Manufacturing Letters*, 14:100292, July 2025. ISSN 2772-3690. doi: 10.1016/j.addlet.2025.100292. URL <https://www.sciencedirect.com/science/article/pii/S277236902500026X>.
- [172] Peter Pak, Francis Ogoke, Andrew Polonsky, Anthony Garland, Dan S. Bolintineanu, Dan R. Moser, Mary Arnhart, Jonathan Madison, Thomas Ivanoff, John Mitchell, Bradley Jared, Brad Salzbrenner, Michael J. Heiden, and Amir Barati Farimani. ThermoPore: Predicting part porosity based on thermal images using deep learning. *Additive Manufacturing*, 95:104503, September 2024. ISSN 2214-8604. doi: 10.1016/j.addma.2024.104503. URL <https://www.sciencedirect.com/science/article/pii/S2214860424005499>.

- [173] Peter Pak, Achuth Chandrasekhar, and Amir Barati Farimani. Agentic additive manufacturing alloy evaluation. *Additive Manufacturing Letters*, 17:100355, April 2026. ISSN 2772-3690. doi: 10.1016/j.addlet.2026.100355. URL <https://www.sciencedirect.com/science/article/pii/S2772369026000022>.
- [174] Yash Parikh and Mathew Kuttolamadom. Property-Graded Stainless Steel 316L by Selective Laser Melting: Characterization & Design. *Journal of Manufacturing Science and Engineering*, 145(061008), February 2023. ISSN 1087-1357. doi: 10.1115/1.4056825. URL <https://doi.org/10.1115/1.4056825>.
- [175] Ratnadeep Paul, Sam Anand, and Frank Gerner. Effect of Thermal Deformation on Part Errors in Metal Powder Based Additive Manufacturing Processes. *Journal of Manufacturing Science and Engineering*, 136(031009), March 2014. ISSN 1087-1357. doi: 10.1115/1.4026524. URL <https://doi.org/10.1115/1.4026524>.
- [176] Pralhad Pesode and Shivprakash Barve. Additive manufacturing of metallic biomaterials and its biocompatibility. *Materials Today: Proceedings*, November 2022. ISSN 2214-7853. doi: 10.1016/j.matpr.2022.11.248. URL <https://www.sciencedirect.com/science/article/pii/S2214785322070985>.
- [177] Pralhad Pesode and Shivprakash Barve. Additive manufacturing of magnesium alloys and its biocompatibility. *Bioprinting*, 36: e00318, December 2023. ISSN 2405-8866. doi: 10.1016/j.bprint.2023. e00318. URL <https://www.sciencedirect.com/science/article/pii/S2405886623000611>.
- [178] A. Phua, C. H. J. Davies, and G. W. Delaney. A digital twin hierarchy for metal additive manufacturing. *Computers in Industry*, 140: 103667, September 2022. ISSN 0166-3615. doi: 10.1016/j.compind.2022.103667. URL <https://www.sciencedirect.com/science/article/pii/S0166361522000641>.

- [179] Andrew T. Polonsky and Tresa M. Pollock. Closing the science gap in 3D metal printing. *Science*, 368(6491):583–584, May 2020. doi: 10.1126/science.abb4938. URL <https://www.science.org/doi/10.1126/science.abb4938>.
- [180] A. Popovich, V. Sufiarov, I. Polozov, E. Borisov, D. Masaylo, and A. Orlov. Microstructure and mechanical properties of additive manufactured copper alloy. *Materials Letters*, 179:38–41, September 2016. ISSN 0167-577X. doi: 10.1016/j.matlet.2016.05.064. URL <https://www.sciencedirect.com/science/article/pii/S0167577X16307819>.
- [181] Alec Radford, Karthik Narasimhan, Tim Salimans, and Ilya Sutskever. Improving Language Understanding by Generative Pre-Training.
- [182] Colin Raffel, Noam Shazeer, Adam Roberts, Katherine Lee, Sharan Narang, Michael Matena, Yanqi Zhou, Wei Li, and Peter J. Liu. Exploring the Limits of Transfer Learning with a Unified Text-to-Text Transformer, September 2023. URL <http://arxiv.org/abs/1910.10683>. arXiv:1910.10683 [cs].
- [183] M. Azizur Rahman, Tanveer Saleh, Muhammad Pervez Jahan, Conor McGarry, Akshay Chaudhari, Rui Huang, M. Tauhiduzzaman, Afzaal Ahmed, Abdullah Al Mahmud, Md Shahnewaz Bhuiyan, Md Faysal Khan, Md Shafiq Alam, and Md Shihab Shakur. Review of Intelligence for Additive and Subtractive Manufacturing: Current Status and Future Prospects. *Micromachines*, 14(3):508, March 2023. ISSN 2072-666X. doi: 10.3390/mi14030508. URL <https://www.mdpi.com/2072-666X/14/3/508>. Number: 3.
- [184] René Ranftl, Alexey Bochkovskiy, and Vladlen Koltun. Vision Transformers for Dense Prediction, March 2021. URL <http://arxiv.org/abs/2103.13413>. arXiv:2103.13413 [cs].
- [185] Asim Rashid and Aditya Gopaluni. A Review of Residual Stress and Deformation Modeling for Metal Additive Manufacturing Pro-

- cesses. *Chinese Journal of Mechanical Engineering: Additive Manufacturing Frontiers*, 2(4):100102, December 2023. ISSN 2772-6657. doi: 10.1016/j.cjmeam.2023.100102. URL <https://www.sciencedirect.com/science/article/pii/S2772665723000417>.
- [186] Zhongshu Ren, Lin Gao, Samuel J. Clark, Kamel Fezzaa, Pavel Shevchenko, Ann Choi, Wes Everhart, Anthony D. Rollett, Lianyi Chen, and Tao Sun. Machine learning-aided real-time detection of key-hole pore generation in laser powder bed fusion. *Science*, 379(6627): 89–94, January 2023. doi: 10.1126/science.add4667. URL <https://www.science.org/doi/full/10.1126/science.add4667>.
- [187] Edward Reutzel, Jan Petrich, David Jeffrey Corbin, and Zackary Snow. Application of Machine Learning to Monitor Metal Powder-Bed Fusion Additive Manufacturing Processes. June 2023. doi: 10.31399/asm.hb.v24A.a0006992. URL <https://dl.asminternational.org/handbooks/edited-volume/187/chapter/3798624/Application-of-Machine-Learning-to-Monitor-Metal>.
- [188] Emmanuel Rodriguez, Jorge Mireles, Cesar A. Terrazas, David Espalin, Mireya A. Perez, and Ryan B. Wicker. Approximation of absolute surface temperature measurements of powder bed fusion additive manufacturing technology using *in situ* infrared thermography. *Additive Manufacturing*, 5:31–39, January 2015. ISSN 2214-8604. doi: 10.1016/j.addma.2014.12.001. URL <https://www.sciencedirect.com/science/article/pii/S2214860414000256>.
- [189] O. L. Rodriguez, P. G. Allison, W. R. Whittington, D. K. Francis, O. G. Rivera, K. Chou, X. Gong, T. M. Butler, and J. F. Burroughs. Dynamic tensile behavior of electron beam additive manufactured Ti6Al4V. *Materials Science and Engineering: A*, 641:323–327, August 2015. ISSN 0921-5093. doi: 10.1016/j.msea.2015.06.069. URL <https://www.sciencedirect.com/science/article/pii/S0921509315301258>.
- [190] Byeong-Min Roh, Soundar R. T. Kumara, Paul Witherell, and Timothy W. Simpson. Ontology-based Process Map for Metal Ad-

ditive Manufacturing. *Journal of Materials Engineering and Performance*, 30(12):8784–8797, December 2021. ISSN 1544-1024. doi: 10.1007/s11665-021-06274-2. URL <https://doi.org/10.1007/s11665-021-06274-2>.

- [191] D. Rosenthal. The Theory of Moving Sources of Heat and Its Application to Metal Treatments. *Transactions of the American Society of Mechanical Engineers*, 68(8):849–865, December 2022. ISSN 0097-6822. doi: 10.1115/1.4018624. URL <https://doi.org/10.1115/1.4018624>.
- [192] Daniel Rosenthal. Mathematical Theory of Heat Distribution during Welding and Cutting. 20(5):220s–234s, 1941.
- [193] W. J. Sames, F. A. List, S. Pannala, R. R. Dehoff, and S. S. Babu. The metallurgy and processing science of metal additive manufacturing. *International Materials Reviews*, 61(5):315–360, July 2016. ISSN 0950-6608. doi: 10.1080/09506608.2015.1116649. URL <https://journals.sagepub.com/action/showAbstract>.
- [194] Victor Sanh, Lysandre Debut, Julien Chaumond, and Thomas Wolf. DistilBERT, a distilled version of BERT: smaller, faster, cheaper and lighter, March 2020. URL <http://arxiv.org/abs/1910.01108>. arXiv:1910.01108 [cs].
- [195] Nigel Saunders and Peter Miodownik. The Application of CALPHAD Methods - ScienceDirect. URL <https://www.sciencedirect.com/science/article/abs/pii/S1470180498800308>.
- [196] Manfred Schmid, Antonio Amado, and Konrad Wegener. Polymer powders for selective laser sintering (SLS). *AIP Conference Proceedings*, 1664(1):160009, May 2015. ISSN 0094-243X. doi: 10.1063/1.4918516. URL <https://doi.org/10.1063/1.4918516>.
- [197] K. Schmidtke, F. Palm, A. Hawkins, and C. Emmelmann. Process and Mechanical Properties: Applicability of a Scandium modified Al-alloy for Laser Additive Manufacturing. *Physics Procedia*, 12:369–374, January 2011. ISSN 1875-3892. doi: 10.1016/j.phpro.2011.03.

047. URL <https://www.sciencedirect.com/science/article/pii/S187538921100126X>.
- [198] Thomas Scialom, Tuhin Chakrabarty, and Smaranda Muresan. Fine-tuned Language Models are Continual Learners, October 2022. URL <http://arxiv.org/abs/2205.12393>. arXiv:2205.12393 [cs].
- [199] Eyob Messele Sefene. State-of-the-art of selective laser melting process: A comprehensive review. *Journal of Manufacturing Systems*, 63: 250–274, April 2022. ISSN 0278-6125. doi: 10.1016/j.jmsy.2022.04.002. URL <https://www.sciencedirect.com/science/article/pii/S0278612522000516>.
- [200] Mohsen Seifi, Ayman Salem, Jack Beuth, Ola Harrysson, and John J. Lewandowski. Overview of Materials Qualification Needs for Metal Additive Manufacturing. *JOM*, 68(3):747–764, March 2016. ISSN 1543-1851. doi: 10.1007/s11837-015-1810-0. URL <https://doi.org/10.1007/s11837-015-1810-0>.
- [201] Rico Sennrich, Barry Haddow, and Alexandra Birch. Neural Machine Translation of Rare Words with Subword Units. In Katrin Erk and Noah A. Smith, editors, *Proceedings of the 54th Annual Meeting of the Association for Computational Linguistics (Volume 1: Long Papers)*, pages 1715–1725, Berlin, Germany, August 2016. Association for Computational Linguistics. doi: 10.18653/v1/P16-1162. URL <https://aclanthology.org/P16-1162/>.
- [202] Aayush Shah, Chakradhar Guntuboina, and Amir Barati Farimani. Peptide-GPT: Generative Design of Peptides using Generative Pre-trained Transformers and Bio-informatic Supervision, October 2024. URL <http://arxiv.org/abs/2410.19222>. arXiv:2410.19222.
- [203] Hanul Shin, Jung Kwon Lee, Jaehong Kim, and Jiwon Kim. Continual Learning with Deep Generative Replay. In *Advances in Neural Information Processing Systems*, volume 30. Curran Associates,

Inc., 2017. URL https://papers.nips.cc/paper_files/paper/2017/hash/0efbe98067c6c73dba1250d2beaa81f9-Abstract.html.

- [204] Subin Shrestha and Kevin Chou. Formation of keyhole and lack of fusion pores during the laser powder bed fusion process. *Manufacturing Letters*, 32:19–23, April 2022. ISSN 2213-8463. doi: 10.1016/j.mfglet.2022.01.005. URL <https://www.sciencedirect.com/science/article/pii/S2213846322000050>.
- [205] Subin Shrestha, Thomas Starr, and Kevin Chou. A Study of Keyhole Porosity in Selective Laser Melting: Single-Track Scanning With Micro-CT Analysis. *Journal of Manufacturing Science and Engineering*, 141(071004), May 2019. ISSN 1087-1357. doi: 10.1115/1.4043622. URL <https://doi.org/10.1115/1.4043622>.
- [206] Manpreet Singh, Fujun Ruan, Albert Xu, Yuchen Wu, Archit Rungta, Luyuan Wang, Kevin Song, Howie Choset, and Lu Li. Toward Closed-Loop Additive Manufacturing: Paradigm Shift in Fabrication, Inspection, and Repair. In *2023 IEEE/RSJ International Conference on Intelligent Robots and Systems (IROS)*, pages 10066–10073, October 2023. doi: 10.1109/IROS55552.2023.10342148. URL <https://ieeexplore.ieee.org/document/10342148>. ISSN: 2153-0866.
- [207] John A Slotwinski, Edward J Garboczi, and Keith M Hebenstreit. Porosity Measurements and Analysis for Metal Additive Manufacturing Process Control. *Journal of Research of the National Institute of Standards and Technology*, 119:494–528, September 2014. ISSN 1044-677X. doi: 10.6028/jres.119.019. URL <https://www.ncbi.nlm.nih.gov/pmc/articles/PMC4487290/>.
- [208] Thale R. Smith, Joshua D. Sugar, Julie M. Schoenung, and Chris San Marchi. Relationship between manufacturing defects and fatigue properties of additive manufactured austenitic stainless steel. *Materials Science and Engineering: A*, 765:138268, September 2019. ISSN 0921-5093. doi: 10.1016/j.msea.2019.138268. URL <https://www.sciencedirect.com/science/article/pii/S0921509319310548>.

- [209] Jacob C. Snyder, Curtis K. Stimpson, Karen A. Thole, and Dominic J. Mongillo. Build Direction Effects on Microchannel Tolerance and Surface Roughness. *Journal of Mechanical Design*, 137(111411), October 2015. ISSN 1050-0472. doi: 10.1115/1.4031071. URL <https://doi.org/10.1115/1.4031071>.
- [210] Antonella Sola and Alireza Nouri. Microstructural porosity in additive manufacturing: The formation and detection of pores in metal parts fabricated by powder bed fusion. *Journal of Advanced Manufacturing and Processing*, 1(3):e10021, 2019. ISSN 2637-403X. doi: 10.1002/amp.2.10021. URL <https://onlinelibrary.wiley.com/doi/abs/10.1002/amp.2.10021>. _eprint: <https://onlinelibrary.wiley.com/doi/pdf/10.1002/amp.2.10021>.
- [211] Tomas Starek and Pavel Dyntera. SLS4All, 2020. URL <https://sls4all.com/>.
- [212] Seth T. Strayer, William J. Frieden Templeton, Florian X. Dugast, Sneha P. Narra, and Albert C. To. Accelerating High-Fidelity Thermal Process Simulation of Laser Powder Bed Fusion via the Computational Fluid Dynamics Imposed Finite Element Method (CIFEM). *Additive Manufacturing Letters*, 3:100081, December 2022. ISSN 2772-3690. doi: 10.1016/j.addlet.2022.100081. URL <https://www.sciencedirect.com/science/article/pii/S2772369022000500>.
- [213] Jianlin Su, Yu Lu, Shengfeng Pan, Ahmed Murtadha, Bo Wen, and Yunfeng Liu. RoFormer: Enhanced Transformer with Rotary Position Embedding, November 2023. URL <http://arxiv.org/abs/2104.09864>. arXiv:2104.09864 [cs].
- [214] Guifang Sun, Rui Zhou, Jinzhong Lu, and Jyotirmoy Mazumder. Evaluation of defect density, microstructure, residual stress, elastic modulus, hardness and strength of laser-deposited AISI 4340 steel. *Acta Materialia*, 84:172–189, February 2015. ISSN 1359-6454. doi: 10.1016/j.actamat.2014.09.028. URL <https://www.sciencedirect.com/science/article/pii/S1359645414007071>.

- [215] S. Tammas-Williams and I. Todd. Design for additive manufacturing with site-specific properties in metals and alloys. *Scripta Materialia*, 135: 105–110, July 2017. ISSN 1359-6462. doi: 10.1016/j.scriptamat.2016.10.030. URL <https://www.sciencedirect.com/science/article/pii/S1359646216305255>.
- [216] Xipeng Tan, Yihong Kok, Yu Jun Tan, Marion Descoins, Dominique Mangelinck, Shu Beng Tor, Kah Fai Leong, and Chee Kai Chua. Graded microstructure and mechanical properties of additive manufactured Ti-6Al-4V via electron beam melting. *Acta Materialia*, 97:1–16, September 2015. ISSN 1359-6454. doi: 10.1016/j.actamat.2015.06.036. URL <https://www.sciencedirect.com/science/article/pii/S135964541500422X>.
- [217] Ming Tang, P. Chris Pistorius, Sneha Narra, and Jack L. Beuth. Rapid Solidification: Selective Laser Melting of AlSi10Mg. *JOM*, 68(3):960–966, March 2016. ISSN 1543-1851. doi: 10.1007/s11837-015-1763-3. URL <https://doi.org/10.1007/s11837-015-1763-3>.
- [218] Ming Tang, P. Chris Pistorius, and Jack L. Beuth. Prediction of lack-of-fusion porosity for powder bed fusion. *Additive Manufacturing*, 14: 39–48, March 2017. ISSN 2214-8604. doi: 10.1016/j.addma.2016.12.001. URL <https://www.sciencedirect.com/science/article/pii/S2214860416300471>.
- [219] Gustavo Tapia, Saad Khairallah, Manyalibo Matthews, Wayne E. King, and Alaa Elwany. Gaussian process-based surrogate modeling framework for process planning in laser powder-bed fusion additive manufacturing of 316L stainless steel. *The International Journal of Advanced Manufacturing Technology*, 94(9):3591–3603, February 2018. ISSN 1433-3015. doi: 10.1007/s00170-017-1045-z. URL <https://doi.org/10.1007/s00170-017-1045-z>.
- [220] Joshua R. Tempelman, Adam J. Wachtor, Eric B. Flynn, Phillip J. Depond, Jean-Baptiste Forien, Gabe M. Guss, Nicholas P. Calta, and

Manyalibo J. Matthews. Detection of keyhole pore formations in laser powder-bed fusion using acoustic process monitoring measurements. *Additive Manufacturing*, 55:102735, July 2022. ISSN 2214-8604. doi: 10.1016/j.addma.2022.102735. URL <https://www.sciencedirect.com/science/article/pii/S2214860422001397>.

- [221] Avijit Thawani, Jay Pujara, Pedro A. Szekely, and Filip Ilievski. Representing Numbers in NLP: a Survey and a Vision, March 2021. URL <http://arxiv.org/abs/2103.13136>. arXiv:2103.13136 [cs].
- [222] Thermo-Calc Software. Thermo-Calc Software, 2025. URL <https://thermocalc.com/>.
- [223] Xiaoyong Tian, Lingling Wu, Dongdong Gu, Shangqin Yuan, Yufan Zhao, Xiao Li, Liliang Ouyang, Bo Song, Tong Gao, Jiankang He, Xin Lin, Feng Lin, Jihong Zhu, and Dichen Li. Roadmap for Additive Manufacturing: Toward Intellectualization and Industrialization. *Chinese Journal of Mechanical Engineering: Additive Manufacturing Frontiers*, 1(1):92, March 2022. ISSN 2772-6657. doi: 10.1016/j.cjmeam.2022.100014. URL <https://www.sciencedirect.com/science/article/pii/S2772665722000046>.
- [224] Hugo Touvron, Thibaut Lavril, Gautier Izacard, Xavier Martinet, Marie-Anne Lachaux, Timothée Lacroix, Baptiste Rozière, Naman Goyal, Eric Hambro, Faisal Azhar, Aurelien Rodriguez, Armand Joulin, Edouard Grave, and Guillaume Lample. LLaMA: Open and Efficient Foundation Language Models, February 2023. URL <http://arxiv.org/abs/2302.13971>. arXiv:2302.13971.
- [225] Hugo Touvron, Louis Martin, Kevin Stone, Peter Albert, Amjad Almalhairi, Yasmine Babaei, Nikolay Bashlykov, Soumya Batra, Prajjwal Bhargava, Shruti Bhosale, Dan Bikel, Lukas Blecher, Cristian Canton Ferrer, Moya Chen, Guillem Cucurull, David Esiobu, Jude Fernandes, Jeremy Fu, Wenyin Fu, Brian Fuller, Cynthia Gao, Vedanuj Goswami, Naman Goyal, Anthony Hartshorn, Saghar Hosseini, Rui

Hou, Hakan Inan, Marcin Kardas, Viktor Kerkez, Madian Khabsa, Isabel Kloumann, Artem Korenev, Punit Singh Koura, Marie-Anne Lachaux, Thibaut Lavril, Jenya Lee, Diana Liskovich, Yinghai Lu, Yuning Mao, Xavier Martinet, Todor Mihaylov, Pushkar Mishra, Igor Molybog, Yixin Nie, Andrew Poulton, Jeremy Reizenstein, Rashi Rungta, Kalyan Saladi, Alan Schelten, Ruan Silva, Eric Michael Smith, Ranjan Subramanian, Xiaoqing Ellen Tan, Binh Tang, Ross Taylor, Adina Williams, Jian Xiang Kuan, Puxin Xu, Zheng Yan, Iliyan Zarov, Yuchen Zhang, Angela Fan, Melanie Kambadur, Sharan Narang, Aurelien Rodriguez, Robert Stojnic, Sergey Edunov, and Thomas Scialom. Llama 2: Open Foundation and Fine-Tuned Chat Models, July 2023. URL <http://arxiv.org/abs/2307.09288>. arXiv:2307.09288.

- [226] Du Tran, Lubomir Bourdev, Rob Fergus, Lorenzo Torresani, and Manohar Paluri. Learning Spatiotemporal Features with 3D Convolutional Networks, October 2015. URL <http://arxiv.org/abs/1412.0767>. arXiv:1412.0767 [cs].
- [227] Johannes Trapp, Alexander M. Rubenchik, Gabe Guss, and Manyalibo J. Matthews. In situ absorptivity measurements of metallic powders during laser powder-bed fusion additive manufacturing. *Applied Materials Today*, 9:341–349, December 2017. ISSN 2352-9407. doi: 10.1016/j.apmt.2017.08.006. URL <https://www.sciencedirect.com/science/article/pii/S2352940717302123>.
- [228] Wakshum M. Tucho, Vidar H. Lysne, Håkon Austbø, Atle Sjolyst-Kverneland, and Vidar Hansen. Investigation of effects of process parameters on microstructure and hardness of SLM manufactured SS316L. *Journal of Alloys and Compounds*, 740:910–925, April 2018. ISSN 0925-8388. doi: 10.1016/j.jallcom.2018.01.098. URL <https://www.sciencedirect.com/science/article/pii/S0925838818300999>.
- [229] N. K. Vail, J. W. Barlow, and H. L. Marcus. Silicon Carbide Preforms for Metal Infiltration by Selective Laser Sintering™ of Polymer Encapsulated Powders. 1993. URL <http://hdl.handle.net/2152/65059>.

- [230] Ashish Vaswani, Noam Shazeer, Niki Parmar, Jakob Uszkoreit, Llion Jones, Aidan N. Gomez, Łukasz Kaiser, and Illia Polosukhin. Attention Is All You Need, August 2023. URL <http://arxiv.org/abs/1706.03762>. arXiv:1706.03762 [cs].
- [231] Bey Vrancken, Lore Thijs, Jean-Pierre Kruth, and Jan Van Humbeeck. Heat treatment of Ti6Al4V produced by Selective Laser Melting: Microstructure and mechanical properties. *Journal of Alloys and Compounds*, 541:177–185, November 2012. ISSN 0925-8388. doi: 10.1016/j.jallcom.2012.07.022. URL <https://www.sciencedirect.com/science/article/pii/S0925838812011826>.
- [232] Liyuan Wang, Xingxing Zhang, Hang Su, and Jun Zhu. A Comprehensive Survey of Continual Learning: Theory, Method and Application. *IEEE Trans. Pattern Anal. Mach. Intell.*, 46(8):5362–5383, August 2024. ISSN 0162-8828. doi: 10.1109/TPAMI.2024.3367329. URL <https://doi.org/10.1109/TPAMI.2024.3367329>.
- [233] Lu Wang, Yanming Zhang, Hou Yi Chia, and Wentao Yan. Mechanism of keyhole pore formation in metal additive manufacturing. *npj Computational Materials*, 8(1):1–11, January 2022. ISSN 2057-3960. doi: 10.1038/s41524-022-00699-6. URL <https://www.nature.com/articles/s41524-022-00699-6>.
- [234] Jason Wei, Xuezhi Wang, Dale Schuurmans, Maarten Bosma, Brian Ichter, Fei Xia, Ed Chi, Quoc Le, and Denny Zhou. Chain-of-Thought Prompting Elicits Reasoning in Large Language Models, January 2023. URL <http://arxiv.org/abs/2201.11903>. arXiv:2201.11903 [cs].
- [235] John D. Williams and Carl R. Deckard. Advances in modeling the effects of selected parameters on the SLS process. *Rapid Prototyping Journal*, 4(2):90–100, June 1998. ISSN 1355-2546. doi: 10.1108/13552549810210257. URL <https://doi.org/10.1108/13552549810210257>.

- [236] Tongtong Wu, Linhao Luo, Yuan-Fang Li, Shirui Pan, Thuy-Trang Vu, and Gholamreza Haffari. Continual Learning for Large Language Models: A Survey, February 2024. URL <http://arxiv.org/abs/2402.01364>. arXiv:2402.01364 [cs].
- [237] Mujian Xia, Dongdong Gu, Guanqun Yu, Donghua Dai, Hongyu Chen, and Qimin Shi. Influence of hatch spacing on heat and mass transfer, thermodynamics and laser processability during additive manufacturing of Inconel 718 alloy. *International Journal of Machine Tools and Manufacture*, 109:147–157, October 2016. ISSN 0890-6955. doi: 10.1016/j.ijmachtools.2016.07.010. URL <https://www.sciencedirect.com/science/article/pii/S0890695516300906>.
- [238] Zhenlin Xu, Hui Zhang, Xiaojie Du, Yizhu He, Hong Luo, Guangsheng Song, Li Mao, Tingwei Zhou, and Lianglong Wang. Corrosion resistance enhancement of CoCrFeMnNi high-entropy alloy fabricated by additive manufacturing. *Corrosion Science*, 177:108954, December 2020. ISSN 0010-938X. doi: 10.1016/j.corsci.2020.108954. URL <https://www.sciencedirect.com/science/article/pii/S0010938X20310702>.
- [239] Aref Yadollahi, Nima Shamsaei, Scott M. Thompson, and Denver W. Seely. Effects of process time interval and heat treatment on the mechanical and microstructural properties of direct laser deposited 316L stainless steel. *Materials Science and Engineering: A*, 644:171–183, September 2015. ISSN 0921-5093. doi: 10.1016/j.msea.2015.07.056. URL <https://www.sciencedirect.com/science/article/pii/S0921509315302082>.
- [240] Shunyu Yao, Jeffrey Zhao, Dian Yu, Nan Du, Izhak Shafran, Karthik R. Narasimhan, and Yuan Cao. ReAct: Synergizing Reasoning and Acting in Language Models. September 2022. URL https://openreview.net/forum?id=WE_vluYUL-X.
- [241] H. Yeung and B. Lane. A residual heat compensation based scan strategy for powder bed fusion additive manufacturing. *Manufacturing Letters*,

- 25:56–59, August 2020. ISSN 2213-8463. doi: 10.1016/j.mfglet.2020.07.005. URL <https://www.sciencedirect.com/science/article/pii/S221384632030136X>.
- [242] Siyu Yu, Yifan Wu, Ying Li, and Pinjia He. Unlocking the Power of Numbers: Log Compression via Numeric Token Parsing, August 2024. URL <http://arxiv.org/abs/2408.05760>. arXiv:2408.05760 [cs].
- [243] Setareh Zakeri, Minnamari Vippola, and Erkki Levänen. A comprehensive review of the photopolymerization of ceramic resins used in stereolithography. *Additive Manufacturing*, 35:101177, October 2020. ISSN 2214-8604. doi: 10.1016/j.addma.2020.101177. URL <https://www.sciencedirect.com/science/article/pii/S2214860420305492>.
- [244] Zhixin Zhan and Hua Li. Machine learning based fatigue life prediction with effects of additive manufacturing process parameters for printed SS 316L. *International Journal of Fatigue*, 142:105941, January 2021. ISSN 0142-1123. doi: 10.1016/j.ijfatigue.2020.105941. URL <https://www.sciencedirect.com/science/article/pii/S0142112320304722>.
- [245] Baicheng Zhang, Hanlin Liao, and Christian Coddet. Microstructure evolution and density behavior of CP Ti parts elaborated by Self-developed vacuum selective laser melting system. *Applied Surface Science*, 279:310–316, August 2013. ISSN 0169-4332. doi: 10.1016/j.apsusc.2013.04.090. URL <https://www.sciencedirect.com/science/article/pii/S0169433213007940>.
- [246] Bing Zhang, Raiyan Seede, Lei Xue, Kadri C. Atli, Chen Zhang, Austin Whitt, Ibrahim Karaman, Raymundo Arroyave, and Alaa Elwany. An efficient framework for printability assessment in Laser Powder Bed Fusion metal additive manufacturing. *Additive Manufacturing*, 46:102018, October 2021. ISSN 2214-8604. doi: 10.1016/j.addma.2021.102018. URL <https://www.sciencedirect.com/science/article/pii/S2214860421001834>.

- [247] Li Zhang, Xiaoqi Chen, Wei Zhou, Taobo Cheng, Lijia Chen, Zhen Guo, Bing Han, and Longxing Lu. Digital Twins for Additive Manufacturing: A State-of-the-Art Review. *Applied Sciences*, 10(23):8350, January 2020. ISSN 2076-3417. doi: 10.3390/app10238350. URL <https://www.mdpi.com/2076-3417/10/23/8350>. Number: 23.
- [248] Shuyao Zhang, Yajing Li, Hailong Dai, Zhe Zhang, and Xu Chen. Achieving balanced uniform and local corrosion performance of SS 316L/IN625 hybrid alloy manufactured by directed energy deposition. *Journal of Materials Research and Technology*, 32:3937–3948, September 2024. ISSN 2238-7854. doi: 10.1016/j.jmrt.2024.08.210. URL <https://www.sciencedirect.com/science/article/pii/S2238785424020003>.
- [249] Siqi Zhang, Hui Yang, Zhuo Yang, and Yan Lu. Engineering-Guided Deep Learning of Melt-Pool Dynamics for Additive Manufacturing Quality Monitoring. *Journal of Computing and Information Science in Engineering*, 24(101002), August 2024. ISSN 1530-9827. doi: 10.1115/1.4066026. URL <https://doi.org/10.1115/1.4066026>.
- [250] Yi Zhang and Jing Zhang. Modeling of solidification microstructure evolution in laser powder bed fusion fabricated 316L stainless steel using combined computational fluid dynamics and cellular automata. *Additive Manufacturing*, 28:750–765, August 2019. ISSN 2214-8604. doi: 10.1016/j.addma.2019.06.024. URL <https://www.sciencedirect.com/science/article/pii/S2214860418304871>.
- [251] Qi Zhong, Xiaoyong Tian, Xiaokang Huang, Cunbao Huo, and Dichen Li. Using feedback control of thermal history to improve quality consistency of parts fabricated via large-scale powder bed fusion. *Additive Manufacturing*, 42:101986, June 2021. ISSN 2214-8604. doi: 10.1016/j.addma.2021.101986. URL <https://www.sciencedirect.com/science/article/pii/S2214860421001512>.
- [252] Bin Zhou, Jun Zhou, Hongxin Li, and Feng Lin. A study of the microstructures and mechanical properties of Ti6Al4V fabricated by

SLM under vacuum. *Materials Science and Engineering: A*, 724: 1–10, May 2018. ISSN 0921-5093. doi: 10.1016/j.msea.2018.03.021. URL <https://www.sciencedirect.com/science/article/pii/S0921509318303551>.